NAVAL POSTGRADUATE SCHOOL
Monterey, California

AD-A283 535

94-26797

DISSERTATION

TIDAL DYNAMICS
AND MIXING
OVER STEEP TOPOGRAPHY

by

Emanuel Ferreira Coelho

June 1994

Dissertation Supervisor   Timothy P. Stanton

94 8 23 031

REPORT DOCUMENTATION PAGE

1a. REPORT SECURITY CLASSIFICATION UNCLASSIFIED	1b. RESTRICTIVE MARKINGS
2a. SECURITY CLASSIFICATION AUTHORITY	3. DISTRIBUTION/AVAILABILITY OF REPORT
2b. DECLASSIFICATION/DOWNGRADING SCHEDULE	Approved for public release; distribution is unlimited

4. PERFORMING ORGANIZATION REPORT NUMBER(S)	5. MONITORING ORGANIZATION REPORT NUMBER(S)

6a. NAME OF PERFORMING ORGANIZATION Dept. Physical Oceanography Naval Postgraduate School	6b. OFFICE SYMBOL (if applicable) 35	7a. NAME OF MONITORING ORGANIZATION Naval Postgraduate School
6c. ADDRESS (City, State, and ZIP Code) Monterey, CA 93943-5000		7b. ADDRESS (City, State, and ZIP Code) Monterey, CA 93943-5000

8a. NAME OF FUNDING/SPONSORING ORGANIZATION	8b. OFFICE SYMBOL (if applicable)	9. PROCUREMENT INSTRUMENT IDENTIFICATION NUMBER
8c. ADDRESS (City, State, and ZIP Code)		10. SOURCE OF FUNDING NUMBERS

PROGRAM ELEMENT NO.	PROJECT NO.	TASK NO.	WORK UNIT ACCESSION NO.

11. TITLE (Include Security Classification)
TIDAL DYNAMICS AND MIXING OVER STEEP TOPOGRAPHY

12. PERSONAL AUTHOR(S)
Emanuel Ferreira Coelho

13a. TYPE OF REPORT Doctoral Dissertation	13b. TIME COVERED FROM TO	14. DATE OF REPORT (Year, Month, Day) June 1994	15. PAGE COUNT 222

16. SUPPLEMENTARY NOTATION The views expressed in this thesis are those of the author and do not reflect the official policy or position of the Department of Defense or the United States Government.

17. COSATI CODES			18. SUBJECT TERMS (Continue on reverse if necessary and identify by block number)
FIELD	GROUP	SUB-GROUP	Internal Tide, Tidal Mixing, Internal Waves, Coastal Dynamics, Nonlinear Internal Wave Propagation, Shelf Break Tidal Dynamics

19. ABSTRACT (Continue on reverse if necessary and identify by block number)

Coastal currents and water column stratification frequently are determined by local phenomena that interact to produce complex dynamics. A process study was designed to assess the role of tides over a coastal shelf break as a local source of internal waves spatially-inhomogeneous, baroclinic residual currents, and internal mixing. The temporal evolution of three dimensional stratification and currents were characterized within a 4Km×4Km box close to the mouth of Monterey Canyon, California. Strong, baroclinic, unidirectional, spatially inhomogeneous jet-like currents were observed with 24 hour periods, together with the occurrence of semidiurnal thermocline oscillations and vertically mixed layers.

The linear theory of Baines (1982) predicts the existence of significant tidally forced internal waves in the area, with an interfacial mode at the thermocline decoupled from the internal waves propagating in the weaker stratification below. A ray tracing method is developed to study the nonlinear propagation of these tidally forced internal waves by considering wave advection and straining by the topographically controlled barotropic tidal flow while

22a. NAME OF RESPONSIBLE INDIVIDUAL T.P. Stanton	22b. TELEPHONE (Include Area Code) (408) 656-3144	22c. OFFICE SYMBOL OC/St

DD FORM 1473, 84 MAR   83 APR edition may be used until exhausted   SECURITY CLASSIFICATION OF THIS PAGE
All other editions are obsolete

UNCLASSIFIED

i

neglecting internal wave-wave interactions. It is found that nonlinear interaction of tidally forced internal waves with the topographically controlled barotropic tidal flow is a mechanism capable of forcing residual currents and internal wave shear instabilities that are capable of creating internal mixed layers similar to those observed at the mouth of Monterey Canyon.

Tidal Dynamics and Mixing
Over Steep Topography

by

Emanuel Ferreira Coelho
Lieutenant Commander, Portuguese Navy
B.S., Portuguese Naval Academy, 1983
M.S., Naval Postgraduate School, 1991

Submitted in partia' olfillment of the
requirements f   h= degree of

DOCTOR OF PHILOSOPHY IN PH SICAL OCEANOGRAPHY

from the

NAVAL POSTGRADUATE SCHOOL
June 1994

Accesion For		
NTIS CRA&I		☒
DTIC TAB		☐
Unannounced		☐
Justification		
By		
Dist.ibution /		
Availability Codes		
Dist	Avail and / or Special	
A-1		

Author: _____
Emanuel Ferreira Coelho

Approved by:

_____
Timothy P. Stanton
Associate Research Professor
of Oceanography

_____
James H. Miller
Associate Professor of
Electrical and Computer
Engineering

_____
Roland W. Garwood
Professor of Oceanography

_____
Robert L. Haney
Professor and Chairman of
Meteorology

_____
Edward B. Thornton
Professor of Oceanography
Committee Chairmain

Approved by: _____
Curt A. Collins, Chairman, Department of Oceanography

Approved by: _____
Richard S.Elster, Dean of Instruction

ABSTRACT

Coastal currents and water column stratification frequently are determined by local phenomena that interact to produce complex dynamics. A process study was designed to assess the role of tides over a coastal shelf break as a local source of internal waves spatially-inhomogeneous, baroclinic residual currents, and internal mixing. The temporal evolution of three dimensional stratification and currents were characterized within a 4Km×4Km box close to the mouth of Monterey Canyon, California. Strong, baroclinic, unidirectional, spatially inhomogeneous jet-like currents were observed with 24 hour periods, together with the occurrence of semidiurnal thermocline oscillations and vertically mixed layers.

The linear theory of Baines (1982) predicts the existence of significant tidally forced internal waves in the area, with an interfacial mode at the thermocline decoupled from the internal waves propagating in the weaker stratification below. A ray tracing method is developed to study the nonlinear propagation of these tidally forced internal waves by considering wave advection and straining by the topographically controlled barotropic tidal flow while neglecting internal wave-wave interactions. It is found that nonlinear interaction of tidally forced internal waves with the topographically controlled barotropic tidal flow is a mechanism capable of forcing residual currents and internal wave shear instabilities that are capable of creating internal mixed layers similar to those observed at the mouth of Monterey Canyon.

TABLE OF CONTENTS

ACKNOWLEDGMENTS

I. INTRODUCTION

A. MOTIVATION

Coastal currents and water column stratification are determined by local surface forcing, enhanced tides, rivers, topography and the coastal boundary, together with larger scale ocean dynamics. These characteristics determine and control circulation patterns and distinquish coastal regions from the deeper ocean. Recently, the development of industries related to the exploration of sea resources have increased significantly, and methods are now required to balance environmental impacts and industry needs. The increase in the strategic importance of these areas, where most of the interaction between man and the ocean occurs, should introduce some priority to understanding the dynamics of these coastal regions.

The study of specific mechanisms contributing to advection and mixing in coastal areas over irregular topography constitutes the broad objective of this research. This objective is fundamental to a large number of fields, including the study of sediment transport, pollutant dispersion, coastal air-sea interaction, marine biology, oil drilling, coastal engineering, and ocean acoustics.

A process study was designed to assess the role of tides and wind forcing on mixing and advection close to the continental shelf break, where steep topography and stratification are important. A 3 day surface mixing experiment was executed in September 1991 to assess some of the complex dynamics in Monterey Bay. An Acoustic Doppler Current Profiler (ADCP) and a Tow-yo CTD package was used to measure currents and stratification with approximately 200m horizontal resolution along a closed square path with 4Km legs, sampled approximately every 2 hours. The measurement site was on the southern side of the Monterey submarine canyon, close to the canyon mouth, over highly irregular topography ranging from 600 to 1500m depth (see Figure II-A.1). The complex dynamic interactions summarized in Figure I-A.1 were considered during this study.

A brief summary of the experimental observations which motivated this work follows. The winds were moderate throughout the observation period, resulting in a very shallow surface mixed layer. Strong spatial inhomogeneities in the upper ocean current and temperature structure were observed in the surveyed area. The analyzed oceanographic data suggest that the measurement box intersects an anticyclonic mean baroclinic flow of the order of $0.05ms^{-1}$. Strong baroclinic and spatially inhomogeneous northward jet-like features were observed 24 hours apart in the south-west portion of the

surveyed area. The maximum currents occurred between 50 to 150m, with 0.30ms^{-1} peak velocities. These jet-like pulses shallowed with time, reaching the surface at the end of the measurements.

Thermocline oscillations at tidal periods having amplitudes of up to 20m were observed at the north-west corner of the surveyed area. The internal wave field was characterized by an interfacial mode at tidal frequency and by smaller scale internal waves propagating in the stratified layer below the thermocline. Vertical thermocline oscillations were observed above the current maxima, with episodic vertically homogenized patches.

An internal mixed layer was observed within the thermocline, between 20m and 50m depth at the west part of the surveyed area, with strong entrainment of warmer water down into the internal mixed layer, occurring in an area of intensified vertical shear.

In the present work it will be shown that the internal tides (Baines, 1982; Huthnance, 1989) were responsible for the observed thermocline oscillations and for the occurrence of strong vertical shear. Furthermore, the nonlinear interaction of the internal tides and the topographically enhanced barotropic tide (Willmot, 1987; Maze, 1987; Pichon et al., 1990) will be studied using a numerical model to show that it is the probable cause of the strong baroclinic, spatially

inhomogeneous, unidirectional currents observed at the mouth of the canyon. Finally, the role of the tidally forced baroclinic velocity field in forcing strong mixing events (New, 1988), like the event observed during the MBAY experiment, will be discussed. This work is organized as follows. Chapter I describes the motivation and the scientific objectives. Chapter II, describes the Monterey Bay Mixing Experiment (MBAY) conducted in Monterey Bay in early September 1991, and the data processing methods used in the analysis. Chapter III discusses observations to motivate the hypotheses for the interpretation of the observed phenomena. Chapter IV presents the theoretical approaches; the linear theory of Baines (1982) is used first to estimate the magnitude of the forced fields, and then a ray tracing method is developed to study the propagation of the tidally generated internal waves; finally, a Richardson number criteria is used to estimate potentially unstable areas where mixing is likely to occur. Chapter V presents the conclusions and recommendations for future work, emphasizing the scientific contributions of the present development.

B. SCIENTIFIC OBJECTIVE

The oceanic tide is a barotropic phenomena that can be predicted locally (Gill, 1982). However, interaction with the coastal topography and stratification can result in mean tidal residual flows driven by potential vorticity conservation

mechanisms (Robinson, 1983; Mass et al., 1989a,b), which contribute significantly to changing the local advection patterns. Furthermore, the barotropic tidal motions interacting with the upper ocean stratification may also cause oscillations in density gradients, forcing internal waves groups which propagate away from the generation areas i.e., internal tides (Baines, 1982). These tidal forced internal waves are often non-linear (Willmott, 1987; Maze, 1987; Huthnanace, 1989), and may force mixing events by vertical shear instability mechanisms when the gradient Richardson number becomes sufficiently small (New, 1988). However, none of the existing theories account for the existence of the strong, baroclinic, unidirectional current pulses observed during the MBAY experiment.

To evaluate the importance of internal tides in the survey region, the tidally forced near-inertial internal wave field is estimated using the linear model of Baines (1982). The model uses idealized topography which approximates the continental slope close to the southern part of the Monterey Bay, and is forced by an estimated barotropic tidal field. The modeled velocity field is then compared with the MBAY observations.

To study near-inertial internal wave propagation on a non-stationary, inhomogeneous mean flow, a nonlinear numerical ray tracing method is developed, neglecting wave-wave interactions but retaining the advective and straining effects of the

underlying flow. This model also uses idealized topography approximating the continental slope in the southern part of Monterey Bay, and is forced with the Baines model internal wave field at the shelf break and by an estimated topographically controlled barotropic tidal flow. The interpretation of the numerical results emphasizes the existence of rectified baroclinic flow, which is comparable to the observed strong, baroclinic, unidirectional currents. The modeled velocity fields and observed mean stratification are also analyzed for the existence of potentially unstable internal shear layers, which could cause vertical shear instabilities and subsequent mixing.

The present work is based on the internal tide propagation linear models of Baines (1982) and New (1988), and on the non-linear studies of internal tides using layer models by Maze (1987) and Willmott (1987), where only the advection was considered. The primary contribution of this work is an extension of Kunze (1985), who studied the propagation of near-inertial internal waves on geostrophic shear, by considering the time variability of the underlying velocity field through which the waves propagate.

II. MONTEREY BAY MIXING EXPERIMENT

A. DATA COLLECTION

To obtain physical data and to study the photo adaptation of biological activity under the influence of advection and diffusion, the Monterey Bay Mixing Experiment (MBAY) was executed between 4-7 September 1991 in Monterey Bay under the sponsorship of the US Office of Naval Research, the Commander of Naval Oceanographic Command (CNOC), and the Monterey Bay Aquarium Research Institute (MBARI). Two ships, the RV "Point Sur" (sponsored by CNOC) and the RV "Point Lobos", and a Remote Operated Vehicle (ROV) from the MBARI, were used as platforms to deploy a Tow-Yo Conductivity-Temperature-Depth (CTD) profiler (5-80m depth, 0.25m bins), a CTD profiler (0-120m) with water sampling, two Acoustic Doppler Current Profilers (ADCP) (7-263m depth, 4m bins), a laser scanner with a high resolution video camera for direct bulk diffusivity measurements, a Coherent-Doppler-Velocity (CDV) package for microstructure measurements of shear, velocity, pressure, temperature and salinity, and two meteorological packages for the measurement of the atmospheric conditions and bulk air-ocean fluxes. Both ships used Global Positioning System (GPS) navigation with 50m accuracy. Simultaneous satellite Advanced Very High Resolution Radiometer (AVHRR) imagery and Coastal

Ocean Dynamics Application Radar (CODAR) maps were also analyzed to determine background conditions.

The RV "Pt.SUR" followed a closed square path with 4Km legs, repeated 27 times, over the Monterey Canyon above a highly variable ocean floor. ADCP velocity, temperature and conductivity profiles and meteorological data were recorded with spatial/temporal resolutions of 120m/60s (ADCP velocity), 360m/180s (temperature and conductivity) and 60m/30s (meteorological variables). The RV "Pt.Lobos" was stationed inside the closed path recording water velocity profiles and meteorological data, and controlling the MBARI ROV which measured bulk diffusivity and microstructure levels at selected depths between 10 and 50m. These measurements provided direct diffusion and turbulence estimates while simultaneously characterizing the internal wave field, tides, wind stress, and surface buoyancy fluxes. The full data set provided observations of mixing in surface and internal layers, while the evolution of the forcing mechanisms in a sub-mesoscale coastal region were identified. A sketch of the survey is shown in Figure II-A.1.

Section plots were made of the ADCP and Tow-Yo data from the RV "Pt.Sur" to show the evolution of the velocity components, temperature, salinity and water density profiles as the "Pt.Sur" traveled around the square box (one plot per box). Strong jet-like current features associated with layers of strong shear occurred periodically throughout the

observation period close to specific depths (surface, upper thermocline and lower thermocline), as shown in the example in Figure II-A.2. However, these strong velocity and shear events were only seen at the same locations within the small survey box, demonstrating the strongly inhomogeneous character of the velocity field.

Considering the temperature profiles of Figure II-A.3, the occurrence of isotherm deepening between profiles 472 and 475 within the strong vertical shear region (Figure II-A.2) suggests that a strong mixing event occurred. These mixed layers occur well within the pycnocline, suggesting they are not directly forced by atmospheric fluxes. Understanding how these strong shear layers appear and evolve is an important step in characterizing forcing mechanisms for mixing and diffusion in the area.

Well resolved temperature inversions were frequently observed within the thermocline; however, the water column was still hydrostatically stable as salinity compensation is occurring with the formation of cold and fresher water layers above warm and saltier water layers below, as the T-S diagrams of Figure II-A.4 show. These diagrams are displayed for two boxes 12 hours apart showing a general reduction in density in the water column, particularly at 30m depth where sigma-theta decreases from 25.7 to 25.2 with the water becoming warmer and fresher. The generation of new water types on these time

scales can only be explained by the occurrence of strong local mixing or by lateral intrusions at these depths.

The CDV and laser-scanner-video data from the ROV were processed separately because of their specific characteristics and scientific purpose. The results of the analysis of this data will be reported elsewhere.

B. DATA PROCESSING

After the preliminary processing and analysis, the RV "Pt.Sur" data discussed in the previous section were spooled to both the DOS and Unix environments for further processing using MATLAB software. To characterize the features mentioned in the previous section, the following methodology was employed:

1. Develop an Objective Analysis procedure to fit the survey data into a regular grid to facilitate comparison between different data types, allow uniform averaging of properties, and to assess the spatial and temporal characteristics of the observed features.

2. Process ADCP data using a reference layer to determine relative velocities and shear, and navigate the reference layer using the ship's Global Position System (GPS) data to estimate absolute current profiles.

3. Develop a spectral estimator to detect dominant propagating waves in the data, based on the repeated box

sampling method (time series following similar spatially closed paths).

4. Characterize and identify strong shear layers in space and time from the ADCP velocities and relate them to the stratification by estimating the gradient Richardson numbers.

5. Characterize the internal wave field, emphasizing near-inertial frequencies and tide components.

6. Identify mixing events and their temporal/spatial distribution using a Richardson number criteria.

7. Perform mass, momentum and vorticity balances.

1. Objective Analysis (OA)

To fit the ADCP and Tow-Yo data into a regular time and space grid, multi-dimensional interpolation methods are used. Ideally, these methods are based on correlation functions obtained from the data, requiring robust statistics and stationarity not seen in our observations. As the ADCP vertical sampling was made every 4m and the Tow-Yo sampling every 0.25m, the Tow-Yo data were smoothed and then decimated so that both data types were binned every 4m. Therefore, the OA was performed only in time and in the horizontal dimensions.

Based on the four corners, whose coordinates are given in Table II-A-1.1, four legs of a square were defined with 120 meter spatial sampling and 1 minute lags between consecutive samples along each leg. Several analysis methods were tested:

optimum interpolation, linear regression, least squares polynomial fit and inverse distance weights. Because of its form, well-based statistical assumptions, and easy generalization, the optimum interpolation method (Haltiner and Williams, 1980; Carter, et al., 1986) was chosen. In this method, it is assumed that the field at the grid points can be obtained from a linear filter operation applied to the neighboring observations of the type:

$$Y_{grid} + e_{grid} = \sum_{k=1}^{N} p_k Y_k^o \qquad (1)$$

where the Y's are the field values (observed and at grid points), e's are the error and the p's are the filter weights. Following a least-mean-square error approach and assuming that the data spans a stochastic vectorial subspace where the observed inner product is defined by the operator E[] (i.e., ensemble expected value); the least square condition requires the assimilation error vector to be orthogonal to the observed data vectors, i.e., error and measurements exist in orthogonal subspaces. Then

$$E[e_{grid}Y_j^o] = -E[Y_{grid}Y_j^o] + \sum_{k=1}^{N} p_k E[Y_k^o Y_j^o] = 0 \qquad (2)$$

Defining the correlation function (CF) as

$$CF_{k,j} = E[Y_k Y_j] \qquad (3)$$

12

and assuming a stationary and homogeneous field, the function CF can be normalized by the variance of Y. The solution of the least-square condition is the solution of a hermitian system of equations, with ones in the main diagonal and smaller absolute values elsewhere, in the form:

$$[CF_{k,j}]\underline{D} = \underline{CF}_{o,j} \tag{4}$$

(where square brackets stand for a matrix and underline for a vector). A potential problem for repeated samples, or for purely periodic fields is that they may generate a singular correlation matrix. A solution to this problem is to identify repeated or periodic samples and remove them from the observations before the analysis. Another approach is to use an eigenvalue threshold criteria that allows handling redundant observations, or ill conditioned matrices. This procedure, based on the singular value decomposition (SVD) (Strang, 1988; Haykin, 1989) allows any correlation matrix to be inverted and gives stable numerical results. Defining the pseudo-inverse matrix (PINV) (Strang, 1988)

$$PINV = Q^T \sum\nolimits^T Q \tag{5}$$

where $[CF] = Q \Sigma Q^T$, Q is the orthonormal matrix of the eigenvectors of $[CF]$ and Σ^T is a diagonal matrix with the inverse of the dominant square eigenvalues of $[CF]$ and zeros

13

for eigenvalues smaller than a threshold. The filter impulse response is given by

$$\underline{p} = [PINV] \underline{CF}_{o,j} \tag{6}$$

and the mean square error (MSE), normalized by the field variance, is

$$MSE = 1 - \sum p_k \underline{CF}_{o,k} \tag{7}$$

As the limited data sampling prevents an accurate estimate of the two dimensional, depth dependent correlation function of each variable from being estimated accurately, the common practice of using an appropriately behaved analytical correlation function has been implemented. Based on the correlation decrease with time and distance for non-periodic data, several functions can be considered and tuned for each specific application. In this work, the function displayed in Figure II-B-1.1, similar to that used by Carter, (1986), was used with 450m spatial and 15 minute temporal scales. These scales are based on the physical sampling scales and are not derived from the observations. This function was used in the optimal filter to weight the contributions of values in surrounding grid points. Valid data points were those with distances smaller than 500m and with time lags smaller than 15 minutes from each grid point. Grid points with no valid

14

contributions were marked as bad data. The RMS errors obtained from this filter operation are an indicator of the time/space distances of the data used at each grid point.

The "Pt.Sur" navigation was irregular with frequent stops in order to obtain CTD casts, and sometimes was more than 500m off course. This fact introduced frequent gaps and additional averaging and interpolation was required close to the CTD casts. Maps showing the vertical averages of RMS errors and the number of profiles used to evaluate each data grid point for each box are displayed in Figure II-B-1.2. The frequent stops of the ship appears as a high number of data points at a given location. After some of these stops the RMS error goes to one, corresponding to a data gap due to the time threshold. Nevertheless, these irregularities in the sampling rates are evenly distributed throughout all the surveyed area, so no significant bias is expected. However, the large periods and areas with no data can introduce some local aliasing, enhancing or attenuating spatial features. Care has been taken in the subsequent analyses to avoid using boxes with large data gaps.

After this data analysis, linear time interpolation was performed at each grid point so that instantaneous estimates of data fields over the full grid were available for analysis.

2. ADCP Velocities

The 64 bin ADCP velocity profiles were computed such that the first valid bin was centered at 7m depth, and velocities where estimated for each 4m bin when 75% of the acoustic returns were good within each 1 minute ensemble. As the raw current profiles were measured in the ship's reference frame rotated to a north/south coordinate system, the ship's velocity must be removed to estimate absolute currents. A commonly used procedure is to choose a reference layer and subtract its velocity from all the other bin velocities. This results in relative velocity profiles free of the ships velocity. Similarly, shear profiles will not be contaminated by the ship's velocity. These relative velocity data are useful for studying baroclinic features, like the shear events mentioned above; however, absolute velocities estimates are needed in order to assess barotropic tides, internal wave fields, mass balances over the full closed paths, and momentum and vorticity balances at specific locations.

The major problem in absolute velocity estimation is to obtain an accurate estimate of the ship's velocity. The ship's mounted GPS navigation system has a 50m accuracy for each independent position. However, by analyzing the navigated ship's velocity spectral characteristics displayed in Figure II-B-2.1, the velocity estimates are significantly more accurate. As the ship was usually traveling at a steady velocity along each leg, the observed high frequency

16

variability in the navigated speed was dominated by the GPS noise. After deglitching the data using a threshold value such that 95% of the data is assumed good, the standard deviation of the navigated ship's velocity associated with high frequencies (above 10 Hr^{-1}) is approximately 0.10m/s. This high frequency velocity variance has contributions from both real physical structure and the ship's positioning errors. Taking this into account, the GPS ship velocity was added to the ADCP vertical mean velocities to form an absolute velocity reference layer, after the reference layer was filtered by a fourth order, zero-phase Butterworth filter with a cut-off at 1/8 min^{-1}, to filter the high frequency noise. Another source of error, which must be taken into account when computing the ADCP (U,V) components, is that the true north does not correspond exactly to the direction used in the computations based on the ship's gyro compass. A heading correction was computed and implemented using correlation methods (Cheriskin, 1989). The resultant profiles of absolute velocities have a 95% error estimated to be +/-0.04m/s, based on the RMS value in the error band as shown in Figure II-B-2.1. Due to the observed highly inhomogeneous velocity field, some of the variance in the error band is probably due to the physical current structure. Therefore this error value slightly overestimates the true uncertainty, and the horizontal

17

velocity gradients are slightly smoothed due to the low pass filter.

With data in this gridded form, an analysis of the complex spatial and temporal time series was performed to develop the hypotheses which will be discussed in the following chapter.

III. HYPOTHESIS FORMULATION BASED ON OBSERVATIONS

A. DATA OVERVIEW

This section presents and discusses space-time series of the velocity and temperature fields observed during the MBAY experiment. The MBAY data are difficult to represent using traditional methods, so maps and section plots corresponding to snapshots, or time averages, of 14 different data fields have been used to present the highly inhomogeneous and non-stationary fields. Several complicated plots of variables showing examples of different spatial regions and times are used to characterize the features, which dominated the upper ocean during the measurement period. Due to the nature of the display, some of these figures show features that are not discussed in the text because they were found not to have a significant contribution to processes relevant to the present study.

The winds were moderate with magnitudes (W) below 5m/s throughout the entire observation period, with a sharp shift in direction at hour 154. The resulting wind stress was less than $0.04 \text{m}^{-1}\text{s}^{-2}\text{Kg}$, which corresponds to an unstratified mixing depth (h_*) of the order:

$$h_s = 10^{-2} \times h_f = 10^{-2} \times \sqrt{C_D} \times \frac{W}{f} \approx 20m \qquad (8)$$

where $C_D = 1.4 \times 10^{-3}$ is the drag coefficient and f is the Coriolis parameter.

The Ekman solution for the magnitude of the surface velocity (V_0) gives:

$$V_0 = \frac{\sqrt{2 \Pi \tau}}{D_e \rho f} \qquad (9)$$

where τ is the wind stress, ρ is the water density and D_e is the depth of frictional influence given by:

$$D_e = \pi \sqrt{\frac{2A_z}{f}} \qquad (10)$$

where A_z is the eddy viscosity. Based on the observed winds and for an homogeneous ocean, it can be assumed $A_z = 0.014m^2s^{-1}$ or smaller (Pond and Pickard, 1983 - p.109). Applying equation 9 for the observed conditions gives a maximum velocity at the ocean surface of about $V_0 = 0.035ms^{-1}$, which corresponds to a depth of frictional influence of about $D_e = 56m$.

However, the CTD observations showed strong stratification below 10m (as it will be discussed below), suggesting that the wind stress was distributed over a shallower depth. Assuming

20

a significant mixed layer depth of $h_e=D_e=10m$, the magnitude of the surface velocity is $V_0=0.20ms^{-1}$ and the corresponding slab current magnitude (i.e., velocity integrated over the depth of frictional influence) is about $0.04ms^{-1}$. Therefore, taking into account the 7m depth first bin ADCP current observation and the $0.04ms^{-1}$ accuracy of ADCP current observations, wind forced ocean currents are not likely detected in the MBAY current data.

Figure III-A.1, shows the time series of the winds during the experiment. Vertical lines represent the starting time of each path around the observation box (total of 27), and the hours of the predicted high and low tides are marked along the x-axis. These figures show that there is no consistent spatial variability in the wind between consecutive boxes, which could result in a significant wind curl capable of forcing vertical velocities at the mixed layer depth.

Some temporal variability can be observed, particularly in the wind direction, at hour 154. Assuming the extreme case of wind reversal over a 5km length scale, the maximum resultant Ekman pumping would force vertical velocities at the mixed layer depth of approximately,

$$W_e = \frac{\partial}{\partial x}\left(\frac{\tau}{\rho f}\right) \approx \frac{0.03}{5\times10^3\times1024\times0.87\times10^{-4}} = 6\times10^{-5}ms^{-1} \quad (11)$$

producing 1.5m maximum thermocline displacements if sustained over a 6 hour period. As the lateral wind gradients could not in fact be detected, W_e can be assumed to be negligible in this study.

The objectively analyzed, vertically averaged, current data temporally averaged over the full 3 days of the experiment (Figure III-A.2) show a weak anticyclonic mean flow of approximately $0.05m.s^{-1}$. The temporal mean net velocity entering the closed area is +0.018m/s indicating mean downwelling; however, this value is comparable to the measurement error. Stronger mean currents are observed along the west leg going northwestward, while weaker mean currents are seen along the east leg, but in the opposite direction. In Figures III-A.3 and III-A.4, the spatial structure of the temporal mean U and V velocity components show that the stronger currents in the south-west side of the surveyed area extend from 25 to 190m, reaching a maximum of about 0.25m/s at 70m depth. These strong mean baroclinic currents are not seen on the north-east side of the surveyed area.

To investigate the nature and possible sources of these highly inhomogeneous mean currents, the box mean divergence and circulation were estimated. These estimates are very sensitive to the ADCP 0.04m/s RMS velocity error, which in this case is dominated by the positioning system, as discussed in the previous chapter. Figure III-A.5.a shows a profile

time series of the depth distribution of the net velocity entering and leaving the surveyed area, normalized by the coriolis parameter and divided by the overall area, such that the units correspond to vorticity time changes. Magnitudes below $20 \times 10^{-9} s^{-2}$ can be assumed to be within the ADCP noise level. By continuity, the vertically averaged time series suggests that upward and downward vertical motions are present at the base of the box, approximately at tidal periods, although the small magnitude of the vertical mean divergence is not above the noise level of the navigated ADCP profile data. Nevertheless, the tidal cycle can be seen in the baroclinic structure of the estimates, for example at hour 150 and 30m depth, negative divergence values are observed opposing the deeper positive values along the same profile with magnitudes well above the noise level. At hour 162 positive divergence is observed between 20 and 130m depth with strong negative peaks above and below, and at hour 174 there is a strong negative divergence near the surface to 50m depth and positive divergence below. This divergence maxima should be associated with strong vertical velocities and be related to time increases in the vorticity magnitude. In Figure III-A.5.b, the box integrated along-track velocity are used as an indicator of the average vorticity inside the surveyed box, with magnitudes below $20 \times 10^{-5} s^{-1}$ within the ADCP noise level. Strong mean vorticity is seen in the profile at hour 150, with

23

positive maxima at 20 and 170m depths and a negative peak at 50m depth. The vorticity peaks at 20 and 50m depth are consistent with the negative divergence at the same hour at 30m depth. On the other hand, vorticity maxima are also observed at hour 134, 220m depth and at hour 172, 70m depth, suggesting that the layers of maximum vorticity are shallowing in time.

If the flow offshore is non-rotating and linear, some local source must be forcing the observed vorticity. Based on the value of the mixed layer slab velocity computed above and a 5Km length scale, the observed light and steady winds until hour 154 can produce a maximum divergence by Ekman pumping of $6 \times 10^{-6} s^{-1}$ (below the measurement error), so the observed wind field cannot explain the changes in divergence magnitude at 30m depth, and the observed tidal periodicity of the divergence peaks. Mechanisms based on the interaction of internal waves with tidal flow above steep topography may explain the observed vorticity (and divergence), and are analyzed in the next chapter.

The temporally averaged velocities in Figures III-A.2/3 have a strong northward component. To see the spatial and temporal structure of this flow, the north-south current component is displayed in Figure III-A.6 at four equally spaced points along the west leg. These figures show that the strong baroclinic residual velocities are associated with

24

bursts of kinetic energy 24 hours apart, most clearly seen in the profiles at location '1560m'. These jet-like events have maxima at approximately hour 142 (velocity event #1) and 166 (velocity event #2), between 50 to 150m and 30 to 100m depth respectively. They are unidirectional (towards northwest) with 0.30ms^{-1} peak velocities. The profiles at '2520m' and '3480m' show the first event with two local maxima in depth, one at 70m and the other at 150m; however, this pattern is not seen as clearly in the second peak at hour 166. The profiles at points '600m' and '1560m' suggest that similar velocity peaks occurred a few hours before the start of the data set at hour 120 and shortly after the end of the data set, although this last velocity maximum is shallower than the previous features and reaches the surface. This implies that the strong residual mean velocities in the west part of the box are a direct consequence of baroclinic, unidirectional, jet-like events occurring every 24 hours, which shallow with time. Such jet events did not occur on any of the other legs. This strong spatial inhomogeneity suggests that the jets could be correlated with the topography. Unfortunately, the surveyed area was not large enough to determine the south-west limit of the jets and to positively identify the maximum currents. Inspection of the four panels in Figure III-A.6 shows that the two initial events at hours 120 and 142, and the last event at hour 186 are stronger at locations '600m' and '1560m', however

the event at hour 167 at location '600m' is strongly attenuated. Comparing the time of the peaks of these events and the predicted tides in Monterey Bay (see Figure III-A.1), the maximum velocities occur during the ebb, corresponding to the maximum tidal flow.

Chapter III-B and III-C will present detailed discussions of the observations before the peak of the event at hour 142 (velocity event #1) and shortly after the peak of the event at hour 166 (velocity event #2).

B. VELOCITY EVENT #1

This section discusses the following features of the stratification and velocity profile time series, which characterize the physical processes in the surveyed area just prior to the jet-like feature observed at hour 142:

1 - Thermocline oscillations with tidal periods and amplitudes of up to 20m occurring at the north-west corner of the surveyed area.

2 - Strong vertical shear occurring below the thermocline, with a shallow upper layer not showing the same form of tidal dependence as the layer below. Unfortunately, no temperature(T) and salinity(S) data were available at the peak of this event or deeper than 80m.

The vertical structure of temperature around the sample box at hours 124 (flood) and 130 (ebb) in Figures III-B.1 and III-B.2 show thermocline displacements up to 20m during the 6

26

hour period at the west side of the sampled box with wavelengths larger than the box leg. These low horizontal mode displacements have larger amplitudes at the end of the west leg and at the start of the north leg. However, their propagation speed or wavelength are not well defined due to the 2 hour sampling time around the box perimeter. Because there are no obvious mechanisms to cause standing waves in the area, it is reasonable to assume that these oscillations are semi-diurnal, propagating internal waves with wavelengths longer than 10Km superimposed on the mean and tidal flows. Figure III-B.3.b displays time series contours of the V component of the current along the box sides at 19m depth, within the upper thermocline, showing a positive (northward) velocity at the west leg between hours 124 and 130. Furthermore, along the west leg, velocity changes in time with a semidiurnal periodicity are consistent with the period of the thermocline oscillations and with the assumption that these oscillations are the result of a propagating internal wave.

This type of thermocline oscillation is not as clearly seen in the other parts of the box; however, across the canyon (south leg at hour 124, south and north leg at hour 130 in Figure III-B.1/2), the spatial distribution of other groups of smaller scale (~1Km) internal wave isotherm displacements of about 10m can be seen superimposed on the larger scale features. The measurement time-space resolution and time

27

series lengths are not adequate to estimate their phase or group speeds.

The temperature profiles displayed in Figures III-B.1 and III-B.2 show the upper ocean is stratified to the surface so that no surface mixed layer is seen over much of the area. In fact, strong upper layer spatial inhomogeneities in the temperature profiles occur over the south and west legs. This stratified surface layer is consistent with upwelling conditions and the observed light winds shown in Figure III-A.1, which persisted throughout the measurements.

The current time series contour maps of Figures III-B.4.a/b and III-B.5.a/b summarize the spatial and temporal currents at 11m and 51m depths. Strong differences are evident between them. Before hour 156, the U component of the current displayed in Figure III-B.4.a suggests a mean value of about 5cm/s at 11m depth superimposed on the tidal cycle. The tidal current is most clearly seen in the V component plot in Figure III-B.4.b. For the same period, Figure III-B.5.b shows strong diurnal northward jets at 51m depth along the west leg superimposed with regular tidal cycles, seen in the U component plots of Figure III-B.5.a. The different behavior of the upper and lower layers before hour 156 suggests that different mechanisms are driving the residual currents, though both appear to be related to the tides.

C. VELOCITY EVENT #2

This section discusses the following features:

1 - A velocity peak at hour 167 with different characteristics from those discussed in the previous section.

2 - An internal mixed layer between 20m and 50m depth.

3 - The development of this internal mixed layer at hour 160, prior to the velocity peak of the event and following the wind shift at hour 154. There were no temperature and salinity data available between hours 134 and 166, or below 80m depth.

The large scale internal wave displacements of the thermocline described in the previous section are not seen in the vertical section snapshots of temperature in Figures III-C.1 at hour 168 and III-C.2 at hour 174. However, an internal homogenized layer is evident in the west and north legs at hour 168, between 15 and 50m depth (Figure III-C.1). This internal mixed layer is well developed at hour 162, prior to the peak of the event at hour 166 (see Figure III-C.3). Later, by hour 174, this layer has restratified as the velocities decreased (see Figure III-C.2 west and north legs).

Below and above this mixed layer, strong vertical temperature gradients are seen in the isotherm structure of Figures III-C.1 south and west legs, and Figure III-C.2 west and north legs. These figures also suggest that smaller scale internal waves might be present, but their signatures are not as obvious as those shown in the previous section.

A patch of warm water shown in Figure III-C.1, (west leg at position 1000m), displaced the 12°C isotherm downward by almost 40m. During this event at hour 168, the velocity jet following a 24 hour cycle along the west leg did not achieve the same magnitude as the previous jets (see Figure III-A.6-600m/2520 and 3480 panels).

The high magnitude 8 meter-scale vertical shear between 30m and the surface, displayed in Figure III-C.3 at hour 156 in the profiles at point '600m' in the west leg, is likely to have triggered the internal mixing event. This mixed patch was then seen as an internal mixed layer in the west leg when the T/S Tow-Yo measurements were resumed at hour 168, as displayed in Figure III-C.1.

Figure III-B.3.b displays time series contours of the V component of the current along the box sides at 19 meters depth, within the upper thermocline and near the depth of the mixing event observed in Figures III-C.1/2. The contours show that at approximately hour 156 there was a reversal (from northward to southward flow) of the north-south velocity component. This temporal change is in agreement with the upper layer velocity at 11m depth, as displayed in Figure III-B.4.b at hour 156, but is not observed in the deeper layers at 51m depth (Figure III-B.5.b) suggesting that the mixing event was triggered at this time due to a shear instability process related to an enhanced vertical shear. These observations

suggest that the observed internal mixed layer at hour 168 was associated with an instability mechanism at the thermocline related to the presence of the strong jet-like events. However, the data do not allow any conclusions about the exact triggering mechanism.

D. HYPOTHESIS FORMULATION

Based on the data discussed in the previous section, the measured weak winds cannot force the observed highly inhomogeneous and strong current field, high vertical current shear, or the observed semidiurnal thermocline oscillations.

On other hand, the fact that the measurement site was close to the mouth of the Monterey canyon suggest that canyon dynamics might be relevant. The effects of geostrophic flow over a canyon has been studied by Klinck (1988, 1989). He showed that narrow canyons, defined as those whose width is small compared to the internal Rossby radius of deformation (~15Km for Monterey canyon) (Koehler, 1990), will act as a barrier to barotropic transverse flow. Using the results presented by Klinck (1988) and the data of Koehler (1990), the time for geostrophic adjustment of the flow crossing the Monterey canyon can be estimated to be on the order of 1.5 hr, exciting waves over the canyon with frequencies 4 and 9 times the inertial frequency, and radiating waves from each side with frequencies 5 to 13 times the inertial frequency. The effects of stratification were discussed by Klinck (1989). For

narrow canyons like Monterey canyon, he predicts slower velocities over the canyon with a cyclonic circulation within the canyon and an anticyclonic circulation above. In contrast to the case of along-canyon flow (like the tidal flow), Klinck (1988,1989) suggests that the canyon will always affect the external pressure gradients, generating residual flows over the shelf. However, for the area covered in our survey, the cross-canyon geostrophic flow is expected to be much less energetic than the tidal flow, based on previous work in the area summarized in Breaker et al., 1989. This is confirmed by the unpublished current meter buoy data, kindly made available by C. H. Pilskaln (Pillsbury, et al., 1992) (see Figures III-D-1.a-d), which show strong tidal currents aligned along the canyon axis. As a result, the effects of geostrophic flow across the canyon on the generation of waves and residual flows is not likely to explain the MBAY observations.

Therefore, based on the discussion of the data presented in the previous section, the following hypotheses are established:

- Internal tides are being observed at the box survey site.

- The unidirectional, baroclinic, jet-like features are the result of rectifications of internal tides propagating below the thermocline

- The internal well-mixed layer discussed in the previous section is a result of an instability mechanism of the internal tide at the thermocline.

A detailed discussion of these hypotheses follows.

1. Tidally Generated Internal Waves

The barotropic tide interacting with the shallowing continental shelf topography forces vertical velocities as the horizontal tidal current magnitude increases. The pressure gradients established by the response of the stratified water column to these vertical velocities will force internal waves with tidal periods (internal tides). These internal waves propagate away from the shelf break, where the topographically generated pressure gradient forcing is maximum (Baines, 1982; Huthnance, 1989). The observed long wavelength thermocline oscillations discussed in III-B are consistent with a baroclinic interfacial mode within a 2-layer like upper ocean structure.

A. Review

Observations of internal wave perturbations propagating along the axis of the Monterey canyon have been reported by Shepard et al. (1974). They report phase velocities of about $0.25ms^{-1}$ for deeper water and of about $0.38ms^{-1}$ in shallower water. Internal tides over the California continental shelf have been observed at several locations (Huthnance, 1989). Shea and Broenkow (1982) observed large

33

tidally related isotherm displacements at the head of the Monterey canyon. Their observations suggest that strong internal tides should exist in the area, but their data were not sufficient to allow a full regional characterization.

Baines (1983) used a laboratory experiment to study tidal motions over submarine canyons. He described a process by which the internal tide amplitudes can be enhanced inside narrow canyons (defined as canyons whose width is much smaller than both the tidal wavelength (~200Km) and the barotropic Rossby radius of deformation), so that the canyon will have negligible effect on the pressure gradients established by the barotropic motion. Therefore, the tidal motions inside topographical features like the Monterey canyon will be forced by the same pressure gradients that exist over the continental shelf, and by a common pressure gradient established at the canyon head, leading to an enhanced transport inside the canyon (Huthnance, 1989). This type of pressure gradient supports the conceptual model proposed by Shea and Broenkow (1982) of cold deep canyon water being lifted by the tides and intruding onto the shelf by the established horizontal pressure gradients. At the MBAY measurement site the topographic slope is much larger than the internal wave slope, as will be shown in the next chapter. For this situation, Baines (1983) predicted an enhanced internal tide up-canyon and near the bottom, verified by observations of strong internal tides by Shea and Broenkow (1982) at the canyon head.

He also predicts that the tidal flow should be strongly baroclinic. For this case, Huthnance (1989) also suggests that the tidal flow will show a complex spatial dependence. Based on the theory by Grimshaw et al. (1985), reflections at the open mouth can contribute to this intensification, especially for steep slopes and narrow canyons.

Because the MBAY survey area is located close to the canyon mouth (but not within the canyon), it can be assumed that the internal tide dynamics will be very similar to those over the open shelf, and the effects of the canyon can be viewed as having higher order effects. Current meter buoy data (Pillsbury, et al., 1992) displayed in Figures III-D-1.a-d, show the tidal flow at 500m depth close to the surveyed area (as shown in the map in Figure II-A.1) to be largely aligned along the canyon axis. Significant isotherm displacements with tidal periods are clearly seen in the temperature data, confirming the importance of tidal dynamics in the area.

B. Problem

To identify the sources for internal waves and to characterize the mesoscale and tidal circulation in the area, simultaneous observations would be needed at several locations along the canyon, along the shelf, and on the continental slope. Nevertheless, the significant along canyon tidal flow identified in both these data and in the current meter mooring data allows some simplifying assumptions to be made in

35

isolating the tides as a primarly source of internal waves in the area. Other mechanisms will be assumed to modulate the tidal dynamics on a longer term (at least several days) or as higher order much less energetic effects.

Other potential problems in the analysis of internal tidal forcing is the possibility of multiple reflection effects inside the canyon and modification of the internal wave field by pressure gradients established by residual flows. However, because our measurement box is at the canyon mouth, the assumption that the observed dynamics are similar to those on the continental slope is justified to a first approximation and the effects of local pressure fields can be regarded as an higher order correction, superimposed on the larger scale response.

The characterization of the barotropic tides in the area will also require some special care. Unfortunately, no complete regional study of the tides exist for the area.

C. Approach

To evaluate the internal tide forcing in the area, the linear model developed by Baines (1982) is used in the next chapter to estimate the magnitude of the forced internal wave field on a regular, straight, continental slope with representative model parameters for the survey area.

To better simulate the observed data and to take into account some of the enhancements which might occur due to the presence of the canyon, the barotropic tidal flux will be

36

assumed to have 0.05m/s amplitudes at 1000m depth, increasing as depth decreases, and generating vertical velocities at the bottom boundary by continuity. The resulting vertical velocities decrease linearly with height towards zero mag¡ .de at the sea surface.

2. Tidal Rectification

Non-linear effects of the barotropic tides interacting with topography and the internal tides result in spatially inhomogeneous residual currents. Therefore, it is hypothesized that the unidirectional, baroclinic, jet like features observed on the west leg of the surveyed box are caused by rectification of the internal tide due to non-linear effects. It is further hypothesized that the nonlinearities are dominated by internal tides interacting with the topographically enhanced barotropic tidal flow (assumed to be a free shallow-water gravity wave) and the water column stratification. These hypotheses will be justified in the following sections, and tested in a model described in Chapter IV.

A. Review

Tides are a periodic phenomena, which ideally have zero mean velocities over long periods. However, due either to ocean floor topography, frictional effects, or to the coastal shape, there are processes that can rectify tidal currents resulting in spatially inhomogeneous mean currents. Tidal

rectification has been shown to be due to non-linear effects and friction in a homogeneous ocean (Robinson, 1985; Mass et al., 1987; Garreau et al., 1992), and to non-linear effects on a baroclinic tidal flow associated with the internal tides (Maze, 1987; Willmott, 1987; Pichon et al., 1990; Mass et al., 1989a,b).

Following Robinson (1985), rectified flows are typically one or two orders of magnitude less than the tidal current velocities, requiring special care in observation and modeling. Robinson identifies the non-linear interactions as the main process by which residual vorticity can occur, and presents four vorticity generation mechanisms which play an important role in coastal dynamics, as shown in the Figure III-D.2.a:

- potential vorticity conservation (column stretching and squeezing);
- differential friction due to horizontal shear;
- differential friction due to lateral depth gradients;
- asymmetrical depth profile changes.

For surface displacements small compared to depth, small residual flows result (compared to the tidal currents) with a relative vorticity much larger than the planetary vorticity (assumptions likely to be valid for the MBAY data considering the vorticity estimates of Figure III-A.6). Zimmermann (1978, 1981) used a simplified potential vorticity

equation to conclude that residuals are determined by a balance between generation by tidal advection and dissipation by turbulent eddy diffusion. He found that maximum residual vorticity occurs over topographic features with length scales comparable to the tidal excursion. For the case of the continental slope near Monterey, the typical topographical length scale of about 5Km is comparable to a tidal excursion length of about 3.5Km for 10cm/s tidal currents, suggesting that these mechanisms might be relevant in the area. The tidal excursion length (L_T) is defined as

$$L_T = 2 \; \frac{u_{tide}(x)}{\omega} \tag{12}$$

where 'ω' is the tidal frequency. Using similar assumptions, Robinson (1981) observed using simplified numerical solutions in a quasi-lagrangian sense the following features:

- vorticity effects cannot penetrate further than the tidal excursion;

- vorticity can propagate normal to the tidal streamlines only by eddy diffusion processes;

- because vorticity is dissipated within one tidal time scale, it cannot be advected further than the length of the tidal excursion, so the

areas of influence of topographic features is limited;

- tidal advection of a gradient of tidal vorticity is the mechanism by which residual vorticity is generated.

Also by running simplified numerical solutions in a Eulerian sense, including only the stretching mechanisms terms, he found that:

- positive mean vorticity is generated in deeper water and negative mean vorticity is generated at shallower depths;

- the maximum generation of residual vorticity occurs when the topographic length scale is similar to the local tidal excursion.

He estimated the maximum residual vorticity (ξ_0) in a shallow sea due to column stretching to be

$$\xi_o \approx 0.45 \frac{fV}{\omega h} \frac{\partial h}{\partial s} \qquad (13)$$

In the same way, considering only bottom friction, he found that the maximum residual vorticity in shallow seas to be

$$\xi_o \approx 0.4 \frac{C_b V}{\omega} \frac{\partial}{\partial n} \left(\frac{V}{h} \right) \qquad (14)$$

where 'V' is the tidal stream amplitude in the 's' (streamline) direction, 'n' is the direction normal to 's', "C_b" is the bottom friction coefficient, 'f' is the planetary vorticity, and 'h' is the water depth. Based on these results, residual vorticity patterns can be drawn for a specific location and the mean residual flow estimated.

In the case of Monterey Bay, depths range from 1000m to 100m over distances of 5000m, corresponding to very large slopes of approximately 15% and 100% depth changes within one tidal excursion (~3.5Km). However, despite this strong topography, barotropic tidal currents at these depths ranges are expected to be smaller than $0.50ms^{-1}$, so that column stretching will be the mechanism likely to generate tidal residual flow. The rectified flow will be maximized for topographic lengths equal to the tidal excursion i.e., $\Delta s \sim V/\omega$. For this case and for typical values in the continental slope close to Monterey, the maximum residual vorticity will be bounded by $\xi_0 \sim 0.45 f (\Delta h/h) < 3.6 \times 10^{-4} s^{-1}$, corresponding to maximum residual flows smaller than $v \sim (\xi_0 . L_T)/4 \sim 0.05 ms^{-1}$ for shallow waters and $v \sim 0.005 ms^{-1}$ for the deep water. Figure III-A.5 shows a residual mean vorticity of about $3 \times 10^{-4} s^{-1}$ in the surveyed area, indicating a good agreement with this theory. However, the observed residual vorticity has a strong depth dependence indicating that the barotropic assumption is not fully valid.

41

This slow rectified flow will result from northward currents along the continental slope with shallow water on the right. This simple analysis suggests that barotropic tidal rectification may play some role in the dynamics of Monterey Bay. However, the small magnitudes of the rectified flows fall within $0.02-0.04ms^{-1}$ noise floor of our observations.

More accurate theoretical and numerical models for barotropic tidal rectification have been developed by Mass et al. (1987) and Garreau (1992) among others. They better simulate the effects of stronger non-linearities that are expected to occur over steep slopes. Garreau (1992) defines a non-dimensional parameter indicating non-linearity as L_T/L_{T_0} where

$$L_{T_0} = h(x) / \frac{dh}{dx}$$
(15)

A typical value of L_{T_0} for the continental shelf close to Monterey Bay is 35Km, so L_T/L_{T_0} is of the order of 0.1, comparable to values in the Celtic Sea where strong and spatially inhomogeneous mean currents of the order of $0.05ms^{-1}$ have been observed. The Celtic sea residual flows have been attributed to tidal rectification processes and this site also has internal tides predicted (Baines, 1982) and observed (Huthnance, 1989), although different length scales apply.

Non-linear layer models have been developed by Maze (1987) and Willmott (1987) to study the effects of advection by the barotropic tides. Significant residual currents are predicted in the upper layer changing within the length scales of topography (L_w) and the internal wave scale (depth/c), where 'c' corresponds to the slope of internal waves for a typical stratification. It will be shown in the next chapter that this last scale is O(3Km) for the data set under discussion. The simplest analysis for weak non-linearities predicts typical mean currents to be on the order of (Huthnance, 1989):

$$\frac{A^2}{\omega L} \tag{16}$$

where 'A' corresponds to the internal wave current amplitudes and 'L' the significant length scale. It will be shown in the next chapter that current oscillations are predicted with amplitudes of about $0.1ms^{-1}$ for the interfacial mode in the MBAY data set. This amplitude will result in residual velocities of $0.02ms^{-1}$ in the upper layer and $0.002ms^{-1}$ in the lower layer of an idealized 2 layer system. The velocities of the forced internal waves in the stratified continuum below the thermocline will be estimated in the next chapter to be approximately $0.15ms^{-1}$, resulting in residuals of about

0.09ms^{-1}. Therefore, advection by the tidal flow appears as a significant source for baroclinic tidal rectification.

The non-linear modal approach for a stratified ocean by Mass and Zimmermann (1989a,b) showed that, though there were many features in common with the homogeneous case developed above, a bottom residual current intensification can be also observed. They found a depth dependent relative vorticity produced by vortex stretching of free internal modes causing bottom enhanced residual vorticity. In fact, the vertical structure of vorticity was found by them to be exponential rather than sinusoidal. They also found evidence for bottom intensified cross-isobath circulation due to baroclinicity and along-slope baroclinic currents extending for greater distances than for the barotropic counterpart. Their results are supported by observations from the continental slope near northwest Africa discussed by Gordon (1980) and Huthnance et al. (1982) where the internal tide was observed to be bottom intensified. Although this mechanism supports bottom current intensification, it does not predict the current profiles observed in the MBAY experiment where the stronger currents were observed between 50 and 150m depths. Also, the buoy data at 500m, described above, does not show any evidence of intensification with depth as would be required if Mass and Zimmermann mechanisms were to be relevant to the MBAY observations. Thus, although these measurements do

44

not allow any conclusion about the existance of bottom intensified currents, this mechanism cannot explain the MBAY observations.

B. Problem

None of the theories mentioned above seem to account for the occurrence of the observed, strong, unidirectional, diurnal, baroclinic jets, although the non-linear interaction of finite amplitude internal waves generated at the thermocline with the barotropic tidal flow appears to be a likely mechanism. Because the currents of the observed jets are approximately $0.30ms^{-1}$, some amplification mechanism must also exist. As these jets did not occur as a bottom current enhancement (they decay below 150m depth) mechanisms other than the baroclinic vortex stretching discussed by Mass et al. (1989) are present.

C. Approach

Kunze (1985) showed the importance of including straining together with advection by the mean flow when analyzing the propagation of near-inertial internal waves. A ray tracing model based on this approach is developed in the next chapter to study the evolution of baroclinic internal waves generated close to the thermocline by the barotropic tides, using an idealized continental slope with values representative of those either side of Monterey canyon. The extension to Kunze's work is the inclusion of vertical

boundaries and the time dependent component in the mean flow, which in our case is assumed to be the barotropic tide. Also a second order result is calculated by computing the wave-action along the rays, defined as the ratio of the wave energy to the Eulerian frequency. Wave-action was proved to be a Riemann invariant (see Whitham, 1974) for internal waves by Bretherthon et al. (1969), and can be used to estimate the wave amplitude along characteristics.

3. Internal Tide Instabilities

The last hypothesis is that the vertical shear supplied by baroclinic rectifications, both on the interfacial thermocline mode and on the internal waves that are propagating in the stratified continuum below, will supply sufficient energy for shear instabilities to occur within the thermocline. Several examples of these strong internal mixing events were observed in the MBAY measurements (see Figure III-C.1).

A. Review

Internal waves are oscillations about an equilibrium state within the interior of a stratified fluid. Their main restoring force is buoyancy, and depending on their length scales, rotational effects in an f-plane will be significant for near-inertial frequency internal waves like internal tides. The presence of lateral boundaries and topography may introduce extra constraints (LeBlond and Mysak,

1972; Gill, 1982). Internal waves in the open ocean have been extensively observed and studied in the past twenty years (see for example Levine, 1983; Muller, et al., 1991).

Based on the current knowledge about internal waves, Garret and Munk (1975) developed an analytical, random phase, linear model (GM75) describing a background continuum of wave energy that has been successfully compared with oceanic observations, and is now a widely accepted standard for comparison and analysis. Deviations from this background continuum can usually be associated with particular generation mechanisms. The evolution towards a GM75 spectral shape is explained by three classes of non-linear resonant interacting triads: elastic scattering (forced vertical symmetry), parametric sub-harmonic instability (transfer of energy towards smaller scales at near-inertial frequencies) and induced diffusion (diffuses wave action in wavenumber space forcing the high wavenumber spectrum to an equilibrium shape) (McComas, et al., 1977; Phillips, 1960).

The frequency band for internal waves has a range limited between the inertial and the Brunt-Vaisaala frequencies, although near-inertial waves with frequencies lower than inertial (Kunze, 1985), and waves with frequencies above N (Lamb, et al., 1992) are possible due to wave-mean flow interactions and horizontal inhomogeneities.

Non-linear interactions of internal waves have been identified as possible sources of mixing within the ocean

47

interior (Gregg, et al., 1986; Caldwell, 1987; New, 1988; Kunze, et al., 1992).

In coastal waters strong departures from the GM75 spectrum might be expected due to the generation of internal tides, the effects of topography, the presence of a lateral boundary and complicated wind regimes, all of which are thought to change the wave field and induce strongly non-linear conditions.

The following analysis follows Leblond and Mysak (1978, sections 42 and 43) in the discussion of the basic theory for stability of internal waves, neglecting rotation. The Taylor-Goldstein equation, derived from the two-dimensional, linearized perturbation equations (p. 398), describes internal waves superimposed on a mean vertical shear:

$$[\rho_0(U - C)w']' - (\rho_0 U'w)' - [\frac{\rho_0'g}{U - C} + \rho_0 k^2(U - C)]w = 0 \qquad (17)$$

where '$\rho_0(z)$' is the non-perturbed density, '$U(z)$' is the mean current, 'C' is the phase velocity, 'w' is the vertical velocity, 'g' is the gravity acceleration, 'k' is the horizontal wavenumber, and primes represent vertical derivatives. This equation can be used to describe the onset of shear flow instabilities as predicted by a linear analysis.

48

For a two layer ocean, with $U=U_1z/h$ (h being the layer depth) in the upper layer and no mean flow in the deeper layer, equation (17) reduces to:

$$w'' - k^2w = 0 \qquad (18)$$

in each layer, providing $U-C \neq 0$. This yields solutions of the type:

$$w = \begin{array}{l} Ae^{kz} + Be^{-kz} , \quad 0 < z \leq H \\ De^{kz} , \quad -\infty < z < 0 \end{array} \qquad (19)$$

where A, B and D are constants determined by the matching conditions at the interface:

$$[\frac{w}{U - C}] = 0$$
$$\qquad\qquad (20)$$
$$[\rho_0[(U - C)w' - U'w - gw/(U - C)]] = 0$$

The kinematic and pressure conditions at the surface combine to give:

$$(U - C)^2w' - (U - C)U'w - gw = 0 \qquad (21)$$

For a non trivial solution, they arrived at the following eigenvalue equation for 'c':

$$[(U_1 - C)^2 k - g)(\Delta(c^2 k - g) + (U_1 - C)^2 k + g) +$$

(22)

$$+ e^{-2kH}[(U_1 - C)^2 k + g][\Delta(c^2 k - g) - [(U_1 - C)^2 k - g]] = 0$$

where $\Delta > 1$ is the ratio between the layer densities. This equation has four real roots, or two real roots and a complex conjugate pair of roots. In the latter case, one of the complex roots generates a time growing (unstable) solution, such that the flow becomes unstable. Therefore, the stabilizing effect of stratification is not always enough to prevent the overturning tendency induced by the shear flow.

If we take the limit as $H \to \infty$, the eigenvalue equation for C takes the form:

$$[(U_1 - C)^2 k - g][\Delta c^2 k + (U_1 - C)^2 k - g'] = 0 \qquad (23)$$

The first factor represents surface gravity waves being advected by the mean flow ($C = U_1 \pm (g/k)^2$), while the second factor represents the Kelvin-Helmholtz result:

$$C = \frac{\rho_1 U_1}{\rho_1 + \rho_2} \pm [\frac{g}{k}\frac{\rho_2 - \rho_1}{\rho_2 + \rho_1} - \frac{\rho_1 \rho_2}{(\rho_1 + \rho_2)^2}U_1^2]^2 \qquad (24)$$

or

$$C = U \pm \left(C_l^2 - \frac{\rho_1 \rho_2}{(\rho_1 + \rho_2)^2} U_1^2 \right)^{1/2} = U \pm s \qquad (25)$$

This result shows interfacial short waves moving relative to the weighted mean flow U with speed $\pm s$, provided that $s^2 > 0$; if not, C is complex and the flow becomes unstable. This condition is valid for small density differences and the stability criteria is:

$$Rk^{-1} = g \frac{\rho_2 - \rho_1}{\rho_1 U_1^2} > \frac{1}{2} \qquad (26)$$

(and $< 1/2$ for instability). The value Rk^{-1} represents a Richardson number (Ri), based on the wavenumber of the disturbance. This inequality reflects the stabilizing effect of stratification that is required in order to inhibit the overturning tendency introduced by the vertical shear.

Now consider a continuously stratified fluid and take the Taylor-Goldstein equation assuming a rigid lid at the surface, $N^2 = g\rho'/\rho$ (Brunt-Vaisaala frequency), $w = FW$, $W = U - C$, where $F(z)$ is a new dependent variable, and the following equation is obtained:

$$(\rho_0 W^2 F')' + \rho_0 (N^2 - k^2 W^2) F = 0 \qquad (27)$$

Now if F is an unstable solution, C is complex and $W \neq 0$. Using the substitution $F=G/W^{1/2}$, where G is another independent variable and depth integrating the equation, the following condition for a zero imaginary part is obtained:

$$C_i [\int \rho_0 (|G'|^2 + k^2 |G|^2) + \int \rho_0 | \frac{G^2}{W} | (-\frac{1}{4} U^2 + N^2)] = 0 \qquad (28)$$

Therefore, $C_i > 0$ (unstable waves) implies $-1/4 U'^2 + N^2 < 0$ for some range of z i.e., for $U' \neq 0$ the sufficient condition for stability on a stratified shear flow is:

$$R_i = \frac{N^2}{U^2} \geq \frac{1}{4} \qquad (29)$$

known as the Miles' theorem for stability. It states that if the stabilizing influence of stratification dominates the destabil ing influence of the shear, the flow is stable.

From the linearized perturbation equations, the following energy budget is obtained (p. 409):

$$\frac{D_0}{Dt} \{ \frac{1}{2} \rho_0 (u^2 + w^2) + \frac{1}{2} \rho_0 N^2 \zeta^2 \} = -(pu)_x - (pw)_z - \rho_0 uwU' \qquad (30)$$

where u is the horizontal velocity and p the pressure and ζ is the vertical particle displacement. Assuming that the quantities are periodic in the horizontal, and averaging over

one wavelength, the depth integrated energy transfer equation is obtained (horizontal averages will be denoted by $E[\,]$):

$$\frac{\partial}{\partial t}(T + V) = P + Q \tag{31}$$

where

$$T = \frac{1}{2}\int_{z_1}^{z_2}\rho_0 E[u^2 + w^2]dz \tag{32}$$

is the perturbation kinetic energy,

$$V = \frac{1}{2}\int_{z_1}^{z_2}\rho_0 N^2 E[\zeta^2]dz \tag{33}$$

is the perturbation potential energy

$$P = -pw\Big|_{z_1}^{z_2} \tag{34}$$

represents the work done by the external pressure at the boundaries, and

$$Q = \int_{z_1}^{z_2}\tau_{13}U'dz \tag{35}$$

53

is the rate of energy transferred between the mean and the perturbed flow by the Reynolds stress:

$$\tau_{13} = -\rho_0 E[uw] \qquad (36)$$

This equation shows that when an instability occurs, ($[T+V]_t>0$), energy is transferred from the mean shear towards the perturbation flow, resulting in a loss of mean kinetic energy.

In fact, Holt, et al. (1992) using direct numerical simulations observed that, for a Richardson number (Ri) below critical, the Reynolds stress and vertical density flux are down-gradient, and some of the vertical kinetic energy gained through production is transferred to potential energy. As Ri becomes higher than critical, there is a release of potential energy towards the vertical kinetic energy. Some of this energy is then redistributed to the streamwise kinetic energy.

There are other mechanisms by which internal waves can break (Leblond and Mysak, 1978, p. 408). The dynamical gravitational instability, in which the vertical density gradient associated with large amplitude internal waves becomes positive, is a non-linear instability that occurs when the particle velocity exceeds the wave phase velocity. Another possibility is the development of turbulence from decreases of the density gradient due to local steepening of isopycnals.

Finally, there are some experimental results showing overturning occurring when large amplitude waves encounter a discontinuity in the density profile.

B. Problem

Once the main source of vertical shear is found, shear instabilities can be predicted for real or idealized stratification profiles in the surveyed area using Miles' criteria (Ri > 1/4) for stability, and compared with the occurrence of internally homogenized layers in our observations. Also, by estimating the amplitudes and phase velocities of the internal tides, potential dynamical instabilities can be identified.

C. Approach

Gradient Richardson number criteria are calculated for the instantaneous internal tide baroclinic field that is modeled in the next chapter to estimate areas where mixing are likely to occur. The number of occurrences of critical conditions during a 24 hour cycle are mapped for a continental slope, similar to MBAY conditions, and comparison with the observations are made.

IV. THEORETICAL APPROACH

A. INTERNAL WAVE GENERATION (BAINES, 1982)

This section describes the internal tide generation model of Baines (1982), applied to conditions typical of the continental shelf close to Monterey Bay, to assess the importance of internal tide generation processes in the MBAY area, and to compare with the MBAY observations. A simplified 2-D continental slope geometry and barotropic tide will then be used to estimate tidally forced internal waves at the shelf break. These internal wave sources will then be used to force the nonlinear internal wave propagation model developed in the next section.

The governing equations for the internal tide generation problem are:

$$\rho_0 \frac{\partial \overline{U}}{\partial t} + \rho_0 \ \overline{f} \times \overline{U} + \nabla p + \rho g \overline{z} = 0$$

$$\frac{\partial \rho}{\partial t} + w \frac{\partial \rho_0}{\partial z} = 0 \tag{37}$$

$$\nabla . \overline{U} = 0$$

where the overlines represent vector quantities, 'U' is the velocity field, 'ρ_0' is the density in static equilibrium and 'ρ', 'p' are the perturbed density and pressure relative to

56

the hydrostatic equilibrium. Assuming that the velocity and pressure field can be separated into barotropic and internal tide components, these equations can be written in the following form:

$$\frac{\partial \overline{U}_j}{\partial t} + \overline{f} \times \overline{U}_j + \frac{1}{\rho_0}\nabla \overline{p}_j + \frac{\rho_j\, g\overline{z}}{\rho_0} = \overline{F} = -\frac{g\rho_1}{\rho_0}\overline{z}$$

$$\frac{\partial \rho_1}{\partial t} = -w_1\frac{\partial \rho_0}{\partial z}$$

(38)

where 'F' represents the generation force for internal motion. The amplitude of the forcing term can be written in the following way, assuming one dominant component in the time dependence of the barotropic tide:

$$F = -\frac{g}{\rho_0}\frac{\partial \rho_0}{\partial z}\frac{w}{\omega_T} = N^2\frac{w}{\omega_T}$$

(39)

where 'ω_T' is the principal tidal frequency that will be assumed to be $2.\pi/12.42hr^{-1}=1.4 \times 10^{-4}s^{-1}$. The Brunt-Väisälä frequency is maximum at the thermocline with magnitudes of the order of $2 \times 10^{-2}s^{-1}$, decreasing as the stratification weakens with depth towards values of the order of $2 \times 10^{-3}s^{-1}$ for the MBAY case (see Table IV-A.1). The semidiurnal forcing frequency ω_T is much smaller than the Brunt-Väisälä frequency close to the thermocline and of the same order of magnitude as the inertial

frequency 'f', which is $0.87 \times 10^{-4} s^{-1}$ for the latitude of Monterey Bay; therefore, solutions to this problem can be assumed to be dominated by near-inertial internal waves (Kunze, 1985).

For a typical 2-D continental slope shallowing eastward (positive x-direction) with a topographical length much smaller than the barotropic tide scales (~200Km), the propagation aspect of the barotropic tide can be neglected, and the tidal flux can be assumed to be constant. The scaling conditions are well met for Monterey Bay even though the 2-D approximation oversimplifies the topography. By energy conservation, the amplitude of the horizontal barotropic velocities over the slope for a homogeneous ocean for these conditions is given by:

$$U(x) = \frac{U_T \cdot h\infty}{h(x)} \qquad (40)$$

where 'U_T' is the oceanic tide velocity amplitude, 'h_∞' is the depth offshore and '$h(x)$' the depth over the continental slope. Using continuity, with no lateral boundaries and no normal flow perpendicular to the vertical boundaries, the barotropic velocity interacting with the continental slope forces vertical motions with amplitudes given by:

58

$$W(x,z) = U(x)\frac{dh}{dx}\frac{z}{h(x)} \qquad (41)$$

Representative values in the neighborhood of the surveyed area during the MBAY experiment were $U_T=0.05m/s$, $dh/dx\approx0.18$ (slope) with depths ranging from $h(0)=100m$ to $h_\infty=1000m$ over a 5000m horizontal distance across the slope. Figure IV-A.1.a/b represents x/z sections of the resultant velocities for the cross-shore (u) and vertical(w) velocity components. For a strong thermocline as observed during MBAY, this velocity field, will produce a maximum internal tide forcing close to, but below the thermocline at the shelf break, as Figure IV-A.1.c shows.

Defining a stream function (ψ) as $u_I=-\psi_z$ and $w_I=\psi_x$ where the subscripts 'x' and 'z' represent partial derivatives, a forced wave equation can be derived:

$$\nabla^2\psi_{tt}+N^2\psi_{xx}+f^2\psi_{zz} = QN^2z\left(\frac{1}{h}\right)_{xx}\cos(\omega_T t) \qquad (42)$$

where 'Q' represents the tidal flux assumed to be $Q=U_T h_\infty$. For a typical solution of the form $\psi=\Psi(x,z)\exp(-i\omega_T t)$ we obtain:

$$\Psi_{xx} - c^2\Psi_{zz} = \frac{Q}{1 - \dfrac{\omega_T}{N^2}}\, z\left(\frac{1}{h(x)}\right)_{xx} \qquad (43)$$

where the boundary conditions are $\Psi=0$ at $z=0$ and $-h(x)$, and 'c' represents the semidiurnal internal wave slope (ratio of horizontal and vertical wavenumbers) given by:

$$c^2 = \frac{\omega_T^2 - f^2}{N^2 - \omega_T^2} \qquad (44)$$

The internal wave slope for the MBAY data will be minimum at the thermocline with a magnitude on the order of 0.006 for an interface temperature drop of $3^\circ C$ (Figure III-B.1), increasing with depth to 0.06 as 'N' approaches $2\times10^{-3} s^{-1}$, below the thermocline (see Table IV-A.1).

A solution for the homogeneous problem can be generated in terms of an infinite set of normal modes, assuming a density interface at depth '-d', with a constant 'N_0' below, and a constant depth. These modes will be determined by the eigenvalues satisfying the relation:

$$(\kappa_n^2 R^2 S - K)\tan(\kappa_n(1 - R)) = \kappa_n R \qquad (45)$$

where

$$R = d/h = 0.2$$

$$S = \frac{g\Delta\rho_0}{d\rho_0}/(N_0^2 - \omega_T^2) = 35$$

$$K = \frac{\kappa_n Rc/c_1}{\tanh(\kappa_n Rc/c_1)} \tag{46}$$

$$c_1 = (1 - (\frac{f}{\omega_T})^2)^{\frac{1}{2}}$$

These values are representative of the MBAY conditions at the shelf break with **d≈20m** and **h≈100m**, and where **N_0** was estimated based on the temperature maps shown in Figure III-B.1 as **$2.9 \times 10^{-3} s^{-1}$**, corresponding to a $0.25^\circ C$ temperature drop over a 50m depth, and the temperature difference across the thermocline interface is estimated to be $3^\circ C$. For these values:

$$R > \frac{1}{(1 + \frac{\pi}{2}\sqrt{S})} = 0.097 \tag{47}$$

implying that for the MBAY conditions only the lower mode will be significant at the interface depth (Baines, 1982). Therefore, an interfacial mode can be expected, decoupling the upper layer from the internal wave propagation in the stratified continuum below. This result allows the two layers to be treated separately which is consistent with the observations discussed in III-B. The observations showed different responses in the layer above the main thermocline compared to the layer below, although both were apparently tidally forced.

For the case of the interfacial mode, the above wave equation can be integrated across the density interface to obtain:

$$\Psi(x, -d) \approx -\frac{Qd}{h} + \phi_A \tag{48}$$

and

$$\Phi_A = \begin{array}{ll} \Phi_A(x, -d)\left(-\dfrac{z}{d}\right) & -d < z < 0 \\[2em] \Phi_A(x, -d)\left(\dfrac{h + z}{h - d}\right) & -h < z < -d \end{array} \tag{49}$$

where

$$\Phi = R + D_0 e^{-i\frac{X}{(1-R)^{\frac{1}{2}}}} \qquad X > 0 \qquad \text{(50)}$$

$$\Phi_{rr} + (1 - \frac{2\mu_0}{r})\Phi = -\frac{2\mu_0}{r} \qquad X < 0$$

where D_0 is obtained by the boundary ⌐ions (X=0) at the shelf break and

$$L = \sqrt{\frac{g'd}{\omega_T^2 - f^2}} \approx 3000m$$

$$X = \frac{x}{L} ; \qquad\qquad \Phi = \frac{\phi_A}{Q} \qquad \text{(51)}$$

$$T = \frac{h_L}{L\alpha} ; \qquad\qquad X_0 = T(1 - R) ;$$

$$\mu_0 = -\frac{1}{2}TR ; \qquad\qquad r = X_0 + X$$

and g' represents the reduced gravity, h_L is the depth at the shelf break (100m for Monterey Bay), α is the bottom slope (0.18 for the simplified 2-D geometry being used) and $2\pi L$ is the wavelength of the interfacial mode (app. 18000m for the MBAY case). Typical solutions for the equation at X < 0 (i.e., over the slope) can be found in terms of expansions of the Coulomb wave functions (Abramowitz, Stegun, 1968).

In order to estimate solutions over a steep slope, a step geometry is considered using typical MBAY parameter values as shown in Table III-A.1 and corrections for the slope case

determined. Therefore, for the step geometry case, the following results are obtained:

$$\Phi = R + D_0 e^{-iX(1-R)^{-\frac{1}{2}}} \qquad X > 0$$
$$R_R + D_1 e^{iX(1-R_R)^{-\frac{1}{2}}} \qquad X < 0 \qquad \text{(52)}$$

where $R_R = d/h_\infty$. From the boundary conditions we obtain:

$$D_0 = -\frac{R - R_R}{1 + (\frac{1 - R_R}{1 - R})^{\frac{1}{2}}} \quad ; \quad D_1 = -(\frac{1 - R_R}{1 - R})^{\frac{1}{2}} D_0 \qquad \text{(53)}$$

For the MBAY conditions $D_0 = 0.085$ and $D_1 = 0.095$; however, Baines (1982) shows that corrections for a linear continental slope, changes these constants to be $D_0 = 0.068 e^{-i0.2\pi}$ and $D_1 = 0.076 e^{-ip}$, where 'p' is a phase factor in the Coulomb wave functions and is determined by depth, slope and 'T'. Furthermore, using expressions (7.4) from Baines (1982) the current magnitude over the shelf is estimated to be 0.17m/s and 0.04m/s in the upper and lower layers respectively, with an interfacial displacement amplitude of 8.9m. These values will not change significantly over the continental slope since T is small, resulting in 0.19m/s and 0.004m/s for the slope current magnitudes in the upper and lower layer respectively and interface displacements of 8.9m (similar to the shelf values).

64

However, the phase lag is not easily determined because of the phase variation of the Coulomb functions with R, T and alongslope distance. As a result, for the MBAY case summarized in Table IV-A.1, a maximum velocity gradient of 0.20m/s can be expected across the thermocline due to the interfacial mode, resulting in a Richardson number of about 1.4 for a 10m width thermocline, i.e., small but above the critical value of 0.25. Therefore, the thermocline oscillations with ~10m amplitudes, wavelengths larger than 10000m, and tidal periodicity which were observed during the first part of the survey and discussed in Chapter III-B, are predicted using this theory. Furthermore, the wavelength of this interfacial mode will be of the order of 18000m, with an e-folding distance of 35 Km; consequently this mode will have significant amplitudes at considerable distances from the shelf break. This theory partly explains the different observed velocity fields in the layers above and below the thermocline until hour 152, discussed in Chapter III-B. However, the velocity fields in both the upper and lower layers displayed in Figures III-B.4/5 at 11m and 50m depths do not show a clear tidal signature, implying that other baroclinic phenomena are also present.

From the results of Baines (1973), the internal wave amplitudes in the stratified continuum below will be small unless:

$$p = \frac{1 - \alpha/c}{1 + \alpha/c} < \frac{h_L}{h\infty} \tag{54}$$

This inequality is observed in the MBAY case so significant amplitude internal waves can be expected to be generated below the thermocline. In fact, using expression (7.9) from Baines, (1982), internal wave amplitudes can be estimated by:

$$A \approx - \frac{Q}{h - d}(1 - D_1) - \frac{1}{4}\frac{Q}{h_L - d}(1 - D_1)\sqrt{\frac{c}{(\frac{\omega_T^2 - f^2}{N^2 - \omega_T^2})^{\frac{1}{2}}}} \tag{55}$$
$$\times [V(\frac{\xi}{2\gamma}) - V(-\frac{\eta}{2\gamma})]$$

where $V(\xi)$ is the function developed in Baines (1982) characterizing the wave amplitudes across the internal wave beam generated at the shelf break. The variables ξ, η and γ are determined by expressions (7.10) from Baines (1982) representing the normalized distance across the beam, distance along the beam, and wavelength scale respectively. Therefore, assuming a uniform stratification below the thermocline with $N \approx 2.9 \times 10^{-3}s^{-1}$ for a typical characteristic inside the beam, $V(\xi/2\gamma) - V(-\eta/2\gamma) \approx -2$, results in a baroclinic velocity amplitude $O(0.15m/s)$. Assuming D_1 with the same phase as the step geometry solution, these oscillations will lag the

barotropic tide by $\pi/2$, and will have a typical wavelength given by

$$\gamma = \int_{-d}^{h_L} \frac{1}{c} dz = 2000 \text{ m} \tag{56}$$

However, because the stratification is not uniform but concentrated in a shallow thermocline in the MBAY observations, the resulting forcing is dominated by a shallow layer below the thermocline at the shelf break.

B. INTERNAL WAVE PROPAGATION

This section summarizes the numerical procedure used to study the non-linear propagation of the internal waves generated at the shelf break interacting with the barotropic tide. For a better understanding and interpretation of the results, a single component wave solution will be propagated from a single point source at the shelf break, where the forcing is predicted to be a maximum. Therefore, the following results can be interpreted as an elemental response that might be integrated later with the solutions starting from other points within the water column, so that a more general solution to the problem can be obtained. The focus of this method will be to simulate the nonlinear interactions of internal waves induced by the barotropic tidal velocities, which are modified by topography along a 2-dimensional

67

continental slope. This approach will investigate the potential of these phenomena to generate the strong, baroclinic, jet-like pulses observed during the MBAY experiment and discussed in Chapter III-C.

Assuming a mean flow field varying slowly in time and space, within which a narrow bandwidth internal wave is propagating, the Boussinesq approximation to the equations of motion (Leblond, Mysak, 1978) can be written in the following form, neglecting wave-wave interaction terms (Kunze, 1985):

$$u_t + (\overline{V}.\nabla)u + (\overline{v}.\nabla)U - f.v = - p_x$$
$$v_t + (\overline{V}.\nabla)v + (\overline{v}.\nabla)V + f.u = - p_y$$
$$w_t + (\overline{V}.\nabla)w + (\overline{v}.\nabla)W = - p_z - b \qquad (57)$$
$$u_x + v_y + w_z = 0$$
$$b_t + (\overline{V}.\nabla)b + uB_x + vB_y - N^2w = 0$$

where the (u,v,w) represent the internal wave velocities and (U,V,W) the mean flow velocities. Terms $(V.\nabla)v$ correspond to the advection of the wave solutions by the underlying flow and are hereafter called 'advective' or 'Doppler shifting' terms. The terms $(v.\nabla)V$ correspond to the straining of solutions by the underlying flow and are hereafter called 'straining' terms. The mean flow and wave buoyancy are represented by 'B' and 'b' respectively, and 'p' is the wave induced pressure normalized by the mean density of the Boussinesq fluid. The mean flow is assumed to satisfy the following relations:

$$U_t - f.V = - P_x$$
$$V_t + f.U = - P_y$$
$$W_t = - P_z - B \tag{58}$$
$$U_x + V_y + W_z = 0$$

so that

$$B_x = - f.V_z + (U_z - W_x)_t$$
$$B_y = f.U_z + (V_z - W_y)_t \tag{59}$$

If we assume that an elemental internal wave variable can be written in the form of a plane wave

$$\Psi = \Psi_0(\overline{x}, t) e^{[-i(\omega - K\overline{x})]} \tag{60}$$

where the rate of change of amplitude is small compared to the phase variations, then the equations of motion can be written in terms of the wavenumbers K and of the intrinsic frequency following the mean motion $\omega_0 = \omega - K.V$, where ω is the Eulerian frequency and $K.V$ the doppler shifting:

$$
\begin{vmatrix}
-i\omega_0 + U_x & -f + U_y & U_z & i\,Kx & 0 \\
f + V_x & -i\omega_0 + V_y & V_z & i\,Ky & 0 \\
W_x & W_y & -i\omega_0 + W_z & i\,Kz & 1 \\
-fV_z + \zeta_t^y & -fU_z - \zeta_t^x & -N^2 & 0 & -i\omega_0 \\
i\,Kx & i\,Ky & i\,Kz & 0 & 0
\end{vmatrix}
\begin{vmatrix} u \\ v \\ w \\ p \\ b \end{vmatrix}
=
\begin{vmatrix} 0 \\ 0 \\ 0 \\ 0 \\ 0 \end{vmatrix}
$$

with, $\zeta^y = V_z - W_y$ and $\zeta^x = W_y - U_z$, and (Kx, Ky, Kz) represents the wavenumber components. To obtain non-trivial solutions, the determinant of this system must be zero. The roots of the resultant 3rd order polynomial with complex coefficients form an implicit dispersion relation which will be used to numerically trace the ray path (characteristic curve of the system) and predict the frequency and wavenumber of an elemental solution. For a 3-D case, no explicit polynomial was obtained and the roots were computed numerically from the implicit relation.

Typically, the roots of this characteristic polynomial represent three modes: one purely complex corresponding to the vortical mode; and the other two with the same imaginary part but having symmetric real parts representing the internal gravity modes (Lamb et al., 1992). However other solutions are possible depending on the wave group and phase speeds relative to the mean flow. For instance, for evanescent waves all the roots are imaginary (Lamb et al., 1992), and when the waves and mean motion are in opposite directions, non-symmetric roots with only negative real parts are possible, resulting in the waves being advected faster then their phase propagation as mentioned by Peregrine (1975) for surface gravity waves.

The solutions to this dispersion relation will then be used following an approach usually referred as the WKB approximation (Leblond and Mysak, 1978; Bretherton and Garret,

1968; Bretherton 1971; Bender and Orzag, 1978), which has been used by Peregrine (1975) to study surface gravity waves interacting with the mean flow. Baines (1982), as mentioned in the previous section, used an equivalent approach to study the propagation of internal tides in continuously stratified fluids; however, he did not consider the non-linear effects of the barotropic tide (doppler shifting and straining). Using the same linear approach, Baines and Fang (1985) compared the results of the model with a laboratory experiment, and concluded that non-linear effects should be important in a layered fluid at high (above unity) Froude number, $Fr=U/C_p$, where U represents the tidal speed at the shelf break and C_p the phase speed of the lowest mode. The MBAY data showed strong currents (unidirectional, baroclinic, alongslope pulses every 12-24 hours), a strong internal mixed layer below the thermocline, and stratification with a sharp thermocline at about 20m depth, suggesting that non-linear dynamics are relevant. Furthermore, from the buoy data of Pillsbury (1992), barotropic tidal velocities are estimated to be below 0.10m/s. Based on the results of the previous section, the phase speed of the interfacial mode is estimated to be about 0.40m/s, resulting in a Froude number near the thermocline well above unity (~4), at least for some portion of the tidal cycles.

Willmott (1987) and Maze (1987) developed three and two layer nonlinear models respectively, taking into account

advection by the barotropic tides. They showed that velocities of the resultant internal wave field can be several times higher than the barotropic tide, and that the resultant baroclinic residual flows change in space with the same length scales as the internal waves as a result of the "bunching" effect that sometimes can halt the internal wave propagation. However, they did not take into account rotation and straining effects by the tidal flow. Furthermore, they used two and three layered models, as approximations to the physical system, which do not necessarily well represent the baroclinic propagation of the internal tides.

Based on the linear modal model by Prinsenberg and Rattray (1975), the internal waves should propagate as beam-like structures away from the shelf break. New (1988) found tidal currents along these beam-like current structures (as described also by Baines, 1982) with velocities O(0.50m/s) in excess of the surface tides in the Biscay Bay. He also showed that the strong shear created by the internal tides was likely to generate strong mixing layers. Kunze (1985) used a ray tracing (WKB) method to study near-inertial internal waves propagating in geostrophic shear, and showed the importance of including the straining terms in the nonlinear equations of motion. He also showed that the WKB method was still approximately valid even when the spatial scales of the mean flow were comparable to the wavelengths of the internal waves.

The present development extends Kunze's work by considering the time variability in the underlying mean flow.

The ray equations for wave propagation in a moving media, using indicial notation, (Leblond and Mysak, 1978) are:

$$\frac{d\,x_i}{d\,t} = \frac{\partial \omega_0}{\partial K_i} + U_j$$

$$\frac{d\,K_i}{d\,t} = -\frac{\partial \omega_0}{\partial \lambda}\frac{\partial \lambda}{\partial x_i} - K_j\frac{\partial U_j}{\partial x_i}$$

$$i = 1,\,2,\,3 \qquad (61)$$
$$j = 1,\,2,\,3$$

where the total derivatives represent rates of change following the ray path and

$$\omega = \omega_0[\overline{K}(\overline{x},t);\lambda(\overline{x},t)] + \overline{K}.\overline{U} \qquad (62)$$

is the dispersion relation resulting from the equations of motion discussed above, with $\lambda(x,t)$ representing properties of the medium stratification and straining by mean flow. Frequency is not constant along characteristics due to the time variability of the mean flow, and an explicit form of the dispersion relation is required to compute the derivatives in the ray equations. In the present work, it was not possible to obtain an explicit relation for a 3-D case, so the implicit expression represented by the roots of the 3rd order polynomial described above are used to numerically compute the required derivatives. The largest real part of the roots was chosen as

73

the physical solution to the dispersion relation. When all the roots are imaginary or have negative real parts, the wave solution is assumed evanescent with all its energy absorbed in some way.

The wave amplitudes following characteristics starting at the shelf break and travelling along-slope can be estimated by considering the conservation of wave action 'A', defined as the ratio of the mean wave energy to the intrinsic frequency as follows (Bretherton, 1968; Garret, 1968; Bretherton, Garret, 1969; Peregrine, 1975; Leblond, Mysak 1978):

$$\frac{dA}{dt} = -\nabla \cdot C_g \, A \tag{63}$$

where 'C_g' is the group velocity defined as

$$C_g = \frac{\partial \omega_0}{\partial K_i} \tag{64}$$

The divergence of the group velocity is computed including the effects of spatial inhomogeneities of the mean flow and stratification, and the effects of spatial changes of the wavenumbers. In indicial notation this becomes:

$$\nabla \cdot C_g = \frac{\partial C_{gi}}{\partial K_i} \frac{dK_i}{dt} \frac{1}{C_{gi} + U_i} \Big|_{X=const.} + \frac{\partial C_{gi}}{\partial X_i} \Big|_{K=const.}, \qquad i = 1, 2 \tag{65}$$

74

The implementation of this approach is summarized next using the linear continental slope and simplified tidal flow described in the previous section, and assuming an internal wave solution at the shelf break as predicted in the previous section using the theory of Baines (1982). A plane wave is assumed as a typical solution to a first order approximation, allowing the characteristic paths to be estimated using a ray tracing method. A known initial solution is taken at the shelf break (x=0) where, based on the results of the last section, a single resonant Fourier component type of oscillation can be assumed to exist (Haberman, 1987; Leblond et al., 1978; Witham, 1974). This initial solution is idealized to have non-zero amplitude only at a single depth close to the thermocline (~30m depth) and over the shelf break (~zero width) and follows the shape of the forcing function displayed in Figure IV-A.1.c. Therefore, this analysis considers characteristics originating only from a single point in the water column, located at the shelf break and at 30m depth. However, because the initial solution and the environmental conditions change in time following the tidal cycle (which represents the non-stationary mean flow), the characteristics at each time in the tidal cycle need to be computed at that origin (Witham, 1974). The solution at the origin will propagate along the characteristic lines, so that each point along the line will have a time lag relative to the initial condition, and a wavenumber determined by the changes in the mean flow. The

wavelengths increase/decrease as the wave propagates into a faster/slower flow (Peregrine, 1975). The next step uses the wave action conservation (Peregrine, 1975 p.37) to compute velocity changes along these paths. These estimates, together with the time lag and initial phase, allow the computation of the instantaneous velocities of the solution at each point along the ray path. The velocity estimates correspond to the square root of half the wave action times the ray Eulerian frequency. The velocity solution changes in time, following the instantaneous Eulerian frequency estimates, which increase/decrease as the flow accelerates/decelerates (Peregrine, 1975). These changes in magnitude and frequency make the solutions nonlinear, inducing different residual flows along the characteristics.

It is assumed that reflections at the surface and bottom have no losses and that there is no dissipation by frictional effects. These assumptions could be easily changed in the future to simulate more realistic environments. Rays with the intrinsic frequency reaching zero or with the wavenumbers and wave-action increasing toward non-physical values are assumed to be dissipated by some type of instability, such as critical layer processes. Other areas where the rays are assumed to be dissipated are caustics i.e., rays converging toward a line or point in space with no possibility of reflection, where the WKB or the plane wave approximation is completely invalid (Peregrine, 1975). The ray equations and the wave action

balance are integrated using a 4th order Runge-Kutta scheme with an adaptative time step satisfying a specified threshold criteria. The time steps were all less than 1 hour, and close to surface or bottom reflections were a few seconds.

To verify the numerical procedure independently of the implicit limitations of the plane wave assumption that will be discussed below, a 2-dimensional formulation with explicit expressions for the dispersion relation is also used. The results for the steady-state mean flow developed by Kunze (1985) are also used for a qualitative comparison of the 3-D model runs. All the numerically computed terms in the ray equations are compared with the analytical 2-D counterparts for a typical ray. They showed small departures on the order of 10% and similar characteristics for the first 30 hours, except for the group velocity divergence which show larger differences. These differences are dominated by the introduction of the coriolis term in the dispersion relation. However, as the group velocity divergence requires the numerical computation of second derivatives, which amplifies numerical noise, it was decided to introduce a wave action maximum threshold value of 30 times greater than the initial value, after which characteristics exceeding this threshold were terminated (physically, the ray was dissipated). This limit threshold value was chosen based on the wave action

estimates for typical straight downward rays, which are in the range 0.1 to 1.5, times the initial wave action value.

To validate this type of approach for the case of propagation of near-inertial internal waves on topographically influenced tidal flow, several points must be considered. Usually the mean flow is assumed to be slowly changing and to have length scales much larger than the internal wave length scales, so that a formal expansion in terms of the following small parameters can be made (Bretherthon, 1968; Bretherthon, 1969; Peregrine, 1975):

$$\epsilon = \frac{MAX\left|\frac{1}{U}\frac{\partial U}{\partial x}\right|}{K} < 1$$

(66)

$$\beta = \frac{MAX\left|\frac{1}{U}\frac{\partial U}{\partial t}\right|}{\sigma_0} < 1$$

However, for the MBAY case $\beta \approx 1$ and $\epsilon \approx 1$ over the continental slope, suggesting that this approach is not valid, and higher order corrections are needed. One of the direct results from incorporating these higher order corrections is the possibility of adding the residual currents resulting from previous internal wave interactions into the underlying mean flow, as discussed by Bretherthon (1969) and Peregrine (1975). However, the results of Bender and Orzag (1978) showed surprisingly accurate results comparing the WKB approach with

78

analytical solutions for cases close to the WKB limit. Kunze (1985) also obtained accurate, physically well-based results, and successfully compared the effects of a critical layer computed numerically by a different method with the WKB approximation, demonstrating the presence of a caustic.

The present formulation allows time variability for the mean flow, so that additional factors and limitations should be considered. Bretherthon and Garret (1969) suggested that terms contributing to the dispersion relation must be slowly varying. For internal waves, they also suggested a relevant condition is that the ratio of the horizontal to the vertical length scales of the underlying flow should be much larger than the ratio of the internal wave horizontal to a vertical wavelength. Considering a barotropic underlying flow with horizontal length scales on the order of 200Km, typical of the MBAY site, this last condition is satisfied. These considerations motivated the current approach; however, as comparison of these model results with other numerical or theoretical solutions will not be possible, validation of this procedure is based on comparison with observational data and physical interpretations.

C. NUMERICAL RESULTS

This section presents the results of the implementation of the numerical procedure developed in the previous section for a linear continental slope, simplified barotropic tidal

flow, and assuming internal waves with amplitudes and wavelengths predicted above using the theory of Baines(1982) at the shelf break.

Discussion of the results of two different numerical model test runs follows. In run #1, the numerical model is forced with internal waves with a frequency six times the tidal frequency, horizontal wavelengths of 2Km (small compared to the topographical scale), and a reduced continental slope extending over 10Km (compared with the 5Km continental slope near Monterey Bay), and with depth changing linearly from 200 to 1000m. For this run the WKB approach is theoretically valid, allowing the numerical procedure to be validated by checking the consistency of the results. Run #2 more closely matches the simplified geometry for the MBAY site with a continental slope extending over 5Km and depth changing linearly from 200 to 1000m, but it is forced with internal waves with twice the tidal frequency having a horizontal wavelength of approximately 7Km. This is similar to the topographical scale and to the predicted wavelength for the internal tides, so the spatial conditions become nearly critical, although there is still a difference in time scales. The results of these two runs are compared by examining their ray paths and the distribution of energy along them. In each case, the families of characteristics are computed at different initial times throughout a single tidal cycle, considering both initially downward and upward wave packets.

The reference time in these runs (hour 0) corresponds to low tide.

The analysis of the model results compares these test runs with run #3, which considers the same geometry as run #2 but is forced with semidiurnal internal waves having 7Km length scales and amplitudes of 0.15m/s, as predicted using the theory of Baines (1982) in Chapter IV-A. Selected model velocity time series at points having the strongest residual flows are compared with time series velocity data from the MBAY experiment to assess the ability of this model to generate the observed residual flows. Finally, the number of occurrences of Richardson number below critical (<0.25) is evaluated during a 24 hour period and mapped to identify areas where mixing is likely to occur. The results are discussed and compared with the internal mixed layer observed during the MBAY experiment. All these model runs consider horizontally homogeneous stratification, with a sharp thermocline at 20m as summarized in Table IV-C.1.

For the conditions of run #1, linear theory predicts that downward rays should reflect from the slope approximately 1Km from the shelf break for a linear wave slope of approximately 0.03; however, as Figure IV-C.1 shows, the initially downward rays starting at hours 2 and 4 reach the floor closer to the shelf break at distances on the order of 500m. This is due to the onshore advection by the horizontal tidal flow against the horizontal ray propagation, and to an increased wave frequency

due to doppler shifting, which further reduces the internal wave slope 'c' as defined in Chapter IV-A. On the other hand, the straining by the tidal flow decreases the wave intrinsic frequency decreasing the wave momentum, resulting in the trapping of these rays close to the generation site. This can be seen in the initial amplitudes plot of Figure IV-C.2 comparing values to a 0.15m/s amplitude at the origin. The contribution of these characteristics is minimal and their energy can be assumed to be rapidly absorbed close to the shelf break.

The downward rays starting at hour 0 and 6 experience low tidal velocity at the source, so they hit the bottom at a distance comparable to that predicted from linear theory. However, as they propagate, they interact with offshore velocity fields allowing the ray starting at hour 6 to propagate further away. The intrinsic frequency of these rays is a maximum at the source, implying by wave action conservation that their momentum is also largest at the source. Therefore, their momentum will decrease as they propagate away from the shelf break. This effect appears to be stronger for the ray starting at hour 0, which is trapped near the surface at 3Km from the source.

The rays generated at hours 8 and 10 also show the effects of doppler shifting described above. The tidal flow is decelerating (from onshore to offshore), reducing the wave frequency and decreasing the ray slope, so they reach the

floor at a larger distance from the shelf break. The horizontal advection of the ray at hour 8 is stronger and directed offshore, so that the ray propagates further away. The rays starting at hours 0, 2 and 10, have accelerating mean flows at the origin causing them to break down before others that reach the bottom at the same distance from the source.

The upward rays experience the same effects described above for waves propagating in the opposite vertical direction; however, they also cross a layer of strong stratification which attenuates their vertical group velocity (C_g). Therefore, only rays at hours 8 and 10, starting with the stronger offshore tidal flow propagate significant distances from the shelf break. For the present case, the wave slope is larger than the bottom slope and the effect of the horizontal advection dominates the ray paths. The frequencies at the source seem to be important in the definition of the initial energy distribution and the distance each component propagates from the origin, so the rays with the smaller initial frequency propagate further offshore.

For the MBAY case (run #2), the ray paths displayed in Figure IV-C.3 show a behavior similar to run #1, although the paths extend further in the horizontal as would be expected for this lower frequency. Also, the increased slope introduces larger horizontal velocities, further increasing the range of the rays. The similarity between these two runs can be seen by

comparing the 9Km distance shown for this run with the first 2Km in run #1. However, one should note that more rays propagate to greater distances from the origin, and a small energy enhancement can be observed in the downward rays starting at hours 6-10 before they reach the bottom (as shown in the initial amplitude map displayed in Figure IV-C.4). Another important feature is that the upward rays, propagating towards a more weakly stratified layer, have smaller initial amplitudes which rapidly change in space. Some of the velocity/amplitude values close to the shelf break increase to unrealistic high energy levels. This suggests that the plane wave approximation might be violated for these cases, and that these solutions are unstable. These results can be considered as a consistent extension of the conditions for run #1.

For run #3, significant changes are observed in the ray paths (see Figure IV-C.5). These changes arise mainly from the tidal velocities overcoming the group velocities during part of the tidal cycle. This causes the rays to propagate backwards relative to their group velocity resulting in negative Eulerian frequencies; only the rays starting close to slack water at low tide have straight paths. This behavior suggests that nonlinear effects become dominant, leading to the question about the validity of the plane wave assumption. Another significant difference is that compared with the previous runs, the reduced vertical group velocities do not allow the initially upward propagating rays to leave the

upper, strongly stratified layers, causing them to become trapped near the surface. Therefore, independent of their validity, the upward rays are neglected in the rest of this discussion because of their negligible effects at depths where the MBAY observations showed strong nonlinearities.

The reliability of the ray paths for run #3 can be evaluated by analyzing the behavior of variables, such as frequency and wavenumber, and by evaluating how consistent they are with the known tidal flow and physics. Figure IV-C.6 displays the time series of wave frequency at the source. The changes in the Eulerian frequency are dominated by doppler shifting as expected; however, from the intrinsic frequency plot, it can be seen that the straining terms also introduce some variability, which superimposed with the doppler shift due to the advection by the underlying flow, attenuates the maximum Eulerian frequency and further decreases the frequency, breaking the symmetry of the doppler shifting. This effect changes the mean wave frequency at the source, but not significantly enough to change the output velocities. However, this effect is important in the generation of residual currents, together with the amplitude modulation determined by the wave action. In Figure IV-C.7, the time changes of intrinsic frequency along the rays can be seen. Rays starting during the flood increase their intrinsic frequency, while rays starting during the ebb show a decrease. This effect is similar to those discussed for runs #1 and #2 which caused ray

85

attenuation. In the Eulerian frequency plot, rays starting during the flood with negative frequencies can also be seen, indicating that they are traveling in the opposite direction to their group velocity. During this initial period, the rays are over the shelf where there are no spatial inhomogeneities in the velocity field, so the wavenumbers will not change. This can be seen in Figure IV-C.8, which displays the evolution of wavenumber components along each characteristic.

To compare the model output with the MBAY data, the velocity field at each instant is computed using the velocities along each characteristic. This is accomplished by computing the intrinsic frequency at each point, for each time, along the rays. Based on these values, an instantaneous velocity amplitude is estimated from the wave action value at that point. The individual velocities are then computed using this instantaneous amplitude and intrinsic frequency, and a phase lag determined by the time taken to arrive at that point, as shown in schematic of Figure IV-C.9. Also, based on the interfacial mode for a step slope as shown in Figure IV-C.10 (Baines, 1982), the initial phase at the shelf break of the internal waves propagating offshore is estimated to be leading the tidal forcing by $\pi/2$.

A 47 by 100 velocity grid is defined enclosing the continental slope between the shelf break and 9Km offshore, and from the surface to 1000m depth, in order to look at the resultant velocity field of a ray family. Velocity estimates

along each ray are projected on to the x-z plane at each instant. The velocity field between two consecutive projected characteristics is computed by linear interpolation along the z-dimension. The rays are computed every 15min through a tidal cycle to minimize aliasing effects, and to limit the linear interpolation needed between successive rays. However, at greater distances from the shelf break, the interpolation between diverging rays produces poor velocity estimates, resulting in broadening of some of the features.

To study the sensitivity of the resultant output flow field as a function of the number of rays, the density of upward rays was increased to start every 7.5min during the tidal cycle for run #2. No significant changes were found, indicating that the 15min ray spacing is appropriate for the grided domain.

A 24 hour run was performed to estimate residual flows for run #3. Figure IV-C.11.a/b show maps of the 24 hour averages of U and V velocity components. The existence of the velocity peaks in the range of 0.20m/s to 0.10m/s in the velocity field at 8250m distance between 30 and 70m demonstrate that nonlinear interactions of the internal tides with the tidal flow are able to produce significant residual flows. These depth ranges and magnitudes are comparable to the 0.20m/s, 70m depth baroclinic northward residual velocities observed during the MBAY experiment at the western portion of the surveyed area (see Chapter III). These residual flows are associated

with the upper portion of the internal wave beam, deepening further away from the shelf break and showing frequent reversals. It is not possible to verify all these features from the MBAY data, where the northward residual flows were observed only along one side of the surveyed box preventing the estimation of the current across-shore extent. However, a reversal in direction at the eastern portion was observed in the form of a narrow southward current with 500-1000m width as displayed in Figure III-A.4.(ii), centered at 1000m box side distance. This flow reversal is consistent with the model results that predict residual flow reversals over distances of approximately 500m in the cross-slope direction.

To assess the way in which these residuals occur, time series of the instantaneous profile velocity components were computed at three different locations at distances 6500m, 7500m, and 8750m along the slope as displayed in Figures IV-12.a/b/c. These locations were chosen to be representative of far, intermediate and close fields from the shelf break wave source. The profiles at 6500m shows wavelike oscillations with the U and V components close to quadrature. These oscillations change frequency with depth, such that a 24 hour periodicity can be observed in the V component at 70m depth, although the U component at the same depth has a 12 hour periodicity. At greater depth, higher frequencies are observed with a 6 hour period defined in the layers enclosed by the wave beam. This depth dependent frequency is consistent with the MBAY data,

which shows 24 hour periods in the V component in areas and depth ranges where current residuals occur; however, there is no evidence for these higher frequency waves in the data. This may be explained by the two hour sampling strategy used that might have aliased them, or smearing of these features by effects such as a broadband baroclinity tidal source and real variations in topography. The profiles at 7500 and 8750 do not show the low frequency component; however, they display a strong frequency modulation at the deeper portion of the beam with periods decreasing from semidiurnal to a few hours. Therefore, as in the MBAY observations, the diurnal oscillations of the modeled velocity field are spatially limited. Comparing the profiles at 7500m and 8750m, it can be observed that the higher frequencies become stronger near the source, indicating that this area will be more sensitive to model parameters values and to instabilities.

The profile time series show that in the far field, currents within the beam are nearly constant with depth, as Figure IV-C.12.a shows; however, strong vertical shear is observed in the upper layers, close to depths where the lower frequency oscillations are observed. On the other hand, the intermediate and near field velocities displayed in Figures IV-C.12.b/c become strongly sheared after 24 hours as strong vertical velocity changes are observed in the upper layers. To assess potential shear instabilities that might force mixing within the internal wave beam, a Richardson number criteria

was calculated using the hourly velocity fields over the slope and the stratification displayed in Table IV-C.1. The number of occurrences of critical or below critical conditions of $R_i < 0.25$ were counted as displayed in Figure IV-C.13. The high occurrence of critical conditions shows the potential of this mechanism to force shear instabilities similar to those observed during the MBAY experiment; however, this result should change significantly with geometry and barotropic tidal flow choices, so no direct correspondence would be expected between observations and this model result.

These model results, which reproduce features of the MBAY observations, show that nonlinear interactions of the internal wave field generated at the shelf break with the barotropic tide are candidate mechanisms for the rectification of internal tides. However, the modeled velocity field does not totally explain the spatial structure of the observed data, though they occur at similar depth ranges and with similar magnitudes. This could be due to the existence of enhanced internal waves activity associated with the canyon, and due to greatly simplified model geometry and barotropic tidal flow.

V. CONCLUSIONS

A process study over a coastal shelf break was developed to examine the role of tidal dynamics in mixing under conditions of steep topography and strong stratification. A 3 day survey (MBAY) of the upper ocean was conducted close to the mouth of Monterey canyon measuring velocity, temperature and salinity profiles along a 4km square box. Pycnocline displacements of 20m with wavelengths above 10000m were observed and discussed in Chapter III-B. Chapter IV-A showed that they result from an internal tide generation process, which also forced internal waves below the pycnocline. Strong, rectified bursts of shear kinetic energy were observed at depths from 50 to 100m with approximately 24 hour periods. The discussion in Chapter III-B showed that the measured weak winds cannot force either the observed highly inhomogeneous and strong current field and vertical shear, or the observed semidiurnal thermocline oscillations. Using the studies of the effects of geostrophic flow over a canyon by Klinck (1988, 1989) and the data of Koehler (1990), the cross-canyon geostrophic flow is expected to be much less energetic than the tidal flow. This is confirmed by the previous work in the area summarized in Breaker et al. (1989) and by the unpublished current meter buoy data kindly made available by C.H.Pilskaln, (Pillsbury, et al., 1992). Therefore, the

effects of geostrophic flow across the canyon on the generation of waves and residual flows cannot account for these observations. It was shown in Chapter IV-B that the observed bursts of energy could result from the rectification of the tidally forced internal waves undergoing interaction with the barotropic tidal flow. An internal mixed layer at the thermocline depth with 40m depth range was also observed and discussed in Chapter III-C. It was found that this mixed layer was probably forced by shear supplied by the non-linear internal waves below the thermocline, and by shear associated with the thermocline oscillations. However, the data and the theoretical analysis did not allow a positive identification of the triggering mechanism.

The MBAY data sets and the numerical results presented in chapter IV show the need for a complete analysis of the tidally forced dynamics of the Monterey Bay as suggested by Shea and Broenkow (1982). The good comparison of observed thermocline oscillation amplitude and frequency with the linear internal tide generation model by Baines (1982) showed continental slope tidal dynamics to be valid near the canyon mouth. Furthermore, velocity observations taken at the canyon mouth were compared with the numerical velocity fields resulting from a nonlinear internal wave propagation model, using model parameters typical of those in Monterey Bay, but considering a linear continental slope. The model results suggest the existence of multiple wave frequencies and

nonlinearities resulting in strong, unidirectional, spatially inhomogeneous currents, as observed during the MBAY experiment. However, there is no direct correspondence between observations and model results because of the simplified geometry and barotropic tidal model. It was also shown in the present work that internal tide dynamics in the area are largely dominated by nonlinear phenomena that might be enhanced by the actual steeper, more irregular topography and inhomogeneous stratification which are found inside Monterey canyon. The current approach can be extended to incorporate these cases; however, better internal wave dissipation models and higher order corrections should be developed and studied to increase the confidence of the numerical results. A more detailed discussion of these conclusions follows.

A. INTERNAL TIDES AT THE MOUTH OF THE MONTEREY CANYON

Based on the work by Baines, (1983), it can be assumed that internal tide dynamics at the canyon mouth are similar to those over the open shelf, as discussed in Chapter III-D.1. The effects of geostrophic flow over canyons has been studied by Klinck (1988;1989), and based on these papers and the current mooring data, the effects of geostrophic flow (i.e., eddies from the California Current) over the canyon can be neglected for the MBAY case.

It was shown in Chapter IV-A that the estimated barotropic tidal velocity field for a strong thermocline, as observed

during MBAY, will produce a maximum internal tide forcing close to the thermocline at the shelf break. Furthermore, using the generation model by Baines (1982), it was found in Chapter IV-A that there will be an interfacial mode of O(10m) amplitude and O(20Km) wavelength at the thermocline. This mode decouples the upper layer from the internal wave propagation in the stratified continuum below, and forces shear at thermocline depth that produces Richardson numbers close to 1 during parts of the tidal cycle. These results are in agreement with the measurements discussed in III-B, before hour 152 in the West portion of the surveyed area where semidiurnal thermocline oscillations with 10m amplitudes and wavelengths above 10Km where observed. Along the east leg, close to the canyon southern wall, the observations did not show the same tidal dependence. This suggests that other effects at the canyon wall are acting, possibly by canceling internal tide mechanisms or by creating a shadow zone. These mechanisms might be related to barotropic velocities across the canyon (alongslope). Unfortunately, the observations and the theoretical formulation do not offer any conclusions about this case.

B. BAROCLINIC RECTIFICATION OF TIDES

Barotropic tidal rectifications over the continental slope close to Monterey can occur by the generation of residual vorticity due to the conservation of potential vorticity

(dominated by vortex stretching), as discussed in Chapter III-D.2. Estimates for residual vorticity (Robinson, 1982) in the present case are of the order $3.6 \times 10^{-4} s^{-1}$, resulting in northward alongslope barotropic velocities of about $0.05 ms^{-1}$, close to the shelf break. These estimates compare well with the observations as mentioned in Chapter III-D.2. However, the MBAY data shows that the vertical mean values are a result of vertically layered residuals of jet-like current pulses which occur at 24 hours intervals. The non-linear modal approach for a stratified ocean (following Mass and Zimmermann, 1989a,b) showed that, although there is much in common with the homogeneous case, the main effect of including vertical stratification in tidal rectification by vortex stretching is a bottom intensification, which cannot be detected in the near-surface MBAY observations and is not consistent with the current maxima observed within the water column. Nonlinear layer models for the MBAY case can predict residual currents in the upper layer of about $0.02 ms^{-1}$ and $0.002 ms^{-1}$ in the lower layer, values that are too small compared with the observations. However, based on Baines (1982), the velocity amplitudes of the internal waves forced over the shelf break were estimated to be of about $0.15 ms^{-1}$, resulting in estimated residuals up to $0.05 ms^{-1}$. Again, this value is smaller than the observed layered time residuals which are approximately $0.25 ms^{-1}$. To evaluate the nonlinear processes that could lead to

these rectified velocities, a ray tracing model was developed by considering the effects of advection and straining of the internal wave field by the barotropic topographically enhanced tidal flow. The results of this model showed, for a simplified continental slope similar to that in Monterey Bay, 24 hour velocity residuals between 0.20ms^{-1} to 0.10ms^{-1}, at 40m to 70m depths along the upper portion of an internal wave beam starting at thermocline depth (~25m) at the shelf break. These rectified velocities start at distances as close as 1Km from the shelf break, and can be observed as far as 4Km from the source, showing sign reversals within distances as short as 500m. These residuals have the same order of magnitude as the MBAY observed values of 0.25ms^{-1}, and the depth ranges are comparable. However, for the MBAY data a determination of the across-shore extent of the observed strong northward velocity residues is not possible, though Figure III-A.4.(ii) shows a well defined residual velocity of 0.15ms^{-1} in the opposite direction, extending over a cross-shore distance of 500-1000m in agreement with the model results. However, the depth ranges over which the residuals are observed are broader than the model results. This is probably due to many effects, such as the existence of pressure gradients established in the canyon, which can enhance the internal wave field (Baines, 1983; Huthnance, 1989), and due to the simplified tidal flow and topography which were used in the model.

The temporal variability of the model currents along the wave beam show a multiplicity of frequencies with smaller values close to diurnal frequencies and at locations where the maximum current residuals were observed; on the other hand, higher frequencies were observed close to the source at the shelf break. This result partially agrees with the MBAY observations, which showed residual velocities resulting from diurnal jet-like features at depths between 50 to 100m, while semidiurnal frequencies were observed at other depths. However, the MBAY observations showed the low frequency fluctuations as deep as 150m throughout the layers where the residuals were observed. Again, this discrepancy between the model and observations is likely due to the existence of the canyon and due to the simplified topography and stratification used in the model. The MBAY data did not resolve higher frequency oscillations due to the sampling strategy. Therefore it is not possible to make a complete comparison with the model results.

Based on this discussion, nonlinear interactions of the internal waves generated at the shelf break, together with the barotropic and topographically changed tidal flow, are a mechanism that can cause the occurrence of diurnal, strong, baroclinic, unidirectional jet like features, similar to those observed during the MBAY experiment. These nonlinear interactions can also contribute to current shear residuals with the current reversing within small vertical distances.

97

C. INTERNAL MIXING DUE TO THE TIDALLY FORCED SHEAR

The nonlinear internal tide model developed in Chapter IV, showed multiple frequencies and a strongly baroclinic current structure, occurring along a beam which starts at the shelf break. The modeled vertical current shear was observed to be stronger near the source, where higher frequencies exist, and at each location close to the upper limit of the wave beam, where the lower frequencies were observed. A Richardson number criteria was applied to the modeled internal tide field to estimate regions where mixing was likely to occur. The number of occurrences of Richardson number below the critical value of 0.25 were counted for a 24 hour model run. It was found that internal tide, wave-induced shear instability mechanism could account for the occurrence of local internal shear instabilities, which will dissipate wave energy and force internal mixing layers, similar to the observation during the MBAY experiment within the thermocline.

D. FUTURE WORK

Assumptions in the numerical model developed in Chapter IV are not completely satisfied for the case under consideration. The comparisons with the MBAY observations do not completely validate the numerical results. Therefore, it is desirable to complement this work by estimating the magnitudes of higher order corrections, and by comparing results with data other

than the MBAY survey or with other existing validated model results.

When comparing the numerical results with observations, significant discrepancies were found and attributed to simplified geometry and barotropic tidal flow. Therefore, one obvious extension of the present work is to improve the barotropic tide model and to use real topography, including the effect of the canyon, using an approach similar to the one developed by Baines (1983).

Other improvements of the numerical model can be achieved by including wave-wave interactions, better identification and handling of some wave-current interactions where the ray tracing method is clearly not valid, and by using a more realistic model of the surface and bottom reflections (currently they are assumed to be perfectly elastic).

99

APPENDIX A - TABLES

Table II-A.1

Geographycal coordinates of the surveyed square area during the MBAY experiment.

	LATITUDE	LONGITUDE
Corner # 1 (NE)	36.7366	122.0033
Corner # 2 (SE)	36.7022	122.0033
Corner # 3 (SW)	36.7022	122.0483
Corner # 4 (NW)	36.7366	122.0483
Center (P.Lobos)	36.72	122.025

TABLE IV-A.1

Summary of significant parameters of Baines (1982) model, showing numerical values estimated for MBAY conditions.

	DEFINITION	MBAY VALUES	COMMENTS
ω_T	$2.\pi/$Tidal Period	$1.4 \times 10^{-4} s^{-1}$	Tidal Frequency
N	$\dfrac{g}{\rho_0} \dfrac{\partial \rho}{\partial z}$	$2.9 \times 10^{-3} s^{-1}$ – Mean $4 \times 10^{-3} s^{-1}$ – Sfc $20 \times 10^{-3} s^{-1}$ – 20m $3 \times 10^{-3} s^{-1}$ – 100m $2 \times 10^{-3} s^{-1}$ – 1000m	Brunt-Vaisala Frequency
c	$c^2 = \dfrac{\omega_T^2 - f^2}{N^2 - \omega_T^2}$	0.03 – Sfc 0.006 – 20m 0.04 – 100m 0.06 – 1000m	Internal Wave Slope
R	d/h	0.2	Parameters determining the existence of an interfacial mode
S	$S = \dfrac{\dfrac{g\Delta\rho_0}{d\rho_0}}{(N_0^2 - \omega_T^2)}$	35	

	DEFINITION	MBAY VALUES	COMMENTS
K	$\dfrac{\kappa_n Rc/c_1}{\tanh(\kappa_n Rc/c_1)}$		Normal modes at constant depth
c_1	$(1 - (\frac{f}{\omega_T})^2)^{\frac{1}{2}}$	0.82	Gyroscopic Wave slope
L	$\sqrt{\dfrac{g'd}{\omega_T^2 - f^2}}$	3000m/2π	Internal Wavelength at Interface
α	$\Delta h/\Delta x$	900m/5000m	Idealized Bottom Slope

TABLE IV-C.1

Summary of model runs used to discuss the numerical procedure
and to estimate the flow associated with nonlinear effects on
internal waves propagating from the shelf break.

	RUN #1	RUN #2	RUN #3
Slope	Attenuatted	MBAY	MBAY
Hor. Scales	~2 Km	~7 Km	~7 Km
Period	~ 2 Hr	~ 6 Hr	12 Hr
Stratification	MBAY	MBAY	MBAY

Note: MBAY stratification corresponds to the following values of N:

Depth	N
0	4×10^{-3}
20	20×10^{-3}
30	2.9×10^{-3}
100	2.9×10^{-3}
1000	2×10^{-3}

APPENDIX B - FIGURES

Figure I-A.1

Physical processes assumed important in a coastal region with a highly irregular topography. The processes inside the thicker line apply to the Monterey Bay Mixing Experiment (MBAY), in September 1991.

Figure I-A.1

108

Figure II-A.1

Figure (a) shows a map of the Monterey Bay. The Monterey Bay Mixing Experiment (MBAY) location and the mooring site of the buoy data of C.H.Pilskaln (Pillsbury et al., 1992) are marked with arrows. Figure (b) shows a schematic of the MBAY experiment and a zoom of ocean floor topography. The RV "Pt. Sur" performed repeated profiling around a square path approximately every 2 hours during three days acquiring ADCP velocity profiles, 586 Tow-Yo CTD profiles and meteorological data. Concurrently, the RV "Pt. Lobos" was stationed close to the center of the box controlling a ROV performing direct turbulence measurements. The surveyed area covered a 4 Km square in the South-West wall of the Monterey canyon, whose coordinates are shown in Table III-A-1. This area has a highly irregular topography with depth ranging from 700m at the north-west corner to 1500m at the north and south legs. Velocity data were gathered down to 250m depth and ancillary data (temperature and salinity) were observed to 80m depth along the surveyed box. Strong shear and an internal mixed layer were observed at the western side of the box.
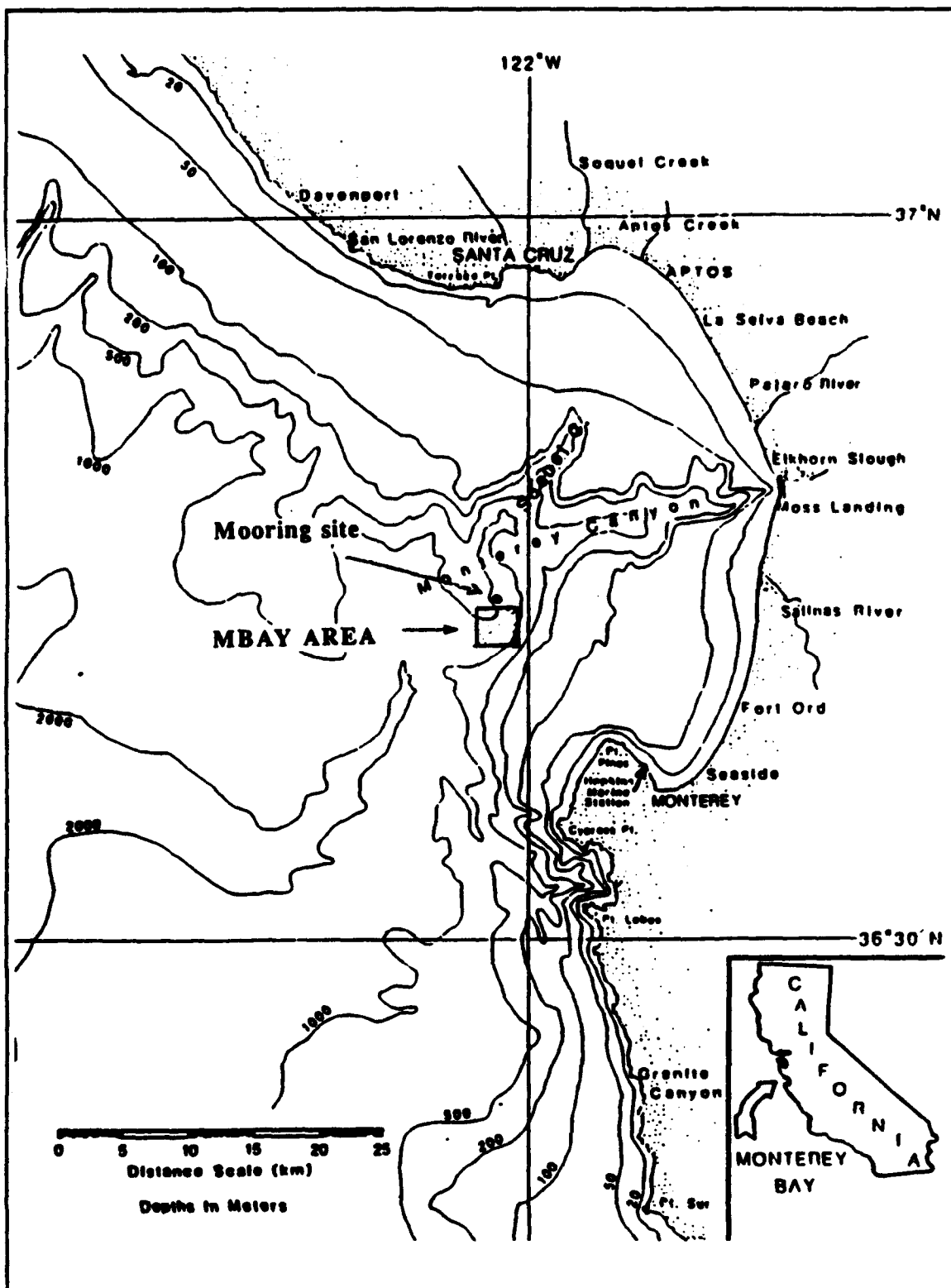
Figure II-A.1 (a)

**MBAY
MIXING EXPERIMENT**

Monterey Bay

Sept 1991

TOPOGRAPHY

[122°W]

N

W
[36°N]
[45°]

E
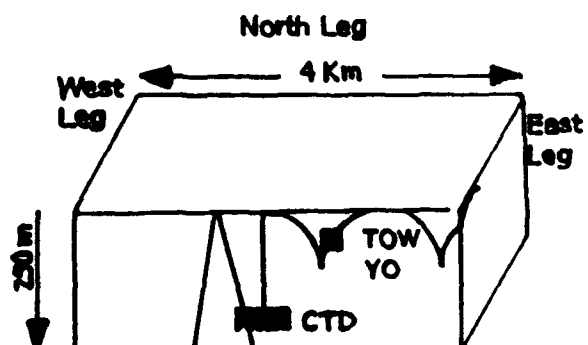
Figure II-A.1 (b)

Figure II-A.2

Along track time series of eastward (U) and northward (V) ADCP velocities from 7 to 120 meter depth for box #25. Each vertical profile has been demeaned relative to a reference layer at 100 meter. Profiles were gathered every 1 minute. The profiles corresponding to each box corner are marked along the x-axis. Strong baroclinic, jet like features are evident in both components. These jets appear to be decouple from the surface and to reach maximum values near the thermocline. The strong shear layers at approximately 20m and 50m depths between ADCP profiles 4050 and 4070 (better seen in the U component profiles), and are simultaneous with the isotherms displacements (upward at 20m and downward at 50m) shown in the along track temperature profiles (between Tow-Yo profiles 472 and 481) in Figure III-A.3.

CORNER

North East	South East	South West	North West	North East

ADCP PROFILE #   **U Component**

4055   4081   4110

V Component

Figure II-A.2

Figure II-A.3

Along track time series of (a) sigma-theta and temperature,
and (b) salinity, from 0 to 80 meter depth for box #25. The
profiles at each box corner are marked along the x-axis. The
deepening of isotherms appears to be related to the occurrence
of the strong shear shown in Figure III-A.2. There is some
evidence of temperature inversions that are being compensated
by salinity. Internal waves are evident at the thermocline in
the sigma-theta and temperature profiles.

CORNER

TOW-YO PROFILE #

Figure II-A.3 (a)

115

CORNER

North East	South East	South West	North West	North East

TOW-YO PROFILE #

473 483 494

Figure II-A.3 (b)

116
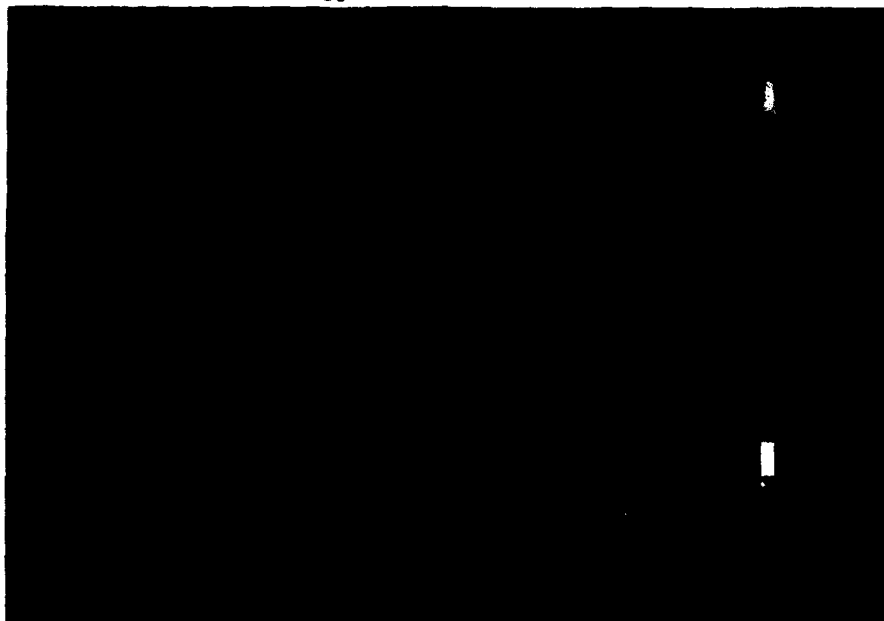
Figure II-A.4

T/S diagrams of the along track Tow-Yo data over the West most leg 12 hours apart: (a) corresponds to box #1 at 01:00 in 9/5/91; and (b) corresponds to box #5 at 12:00 of the same day. The new water type, appearing at the depth of 30 meter in (b) (box #5), corresponds to a loss in potential energy (denser water) and must be a result of mixing or intrusions.

Figure II-A.4 (a)

118

Figure II-A.4 (b)

119
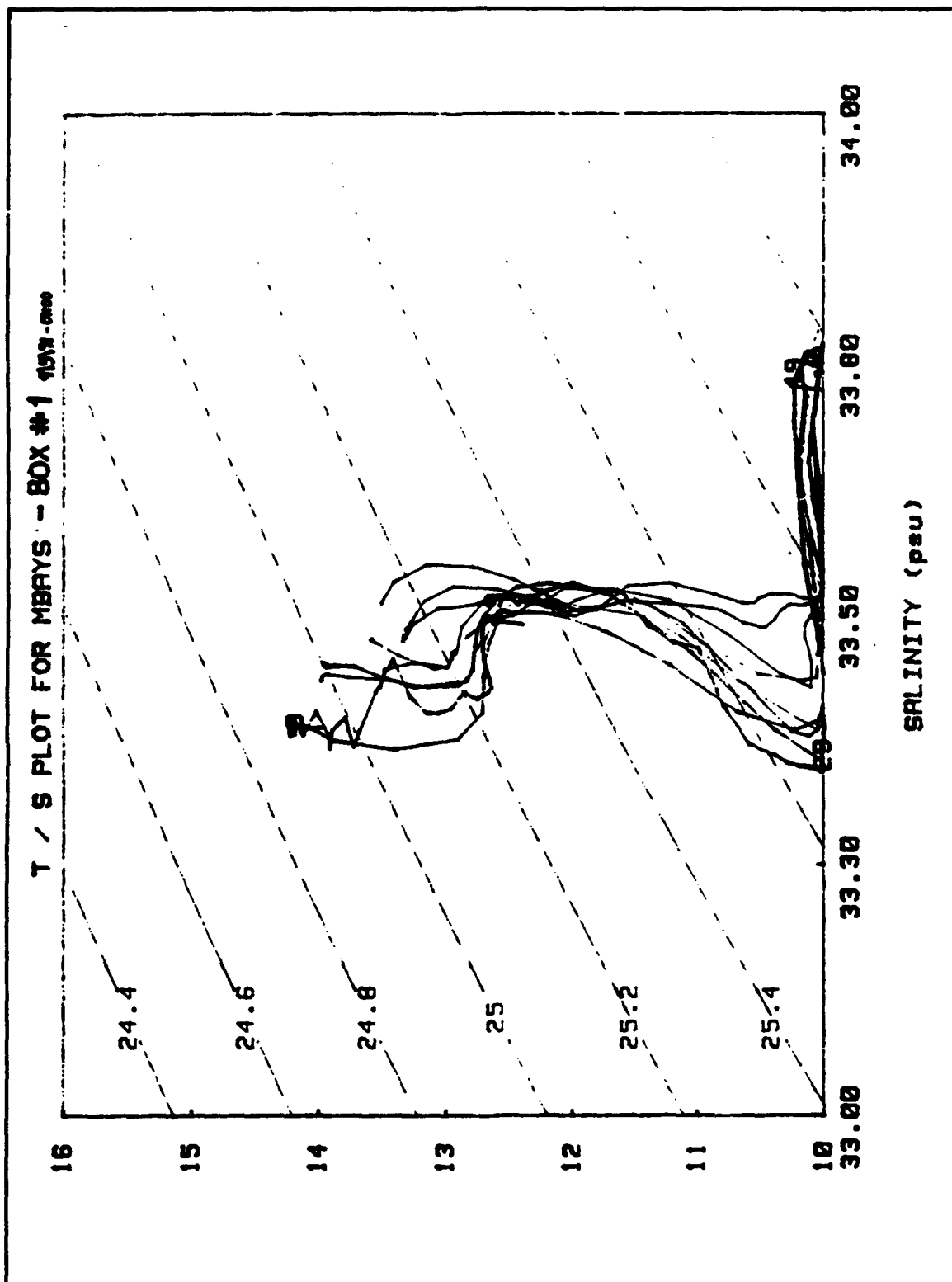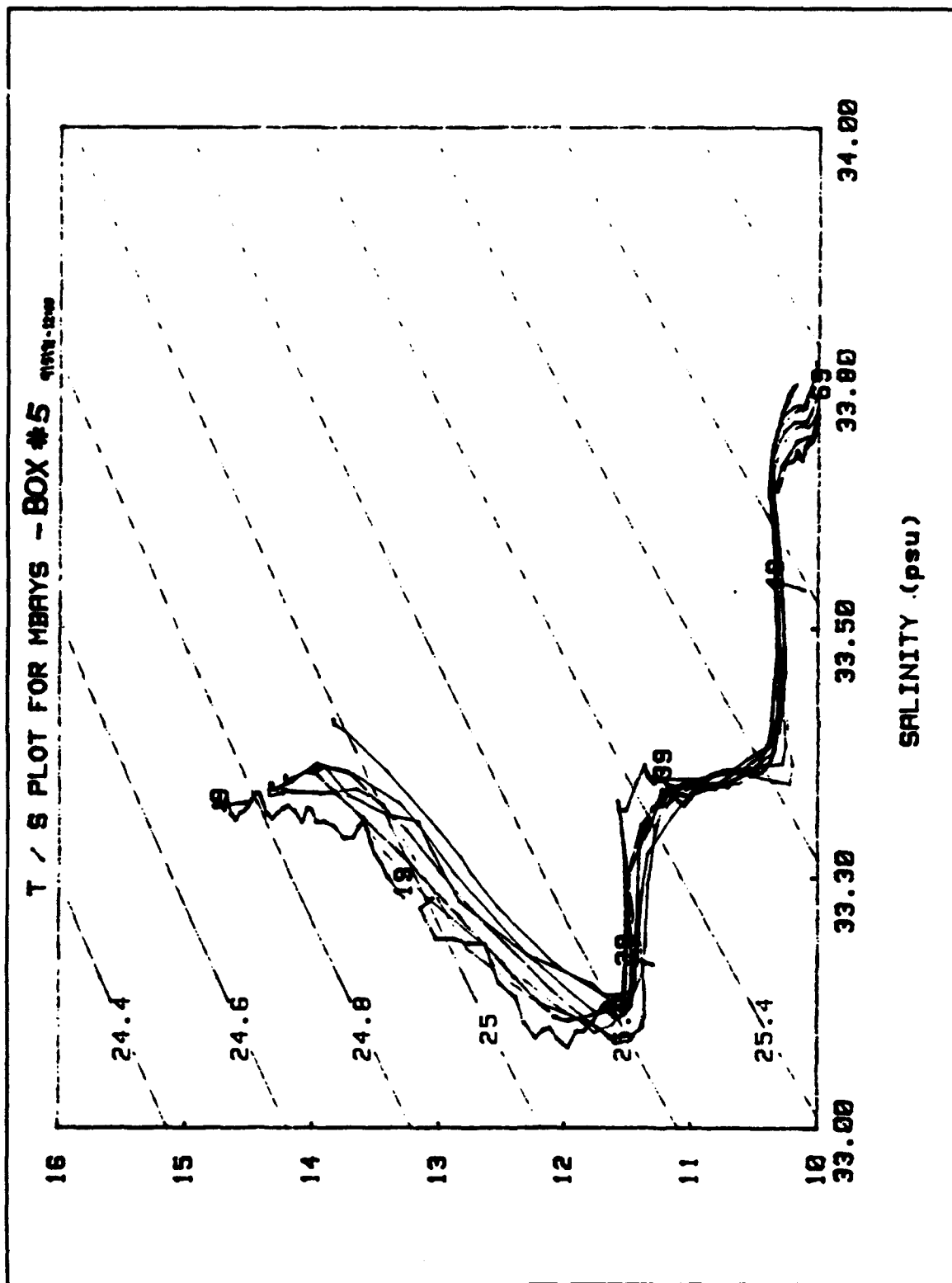
Figure II-B-1.1

Figure (i) shows the 2-dimensional autocorrelation function used for the assimilation of the MBAY data into a grid. Figure (ii) shows the correlation values at a zero distance lag as a function of the time lag. Similarly, Figure (iii) shows the correlation values at a zero time lag as a function of the spacial lag. Correlation length and time scales were chosen based on the sampling scale. The scaled variables 'tt' and 'rr' correspond to the squares of the scaled time and distance lags and are displayed in Figures (iv) and (v).
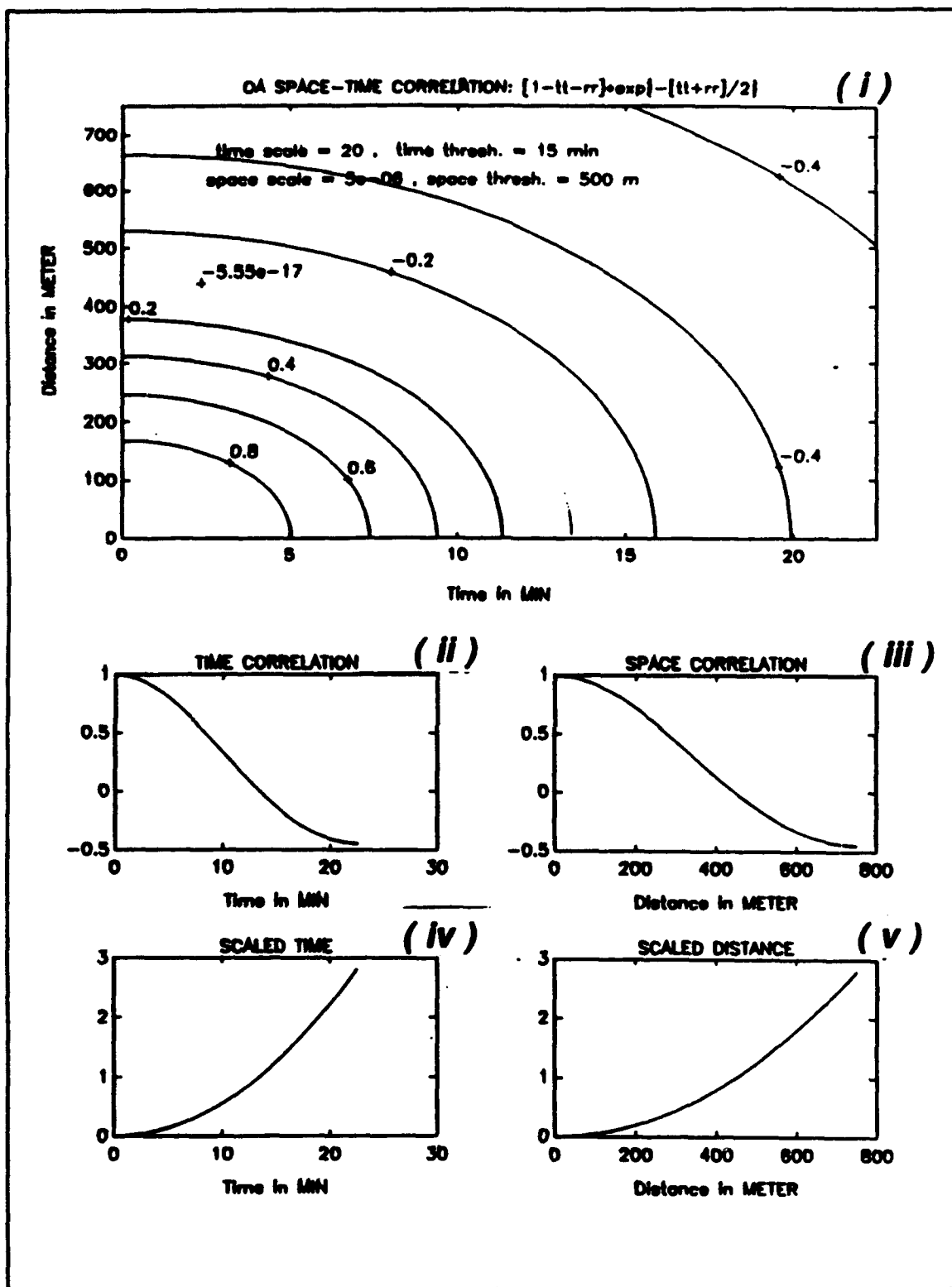
Figure II-B-1.1

Figure II-B-1.2

An example of the implementation of the optimum interpolation
scheme used to analyze the several observations onto a grid.
An empirical correlation function with 450 meter and 15
minutes scales was used. The upper Figure (i) shows the depth
averaged number of data points used for each of the 27 runs,
around the surveyed box. Less than 5 data points were used for
most of the grid points along the boxes. The lower Figure (ii)
shows contours of the depth averaged, normalized RMS errors,
at each grid point for each box. RMS errors are indicators of
the dominant distances between the data points and each grid
point. Gaps in the data were assigned RMS of 1.
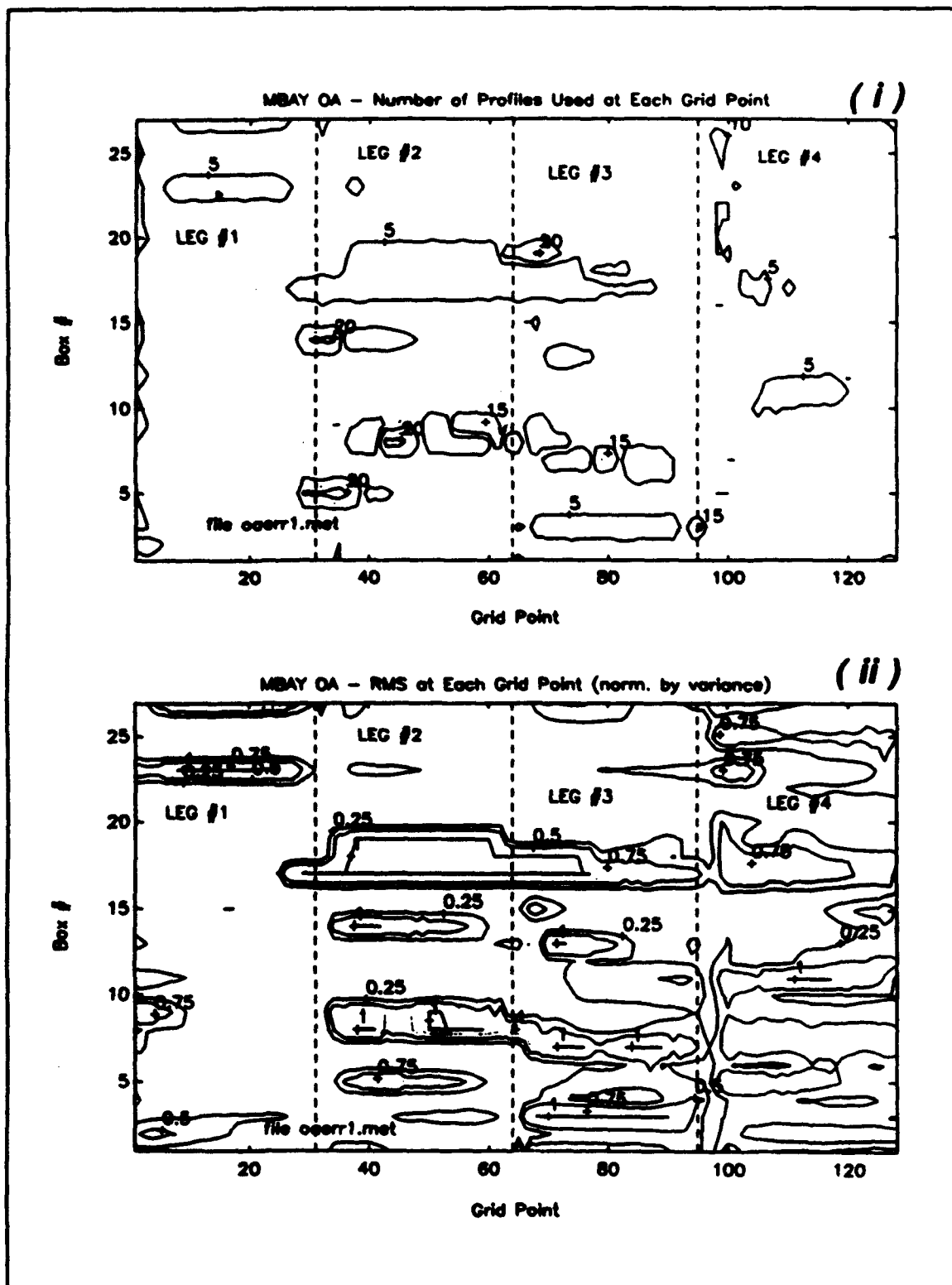
Figure II-B-1.2

Figure II-B-2.1

Absolute U (i) and V (ii) velocity component spectra (unfiltered data), after applying the GPS navigated ships velocity. Three bands are identified. The higher frequency band is assumed to be instrumental noise and was filtered from the data using a 4th order, zero-phase, Butterworth filter. Within the error band, the observed variance is assumed to be from instrumental noise and from physical current structure. This band was used to estimate the error of the absolute current estimates (app. 4 cm/s at 95% confidence). The variance in the structure band is assumed to dominated by physical current structure. The peak at approximately 2 hour period results from the strong inhomogeneities in the mean velocity field over the sampled area. The semi-diurnal tidal component is observed in both U and V spectra. The peaks at approximately 4 hour period have no obvious explanation. They might be due to doppler shifts of the tides or to inhomogeneous spatial current structure.
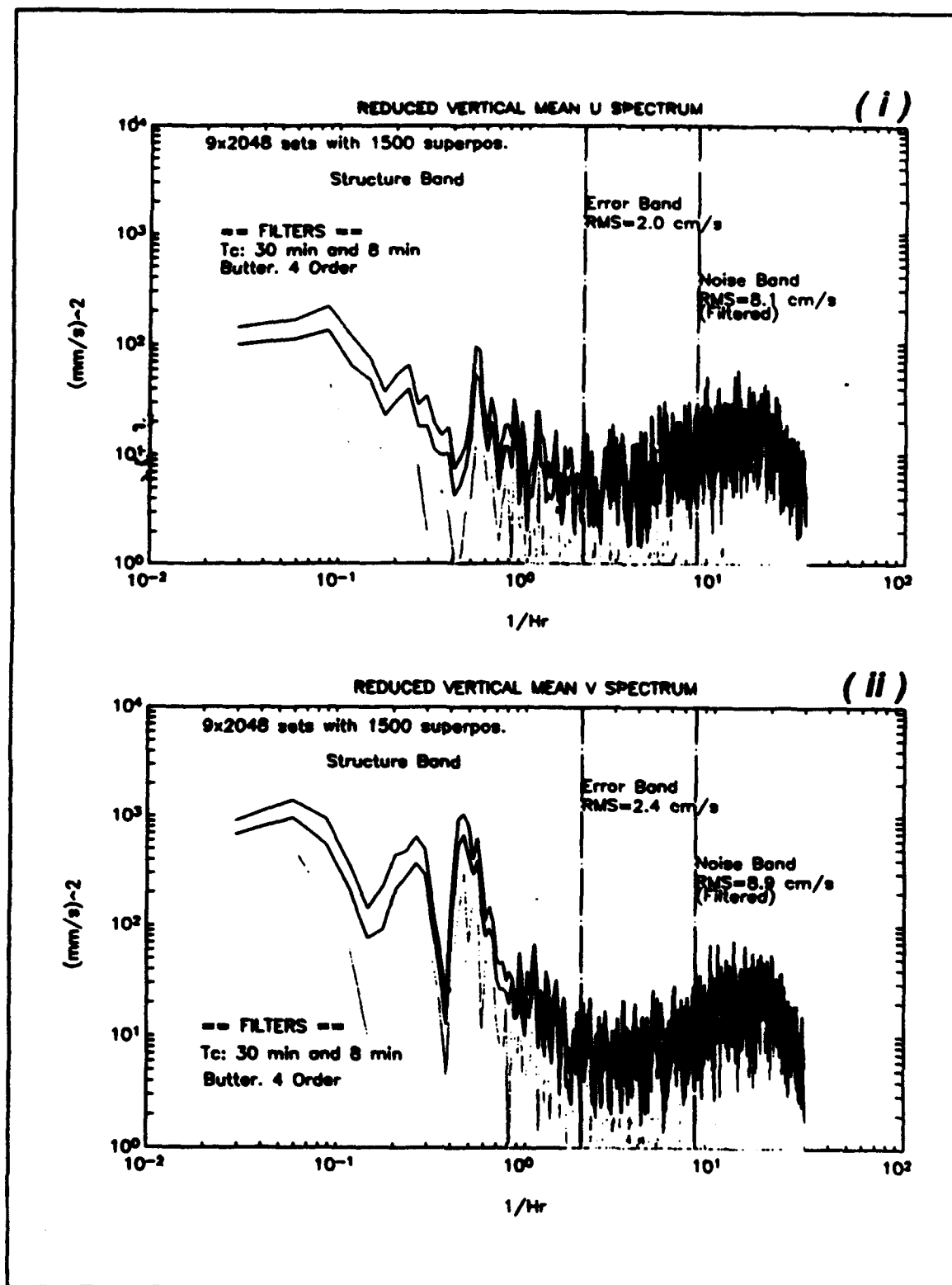
Figure II-B-2.1

Figure III-A.1

Vector plot of the time series of winds (i), during the MBAY experiment. The wind magnitudes were low to moderate with a rapid change in direction at hour 156. The magnitude and direction of the wind are displayed in (ii). Below the figure, the hours of the predicted high and low tides are marked along the x-axis.
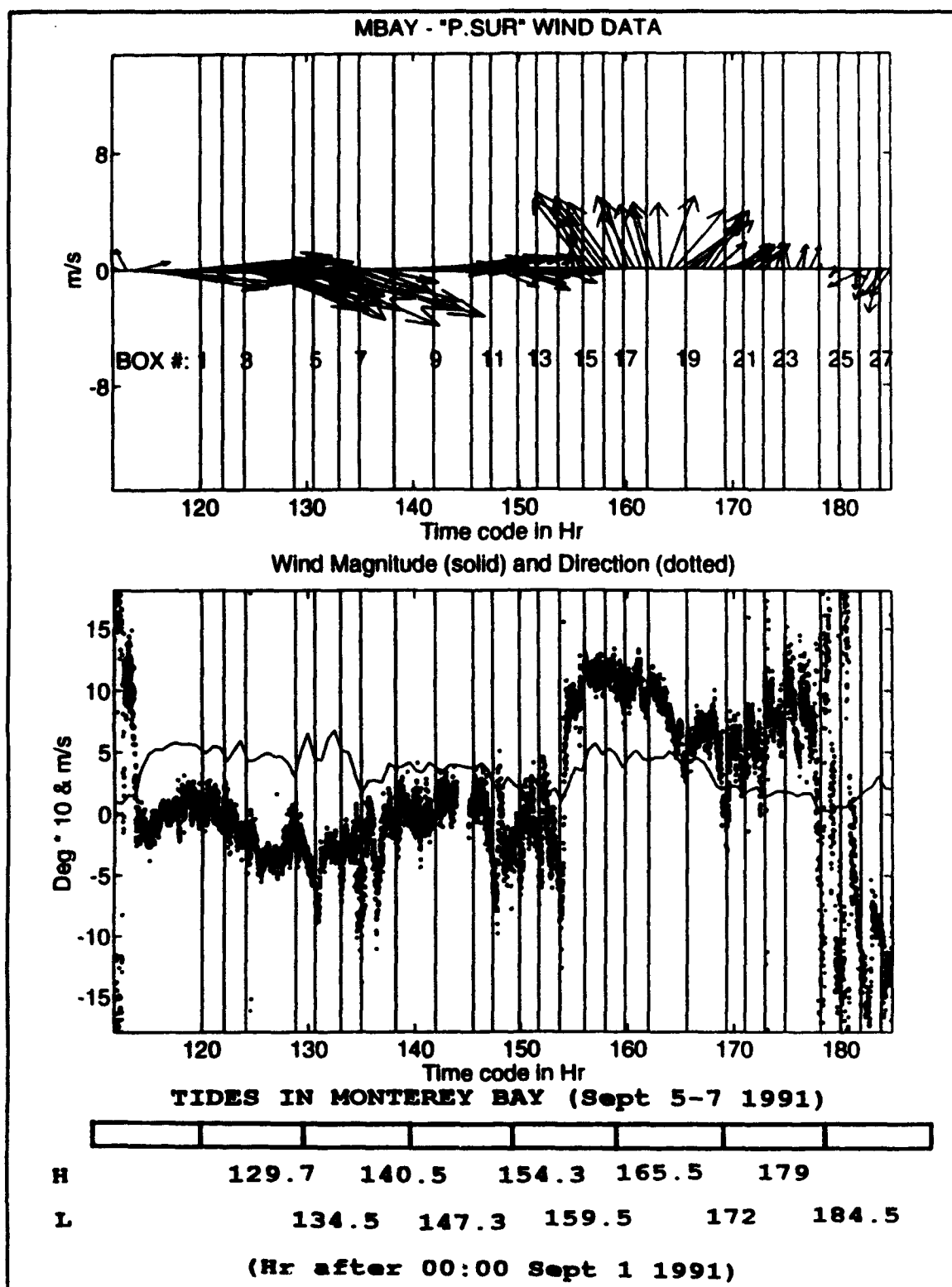
Figure III-A.1

Figure III-A.2

Vector plot of vertically averaged (upper 250m) absolute velocities averaged over all 27 box measurements. Stronger currents are observed at the west leg over the Southward facing slope of the canyon (Figure II-A.1). Overall, an anticyclonic circulation can be seen. Figure III-A.6 gives quantitative estimates of this circulation and of the divergence.
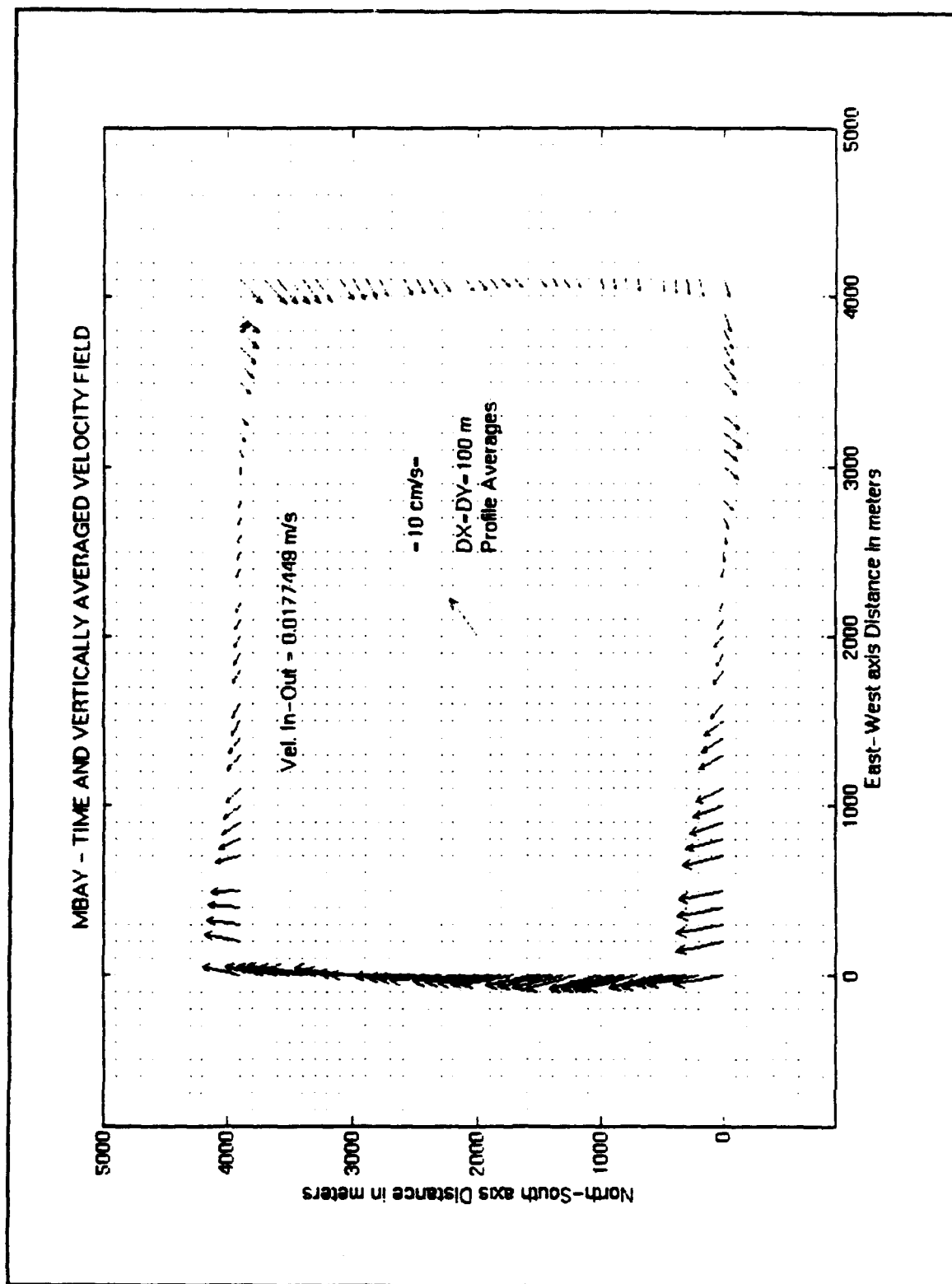
Figure III-A.2

Figure III-A.3

Profiles of time averaged eastward (U) velocity component for the 3 day measurements. Each panel represents the observed values along one leg. Figure (i) corresponds to the east most leg, (ii) corresponds to the south most leg, (iii) corresponds to the west most leg and finally (iv) represents the north most leg. Each panel starts at the beginning of the corresponding leg in the following direction (NE-SE-SW-NW-NE). They show a strong baroclinic and spatial inhomogeneous mean flow. See the text for other figure interpretations.

ADCP TIME AVERAGED U-VELOCITY CONTOURS (in cm/s)
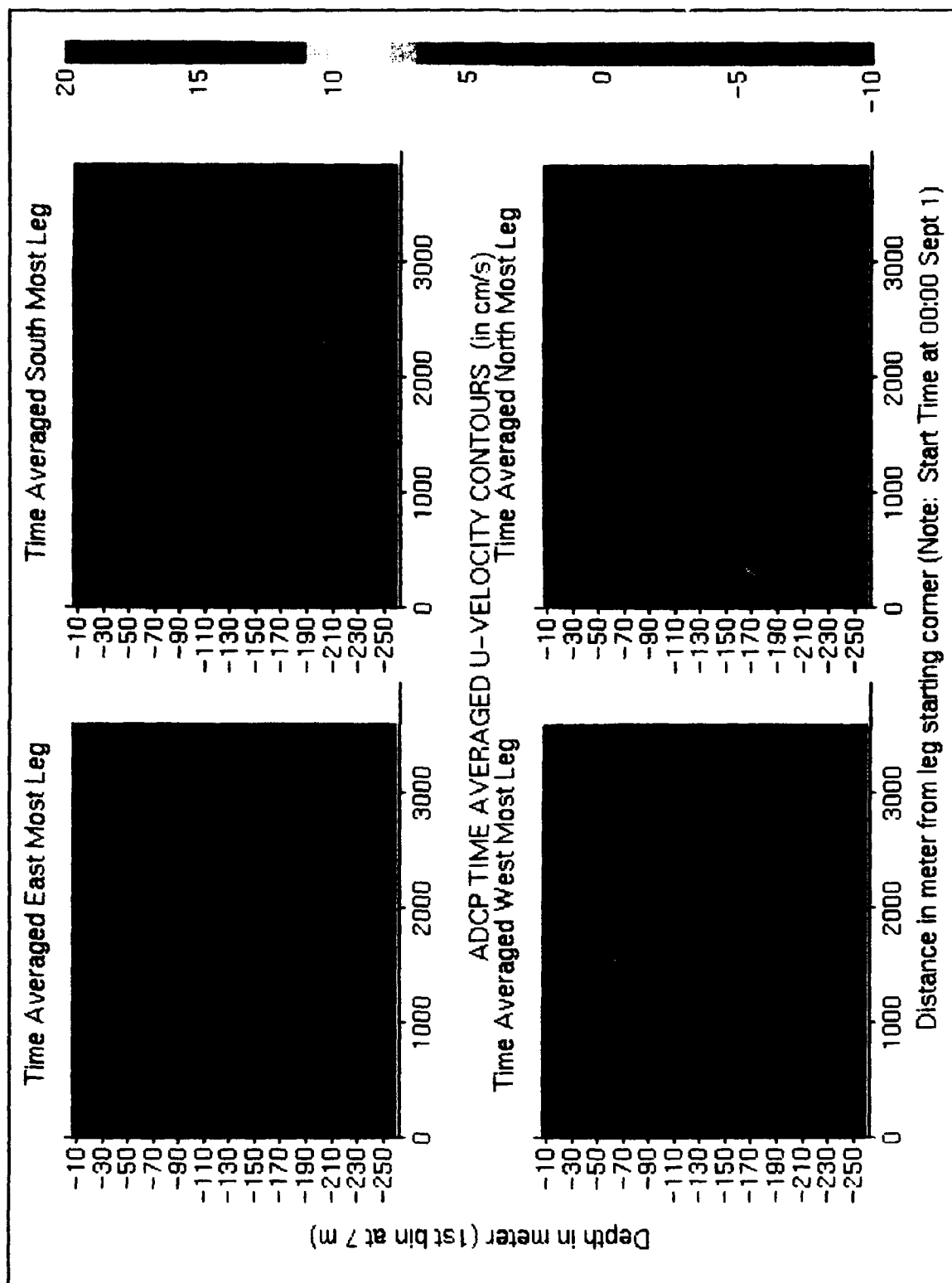
Figure III-A.3

Figure III-A.4

Profiles of time averaged, northward (V) velocity component for the 3 day measurements. Each panel represents the observed values along one leg. Figure (i) corresponds to the east most leg, (ii) corresponds to the south most leg, (iii) corresponds to the west most leg and (iv) represents the north most leg. Each panel starts at the beginning of the correspondent leg, in the following direction (NE-SE-SW-NW-NE). They show a strong, baroclinic and spatial inhomogeneous mean flow. See the text for other figure interpretations.

Figure III-A.4

133
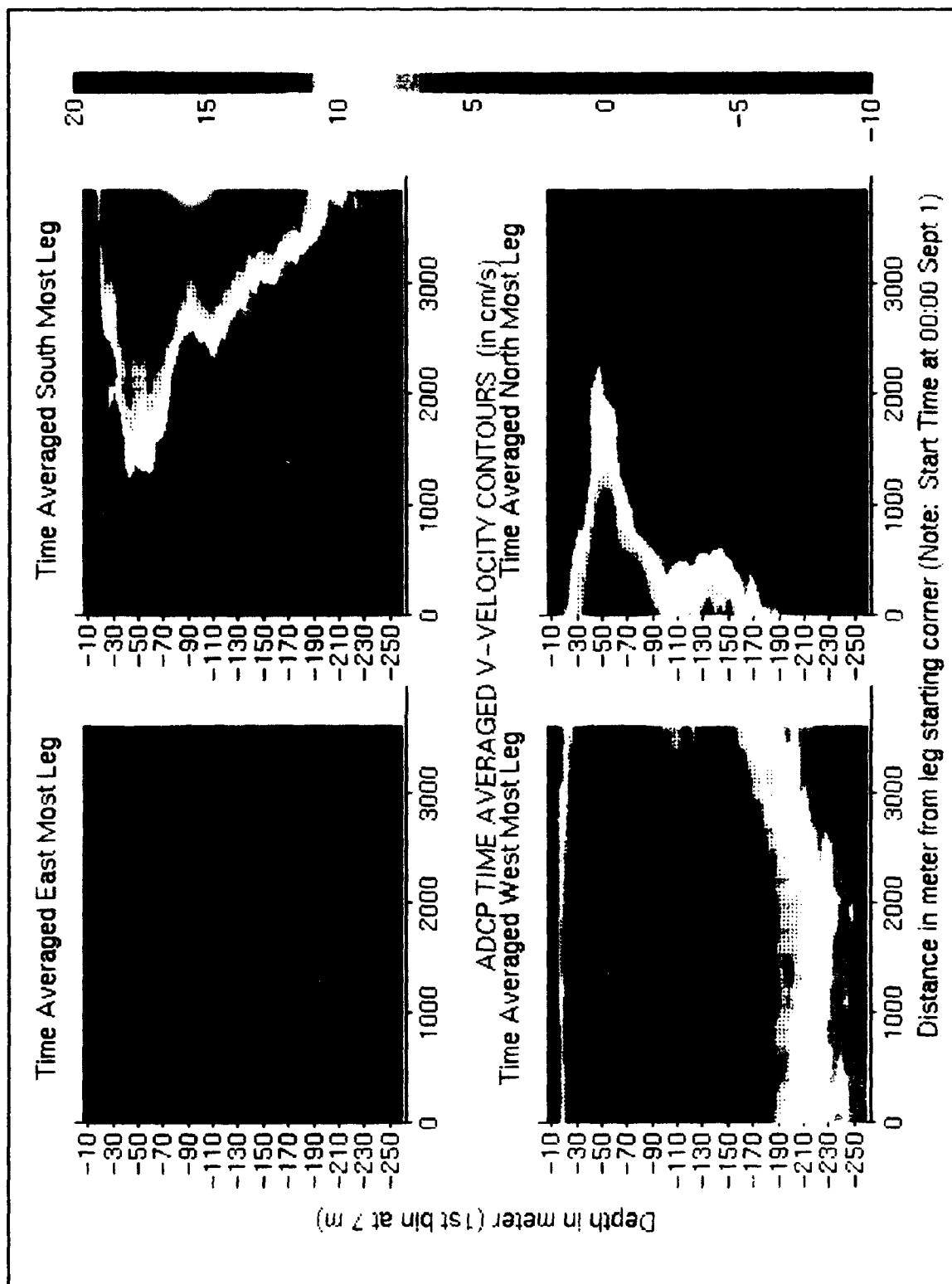
Figure III-A.5

Time series of box mean divergence times the inertial frequency (a), box mean vorticity (b) and time derivative of the box mean vorticity (c). The divergence was computed based on the normal component of the current relative to the ship's closed track and the vorticity based on the along-track velocity component. The tidal signature can be seen on the vertical averages of the divergence (suggesting either internal wave motion or topographically forced vertical velocities). A strong baroclinicity is evident in all current components. One should also note the strong, rapid vorticity change in the vertical at 30m depth at hour 152. Section III-C discusses likely consequences of this vorticity pattern. The time derivative of vorticity, though it shows the correct order of magnitude relative to the divergence that one can expect from linear theory for an homogeneous ocean, does not follow closely the divergence patterns. This is likely due to the presence of near-inertial internal waves. The tidal signature is also apparent in the vertical averages but is weaker than the divergence counterpart.

Figure III-A.5 (a)

135

Figure III-A.5 (b)

136

Figure III-A.5 (c)

137
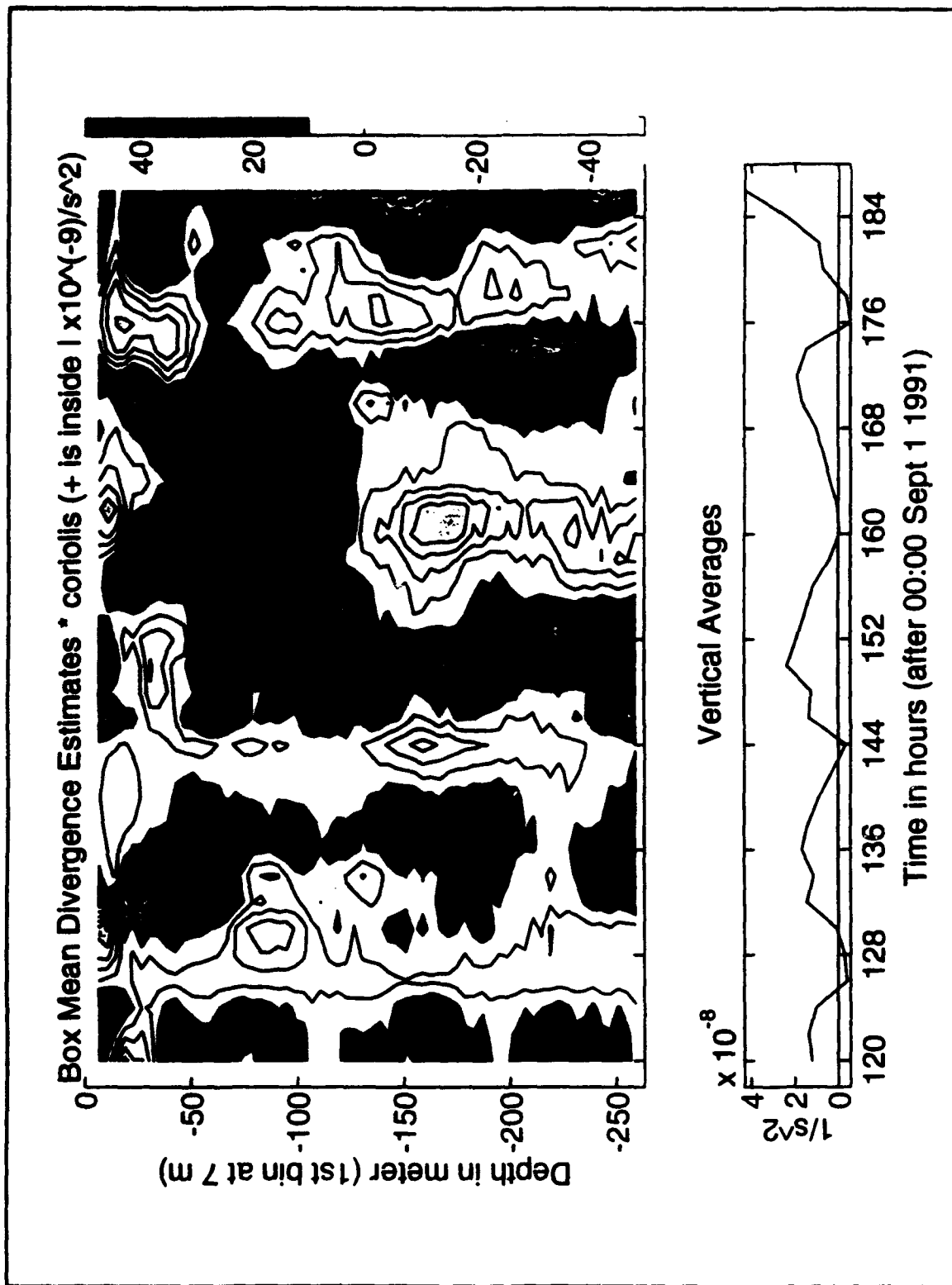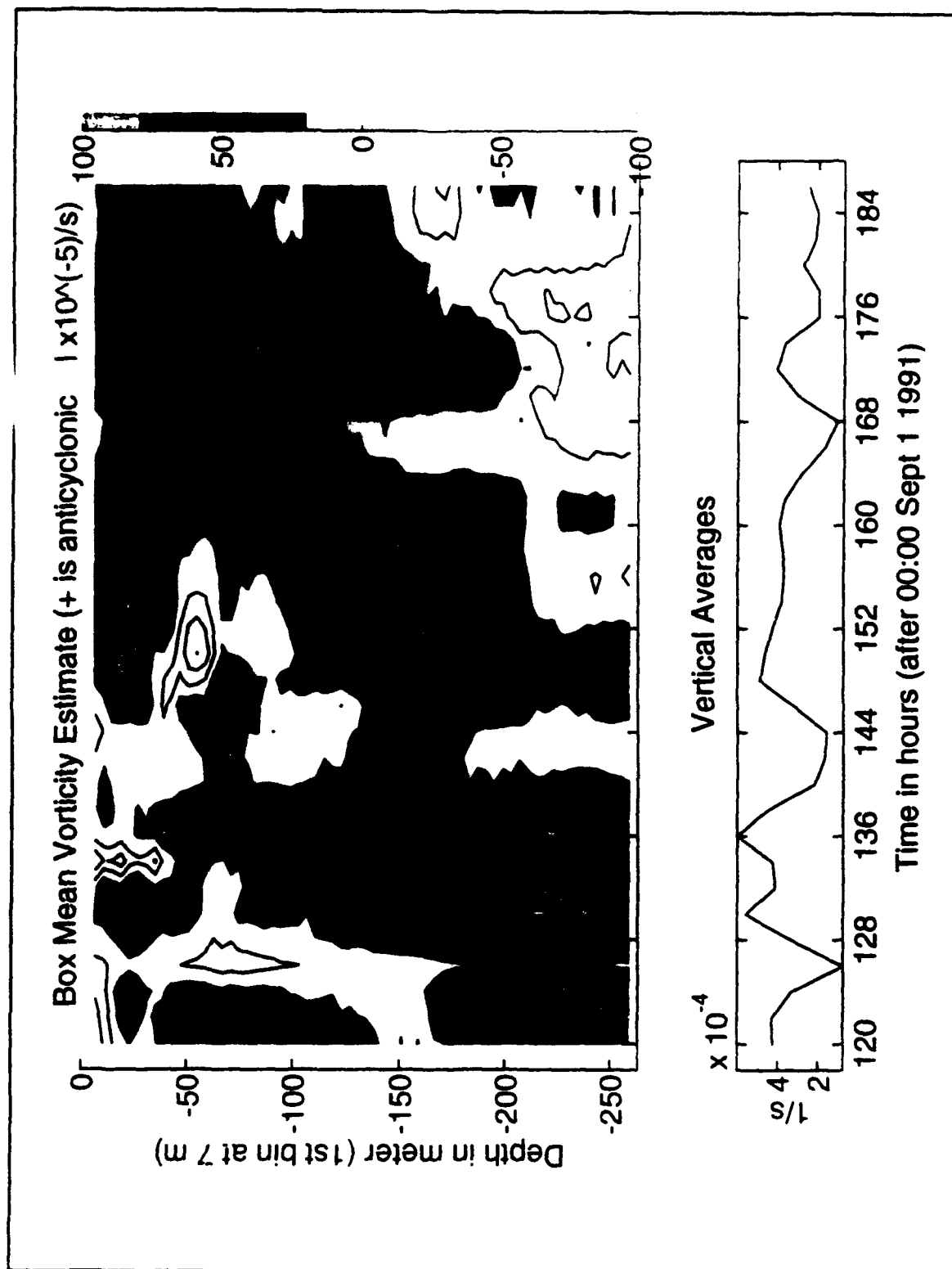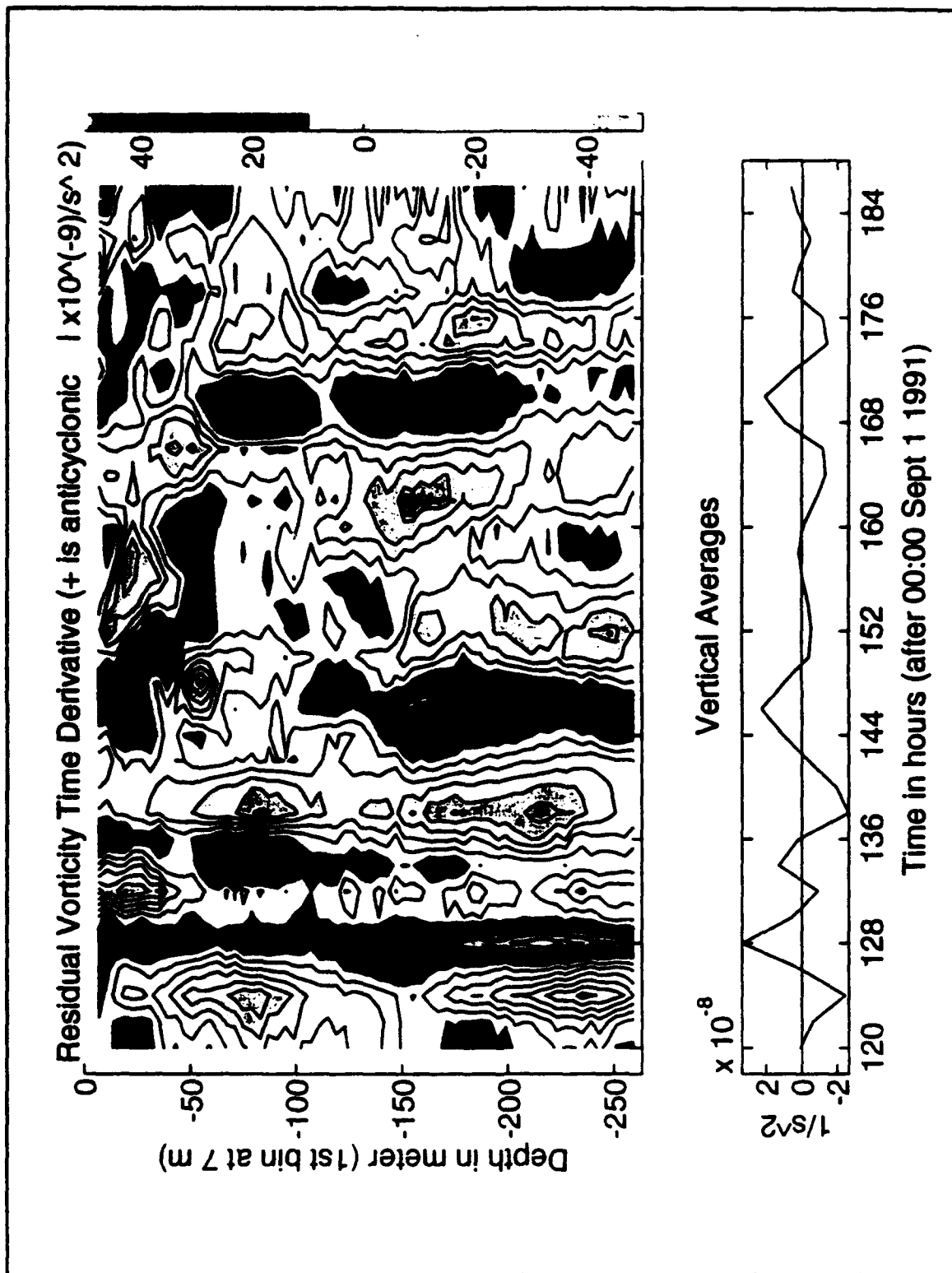
Figure III-A.6

Profiles of the temporal evolution of the absolute value of the current speed at 4 points selected along the west most leg. The hours shown in the x-axis are referred to the 0 hour of September 1 1991. Baroclinic bursts of absolute velocity are observed with an apparent period of 24 hours. See the text for a more detailed interpretation of the figure.
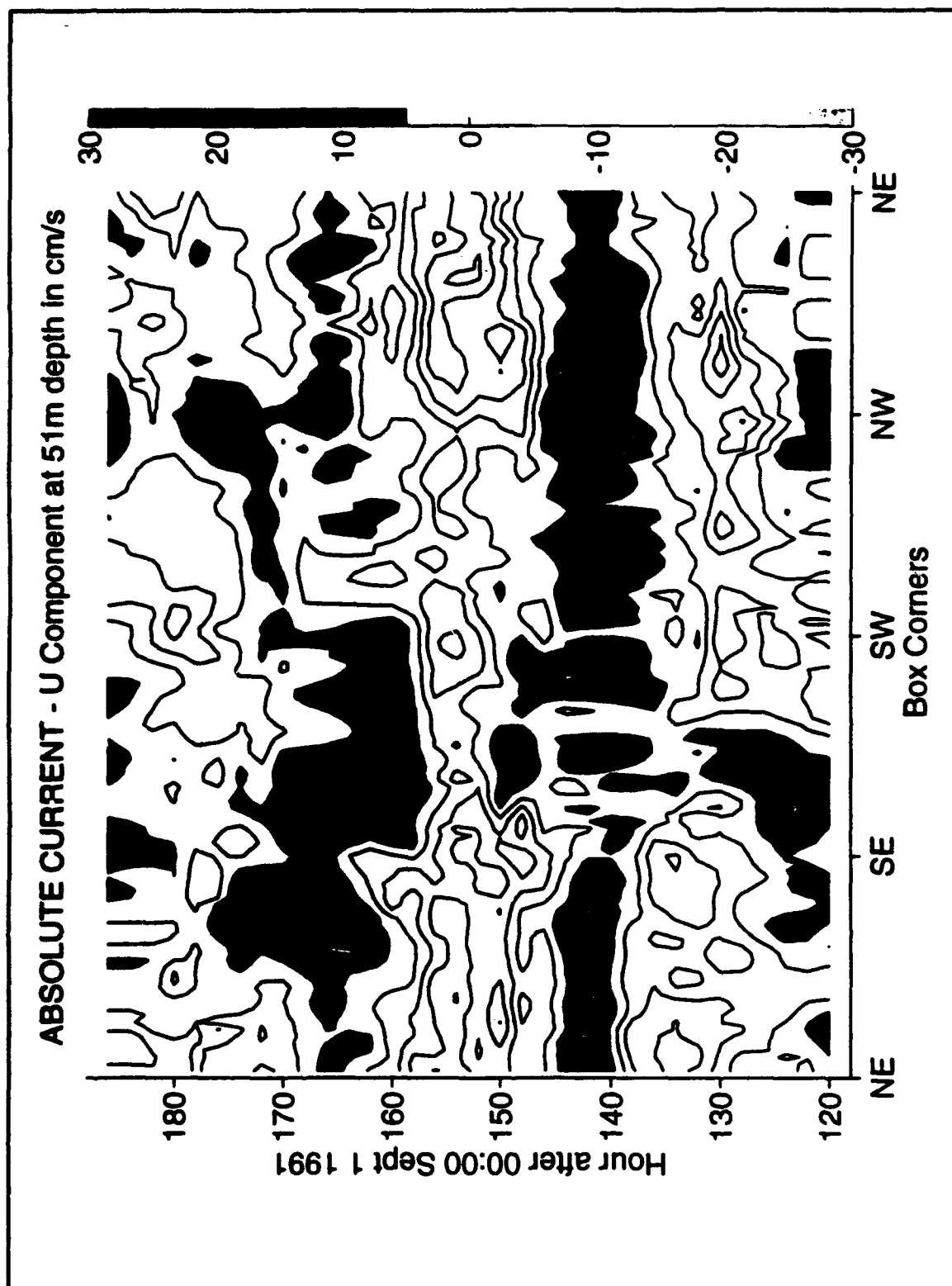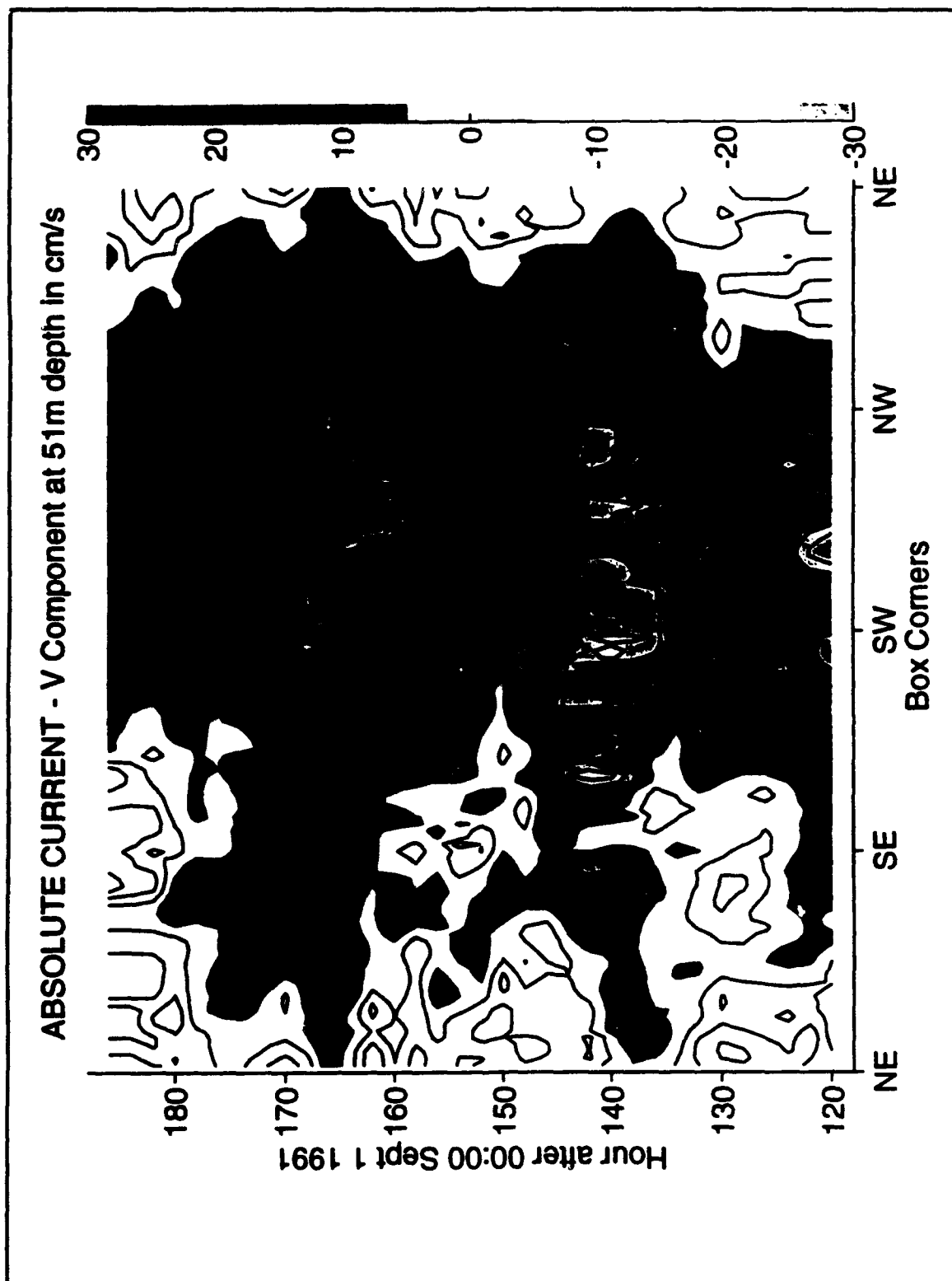
Figure III-A.6

139
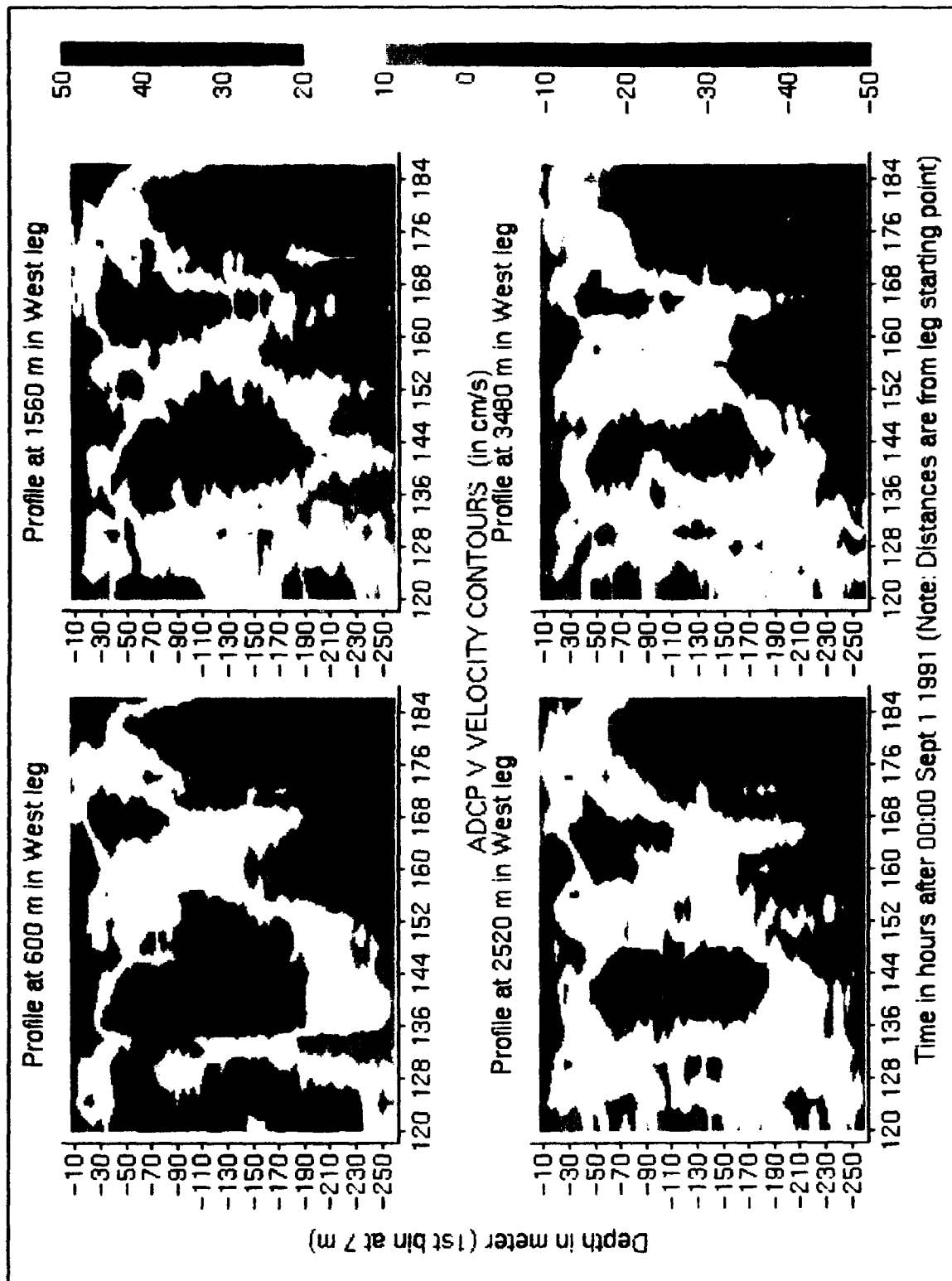
Figure III-B.1

Contours of the vertical structure of temperature at hour 124. Figure (i) corresponds to the east most leg, (ii) corresponds to the south most leg, (iii) corresponds to the west most leg and (iv) represents the north most leg. Temperature data between the surface and 8m depth corresponds to a linear interpolation between the sea surface temperature and the first CTD Tow-Yo data bin. Each panel represents the observed values along one leg. Each panel starts at the beginning of the correspondent leg in the following directions (NE-SE-SW-NW-NE). See the text for further interpretations.
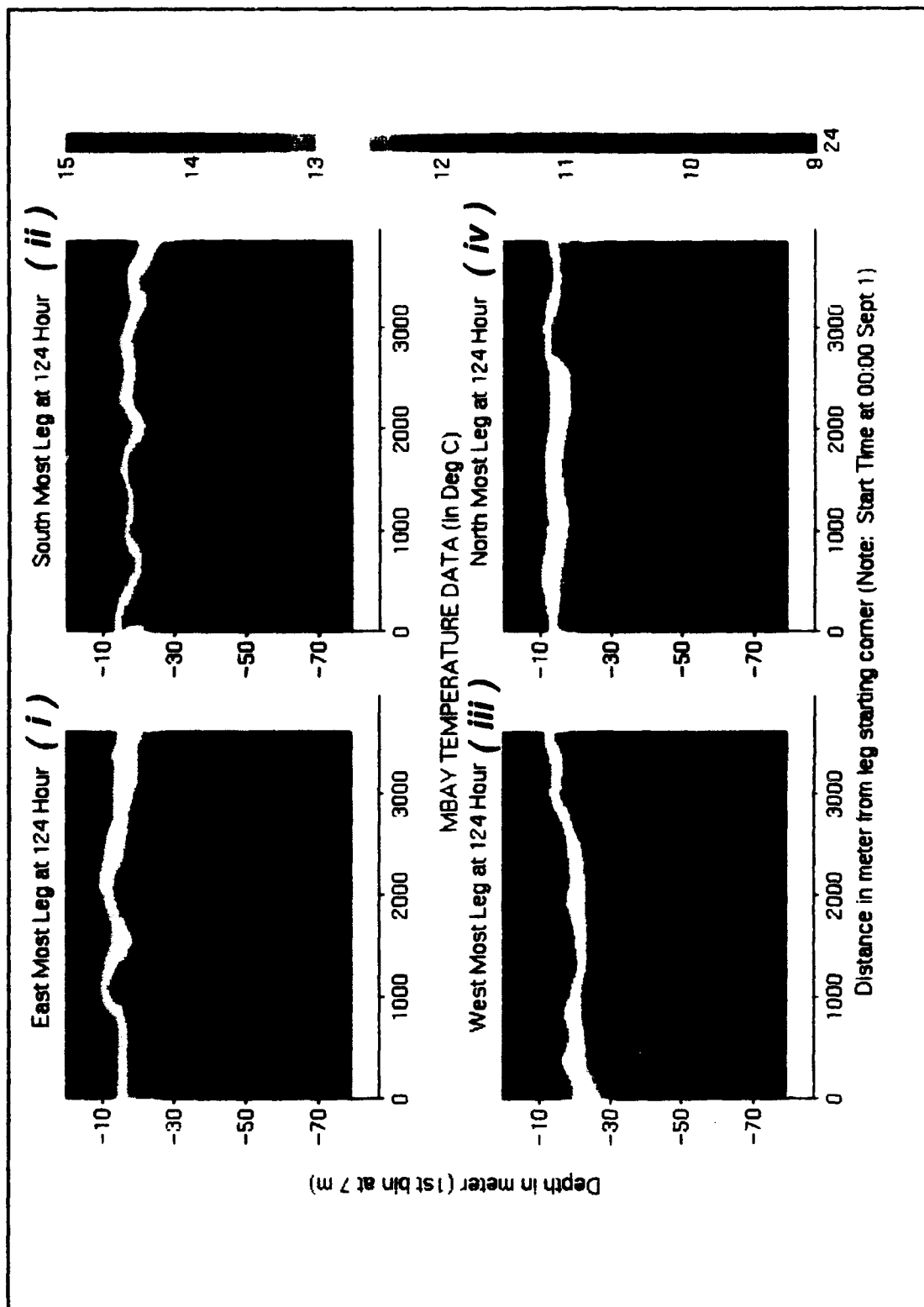
Figure III-B.1

141

Figure III-B.2

Contours of the vertical structure of temperature at hour 130. Figure (i) corresponds to the east most leg, (ii) corresponds to the south most leg, (iii) corresponds to the west most leg and (iv) represents the north most leg. Temperature data between the surface and 8m depth corresponds to a linear interpolation between the sea surface temperature and the first CTD Tow-Yo data bin. Each panel represents the observed values along one leg. Each panel starts at the beginning of the correspondent leg in the following directions (NE-SE-SW-NW-NE). See the text for further interpretations.
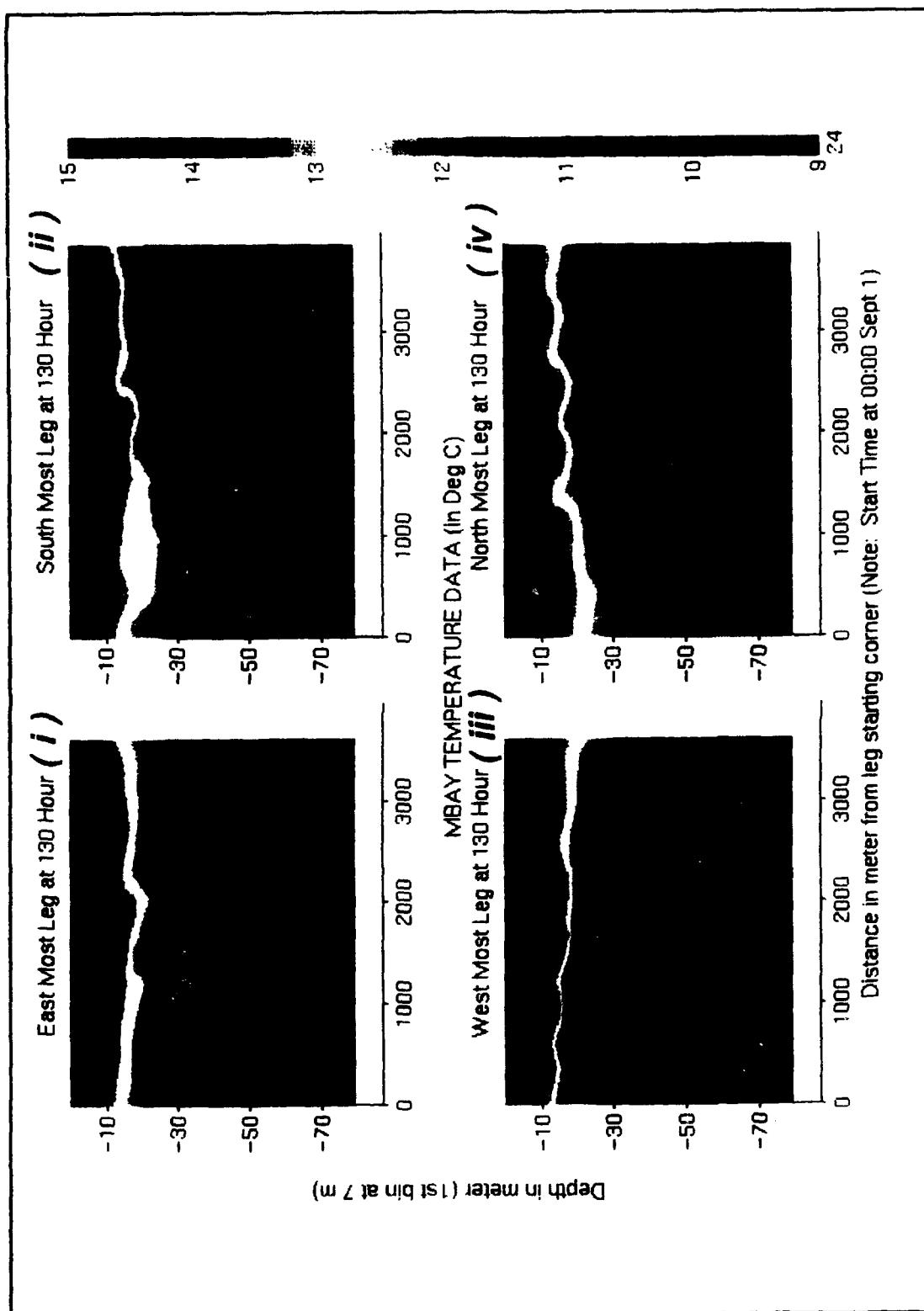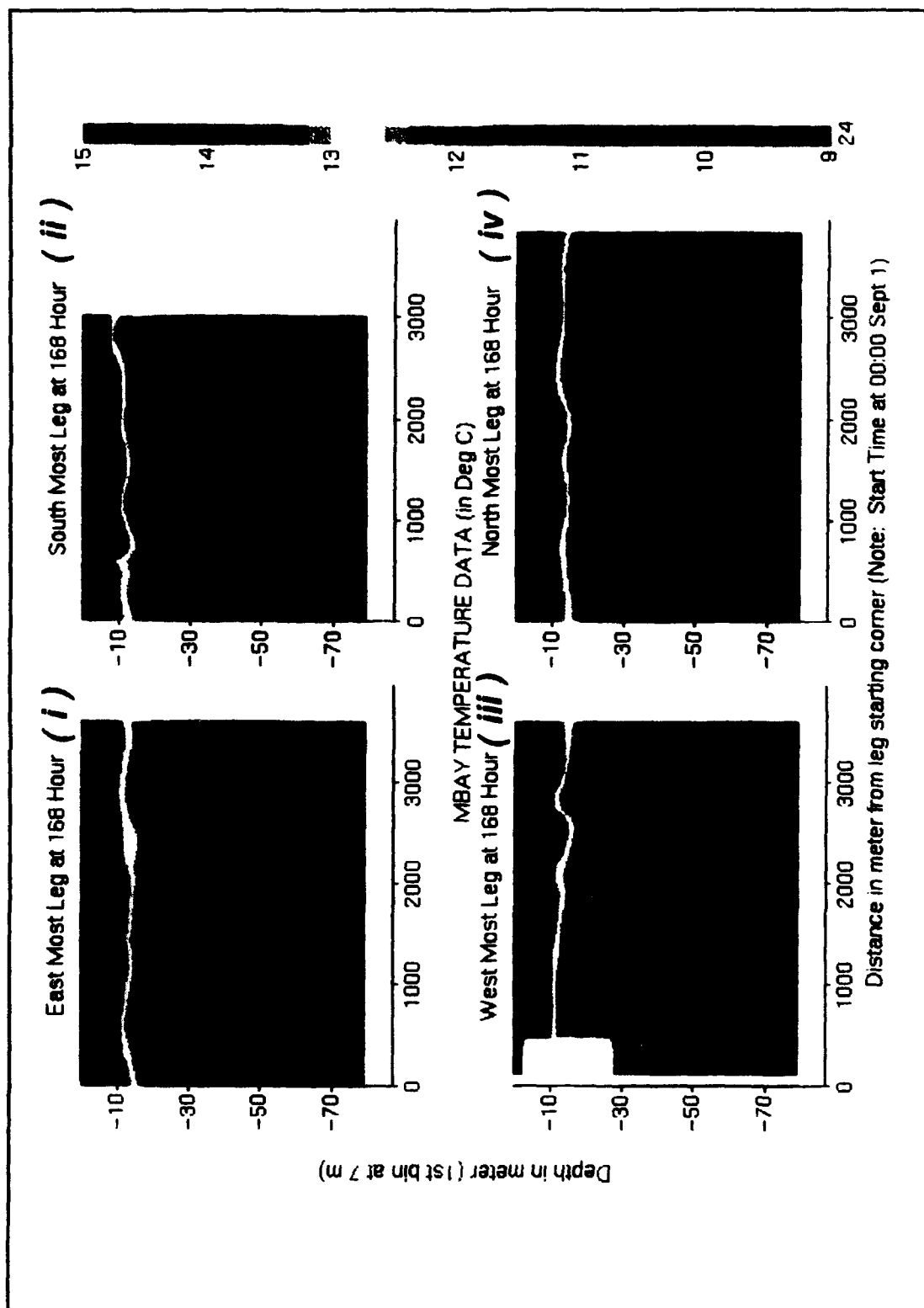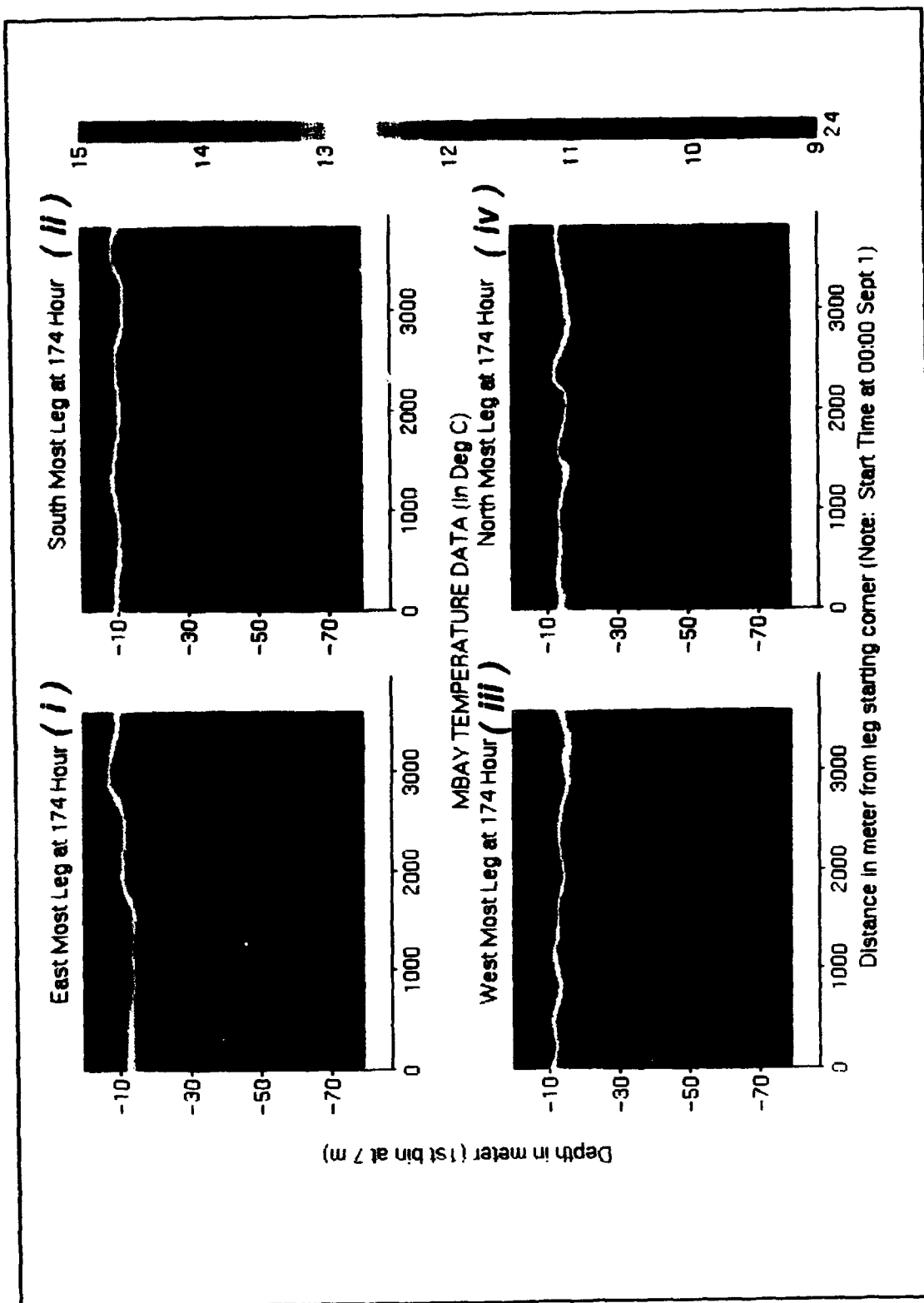
Figure III-B.2

Figure III-B.3

Velocity contours showing the time evolution around the sampled box at 19m depth (i.e., approximately the mean thermocline). Figures (a) and (b) correspond to the U and V current components respectively. Figure (b) shows northward currents occurring along the west leg with a tidal periodicity, though at hours 125, 170 and 185 some current enhancement can be observed. These currents are not similar to those shown in Figure III-B.4.b, that show a 24 hour periodicity; however, the northward strong surface currents between hours 180-185 in Figure IV-B.3.b are consistent with these observations. One should note that between hours 140 and 155 the weaker currents at 19m are almost simultaneous with the occurrence of strong vertical shear at this depth along the west leg, as can be seen in Figure III-C.3, suggesting that part of the kinetic energy might have been used for mixing due to a shear instability process.

Figure III-B.3 (a)

145

Figure III-B.3 (b)

146
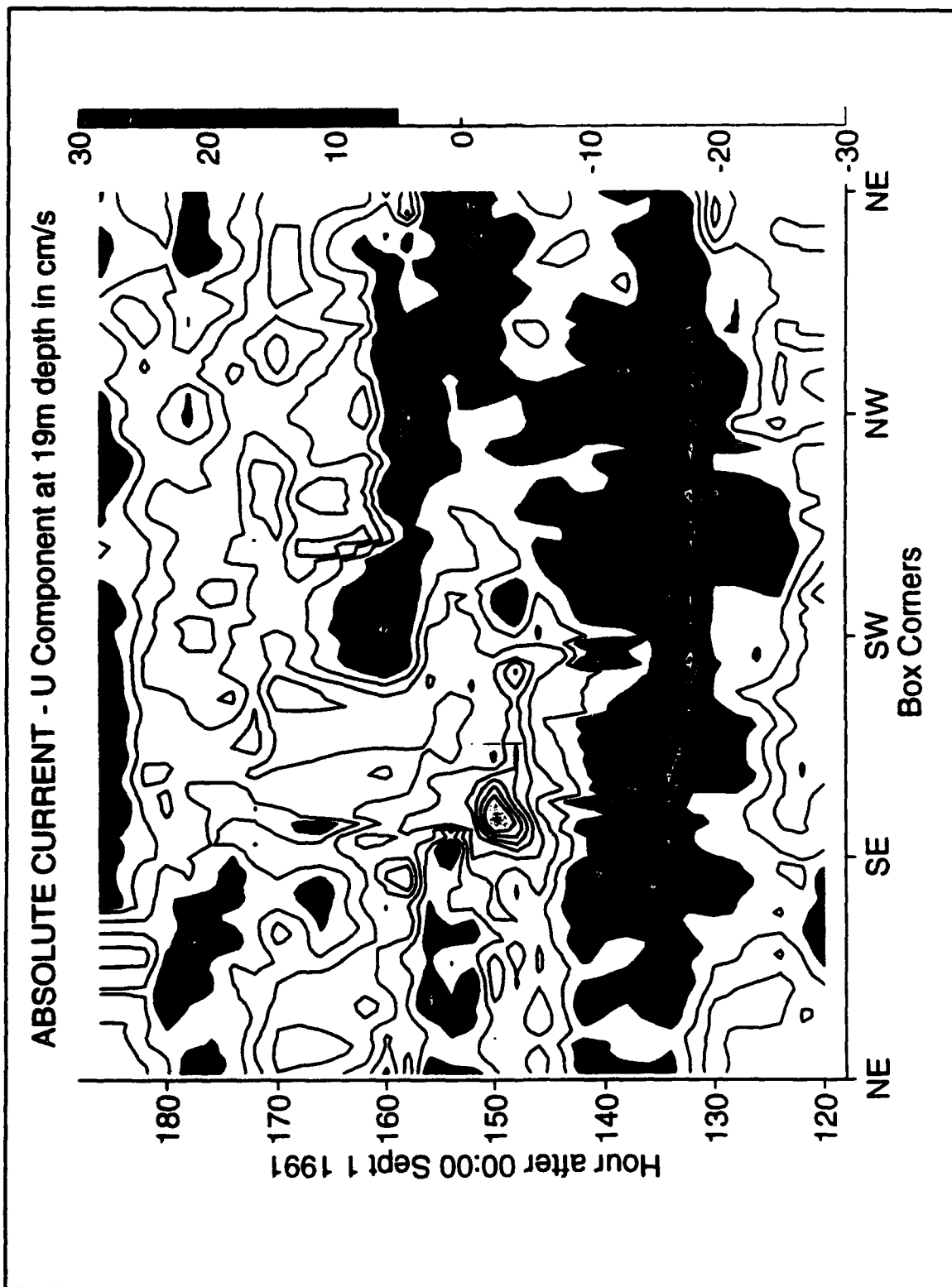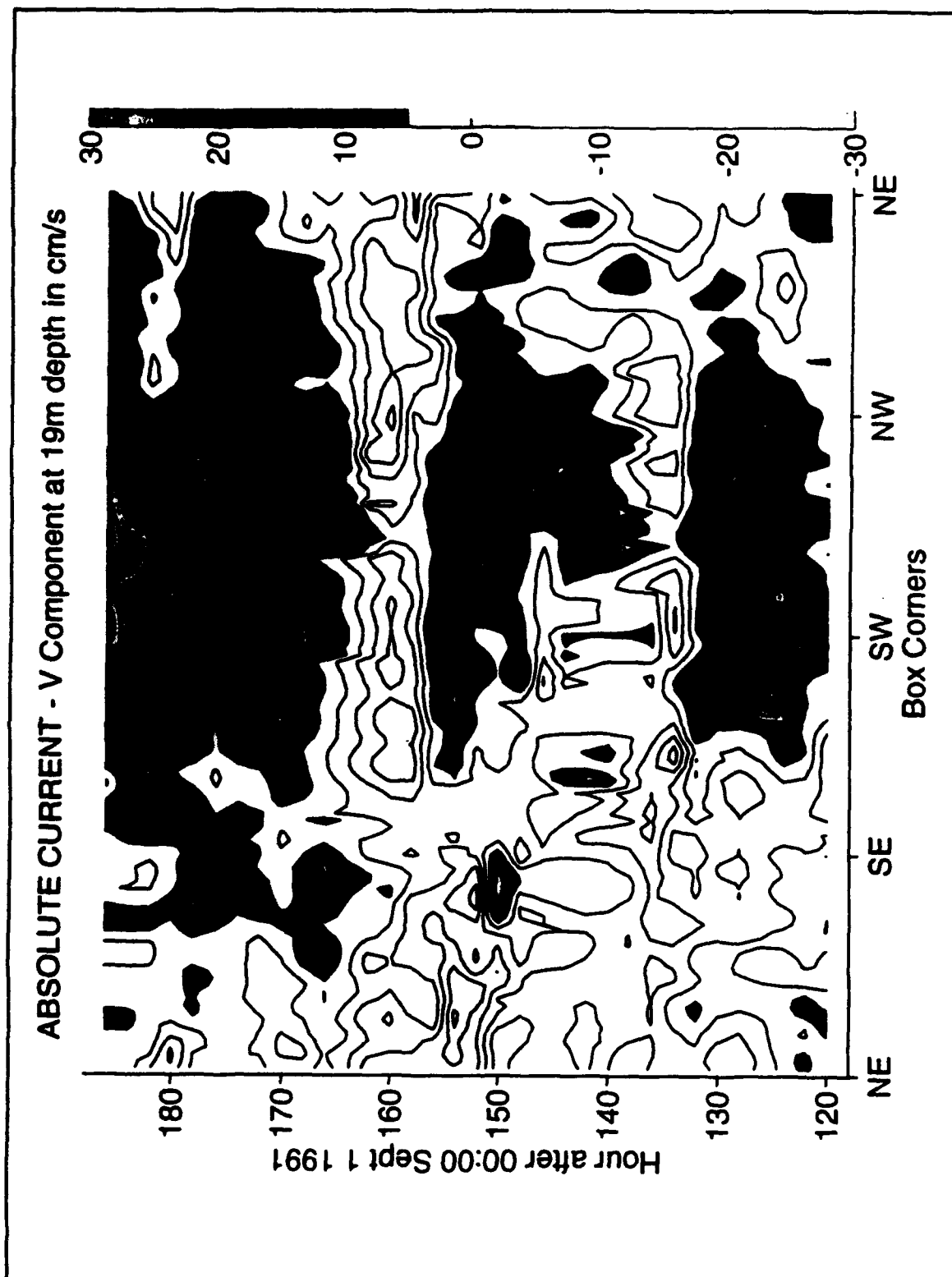
Figure III-B.4

Velocity component contours showing the time evolution around the sampled box at 11m depth. Figures (a) and (b) correspond to the U and V current components respectively. Figure (a) shows a near surface eastward current component throughout the box until hour 156, when this component shifts to a westward direction throughout the box. This shift seems to propagate along the west leg between hours 150 and 160. Figure (b) show that the V component at this depth is following the tidal cycles until hour 165, after which a strong surface northward current starts at the beginning of the west leg and spreads toward the north-west *corner* *between* *hours* 165 and 180. After hour 180 the current reaches a maximum and becomes spatially confined to the western part of the surveyed area.

Figure III-B.4 (a)

148

ABSOLUTE CURRENT - V Component at 11m depth in cm/s
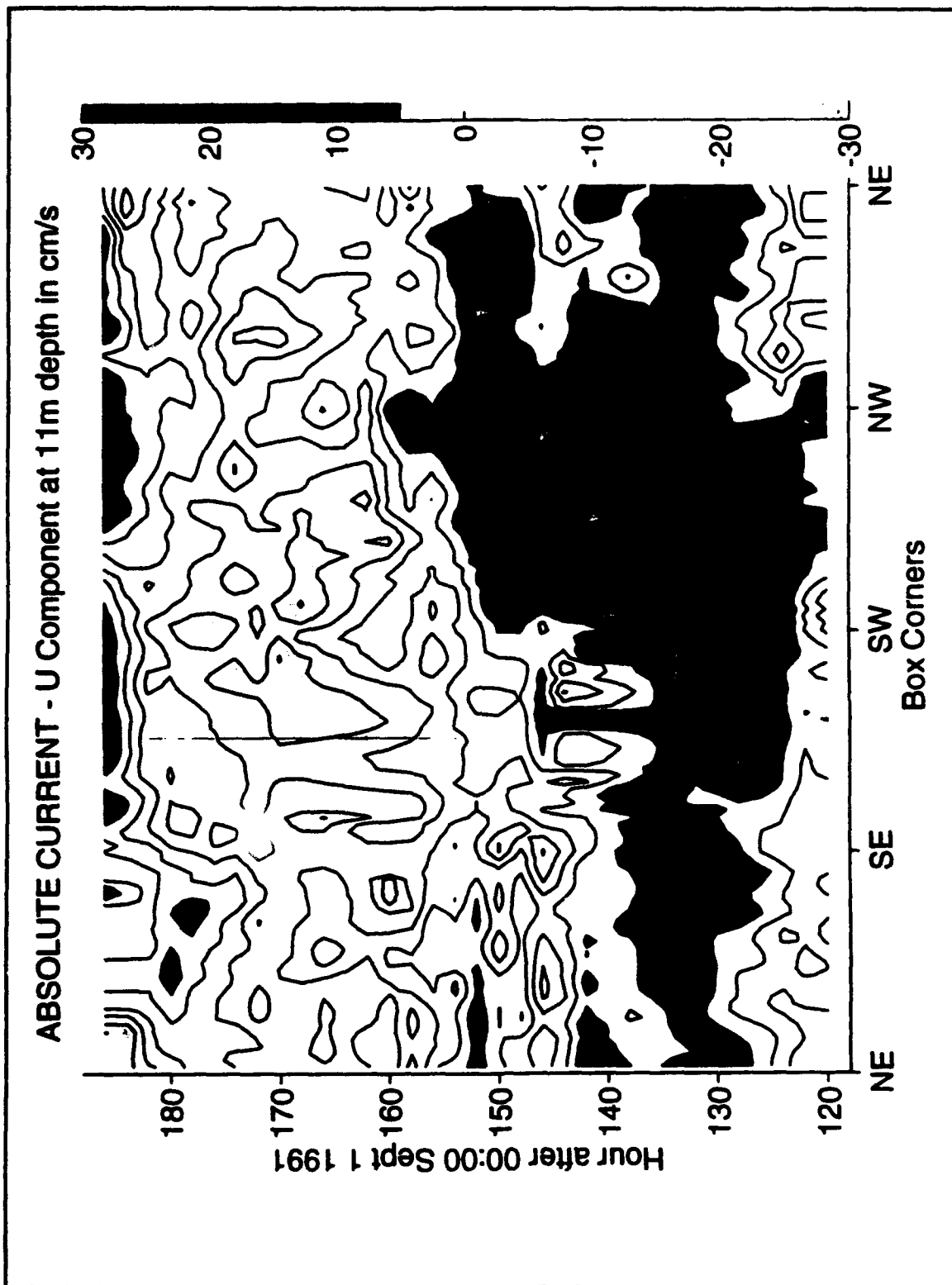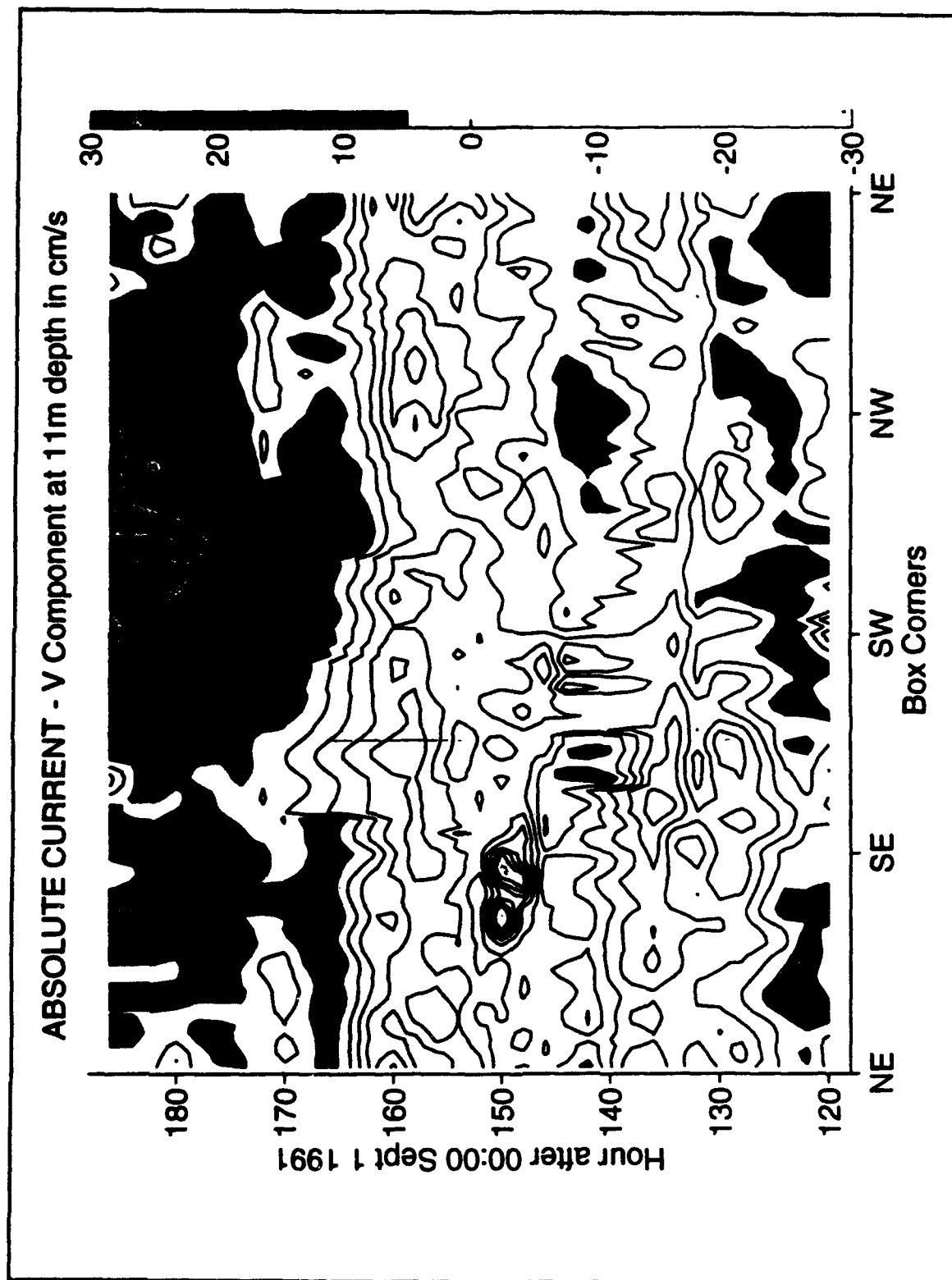
Figure III-B.4 (b)

Figure III-B.5

Velocity contours showing the time evolution around the sampled box at 51m depth. Figures (a) and (b) correspond to the U and V current components respectively. Figure (a) shows a U component following the tidal cycle until hour 170. Rapid temporal changes occur at the north-west corner after hour 150. Figure (b) shows the a strong northward V component along the west leg corresponding to bursts of kinetic energy 24 hours apart, in agreement with Figure IV-A.5. At the end of the time series, the following burst is weaker than the previous two. This attenuation is simultaneous with the occurrence of stronger currents at the surface of Figure IV-B.3.b.

Figure III-B.5 (a)

Figure III-B.5 (b)

Figure III-C.1

Contours of the vertical structure of temperature at hour 168. Figure (i) corresponds to the east leg, (ii) corresponds to the south leg, (iii) corresponds to the west leg and (iv) represents the north leg. Temperature data between the surface and 8m depth is a linear interpolation between the sea surface temperature and the first CTD Tow-Yo data bin. Each panel represents the observed values along one leg. Each panel starts at the beginning of the correspondent leg in the following directions (NE-SE-SW-NW-NE). See the text for further interpretations.

Figure III-C.1

Figure III-C.2

Contours of the vertical structure of temperature at hour 174. Figure (i) corresponds to the east leg, (ii) corresponds to the south leg, (iii) corresponds to the west leg and (iv) represents the north leg. Temperature data between the surface and 8m depth is a linear interpolation between the sea surface temperature and the first CTD Tow-Yo data bin. Each panel represents the observed values along one leg. Each panel starts at the beginning of the correspondent leg in the following directions (NE-SE-SW-NW-NE). See the text for further interpretations.

Figure III-C.2

Figure III-C.3

This figure shows 8 meter vertical shear magnitudes at 4 equally spaced points selected along the west leg. The strong shear above 30m depth after hour 150 in the profiles of point '600m' is simultaneous with the rapid variation of the surface current of Figure III-B.3.a, and with the attenuation of the rectification process at the thermocline, as shown in Figure III-A.5 on the profiles at point '600m' and in Figure III-C.4.b along the west leg. This strong shear could be associated with the start of the internal mixed layer observed in Figure III-C.1.a at the west leg.

Figure III-C.3

158
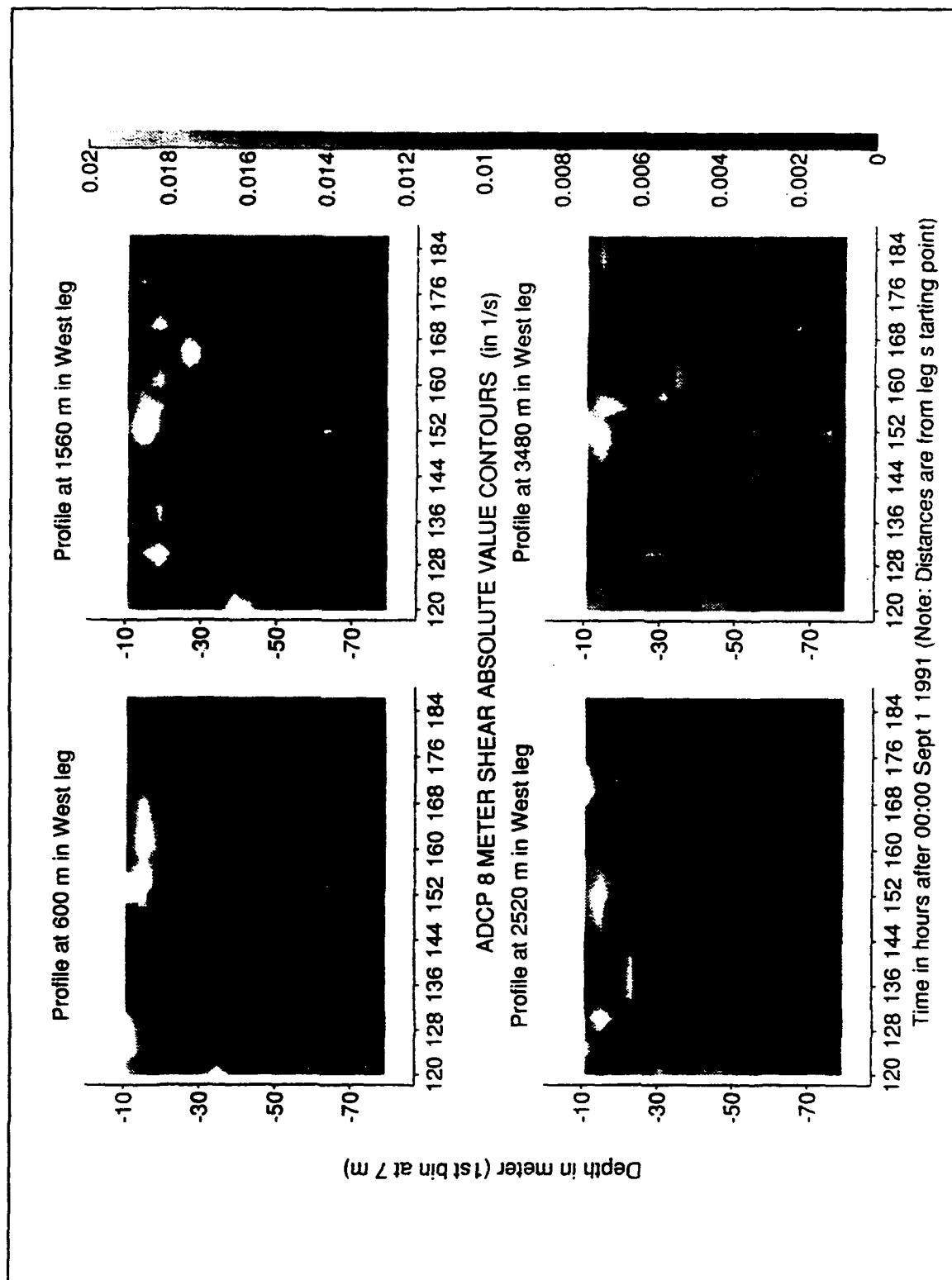
Figure III-D.1

Current meter time series (a), simultan   th the MBAY survey from a mooring instrumented with temperature (i), eastward (U) velocity component (ii) and northward (V) velocity component (iii) measurements. The hours displayed along the x-axis correspond to hours after 0:00 of September 1, 1991. The MBAY cruise was from hours 120 to 186. Spectral estimates were computed for 128 hours segments and are shown in Figures (b), (c) and (d), for temperature (in potential energy units), and U and V velocities respectively. The location of the mooring was within 2000m north of the center of the north leg, as shown in Figure II-A.1. A semidiurnal tidal signal is evident on the temperature and U time series, which is nearly aligned with the canyon axis, though the spectral estimates also show a significant peak at the 24 hour period. The temperature time series show significant drops of $0.6°C$ 24 hours apart, though smaller ones can be observed between them. The persistence of the spectral estimates in time suggests that there were no abnormal features present, so the present data can be assumed to be typical for this time of the year in this area.
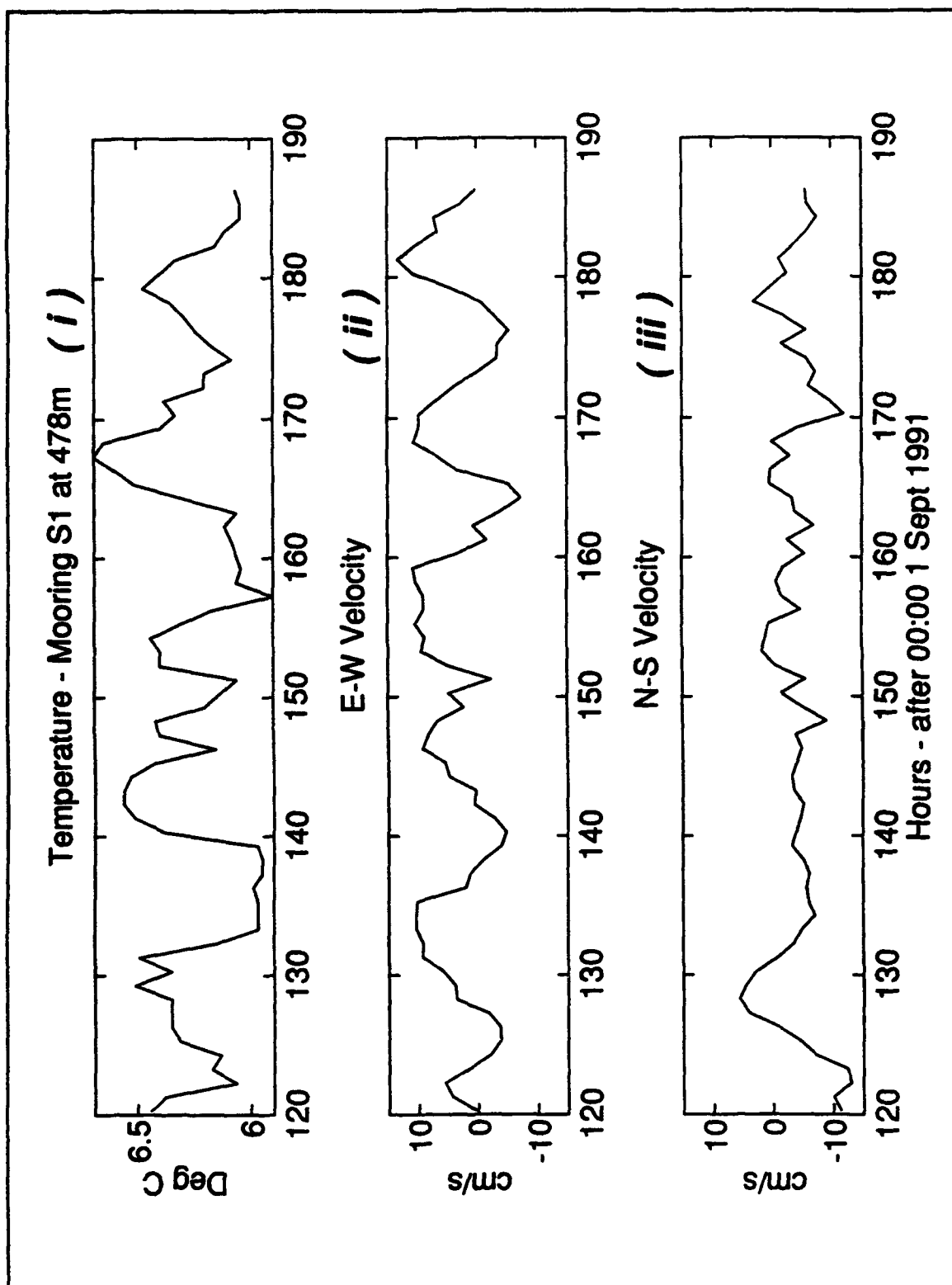
Figure III-D.1 (a)
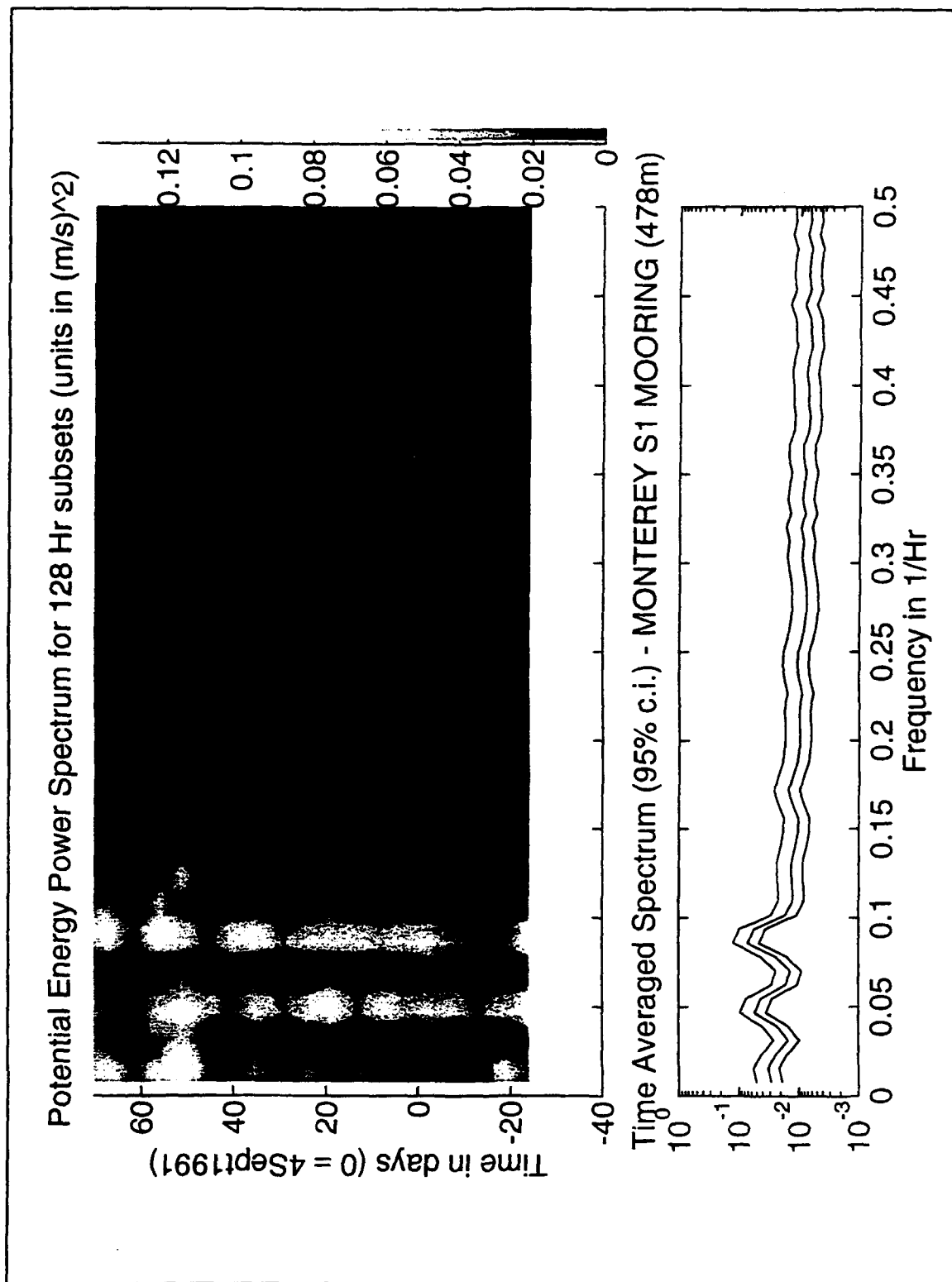
Figure III-D.1 (b)
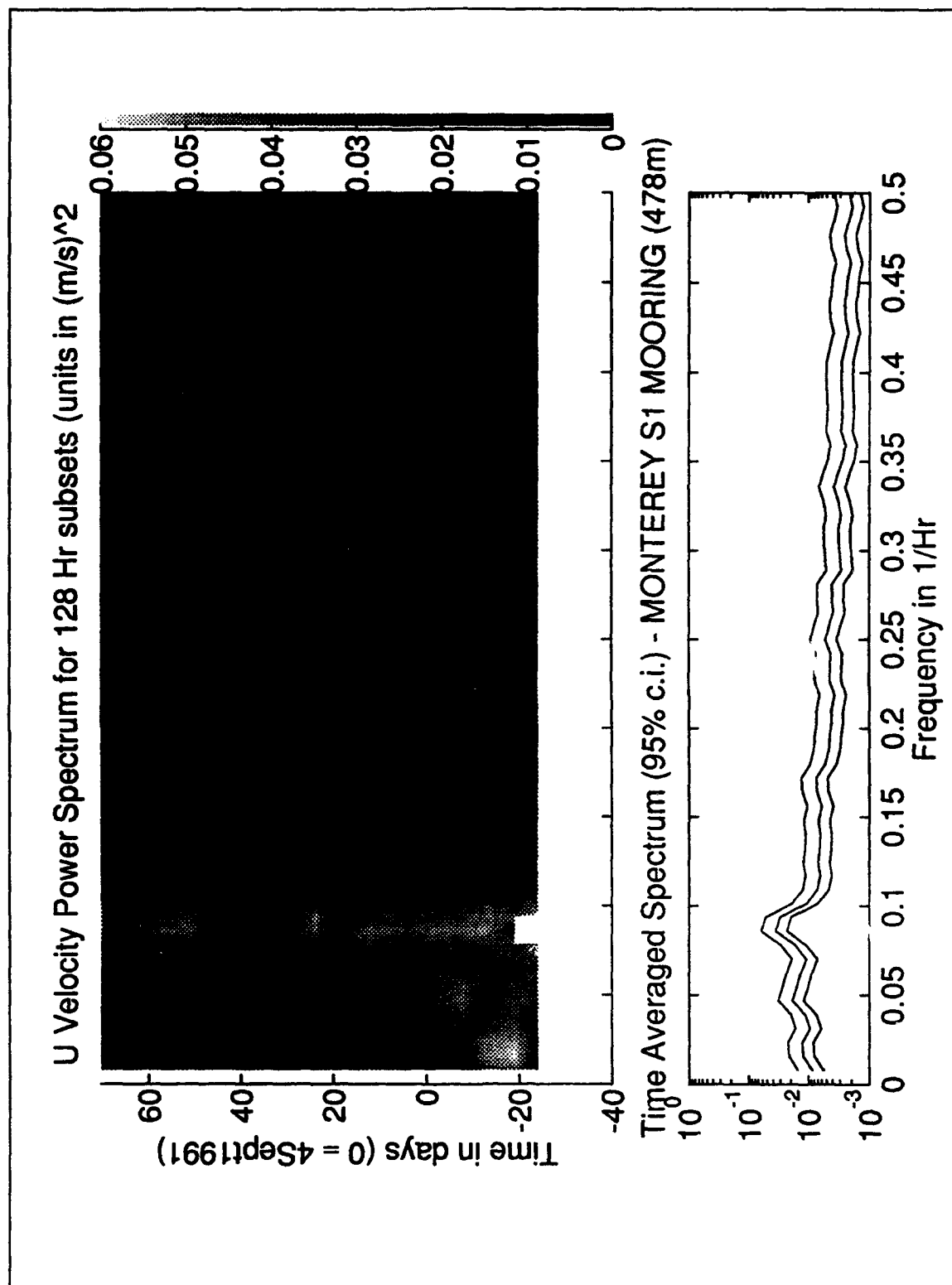
Figure III-D.1 (c)

Figure III-D.1 (d)

163
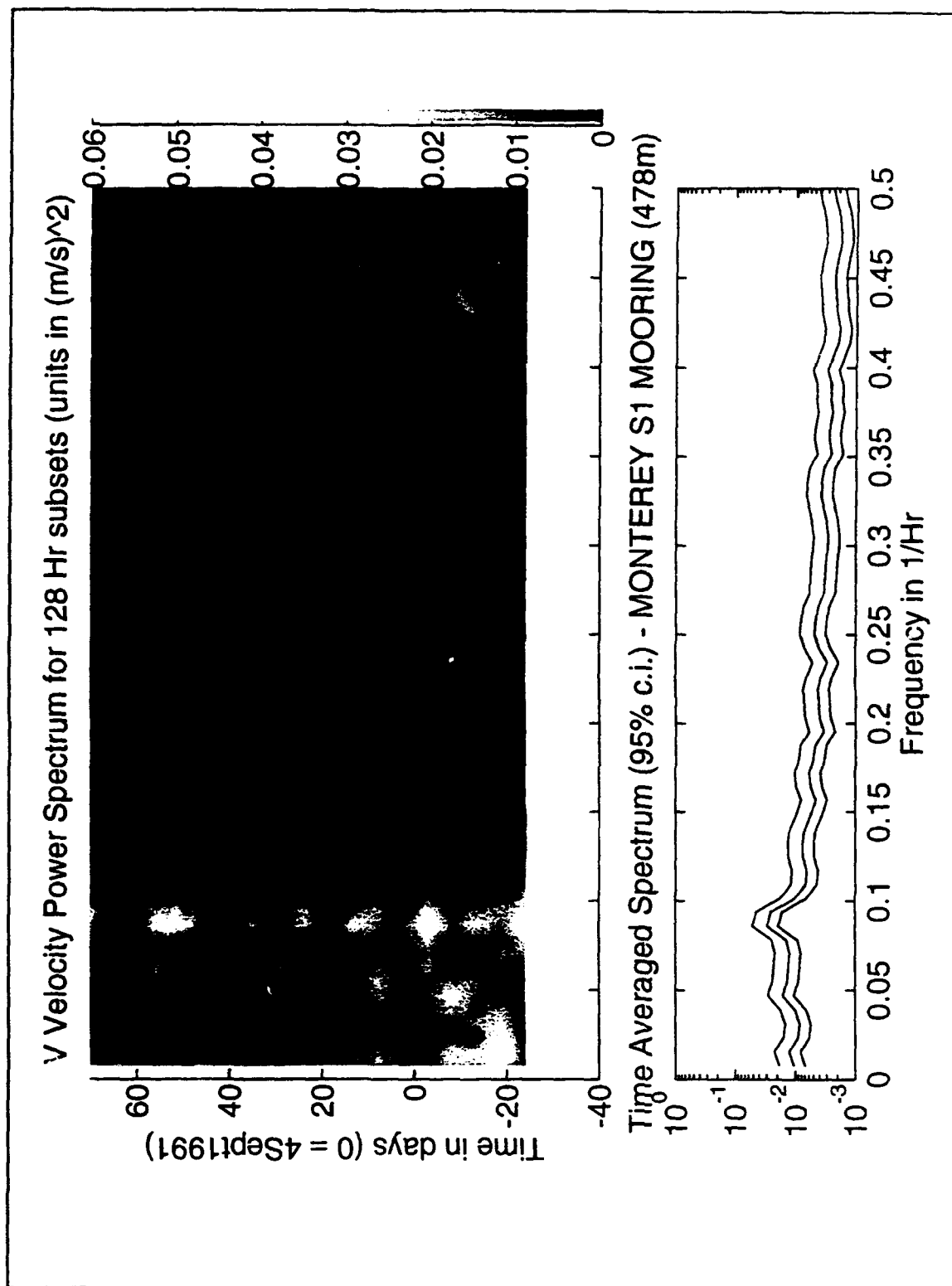
Figure III-D-2

Schematic representation of vorticity generation mechanisms in a tidal flow over topography:(a) potential vorticity conservation-column stretching and squeezing; (b) differential friction due to velocity shear (for quadratic friction law); (c) differential friction due to lateral depth gradients; (d) asymmetrical depth profile changes [from Robinson, 1985, fig.7.7].
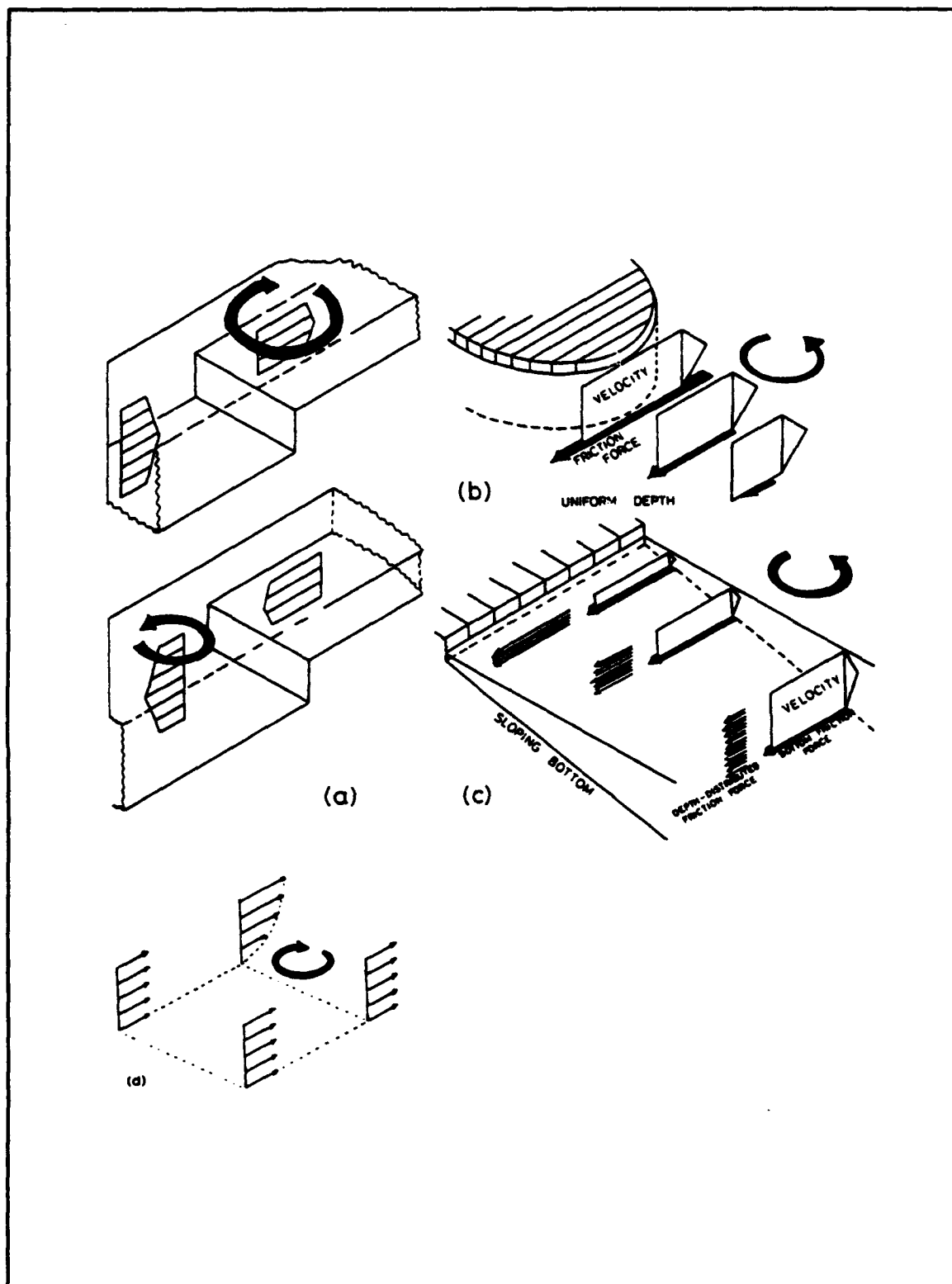
Figure III-D.2

Figure IV-A.1

Tidal velocity amplitudes over the simplified continental slope taken as representative of the topography in the MBAY vicinity. Figure (a) represents the cross-shore (U) horizontal tidal component increasing in magnitude as depth shallows. Figure (b) shows the consequent, bottom induced vertical velocity (W) amplitudes, that are in-phase with the horizontal cross-shore velocities. The horizontal velocity amplitudes were computed assuming kinetic energy conservation with a rigid lid assumption. The vertical velocities were then derived by continuity assuming no velocity normal to the vertical boundaries. This velocity field was used for the characterization of the internal tidal field in the MBAY area and for the study of nonlinear internal tide propagation, where it was taken as the non-stationary mean velocity field on which the waves propagate. Figure (c) displays the resultant internal tide forcing term $(N^2 W/\omega_T)$ as derived by Baines (1982) taking into account the assumed stratification for the MBAY conditions, as discussed in the text.
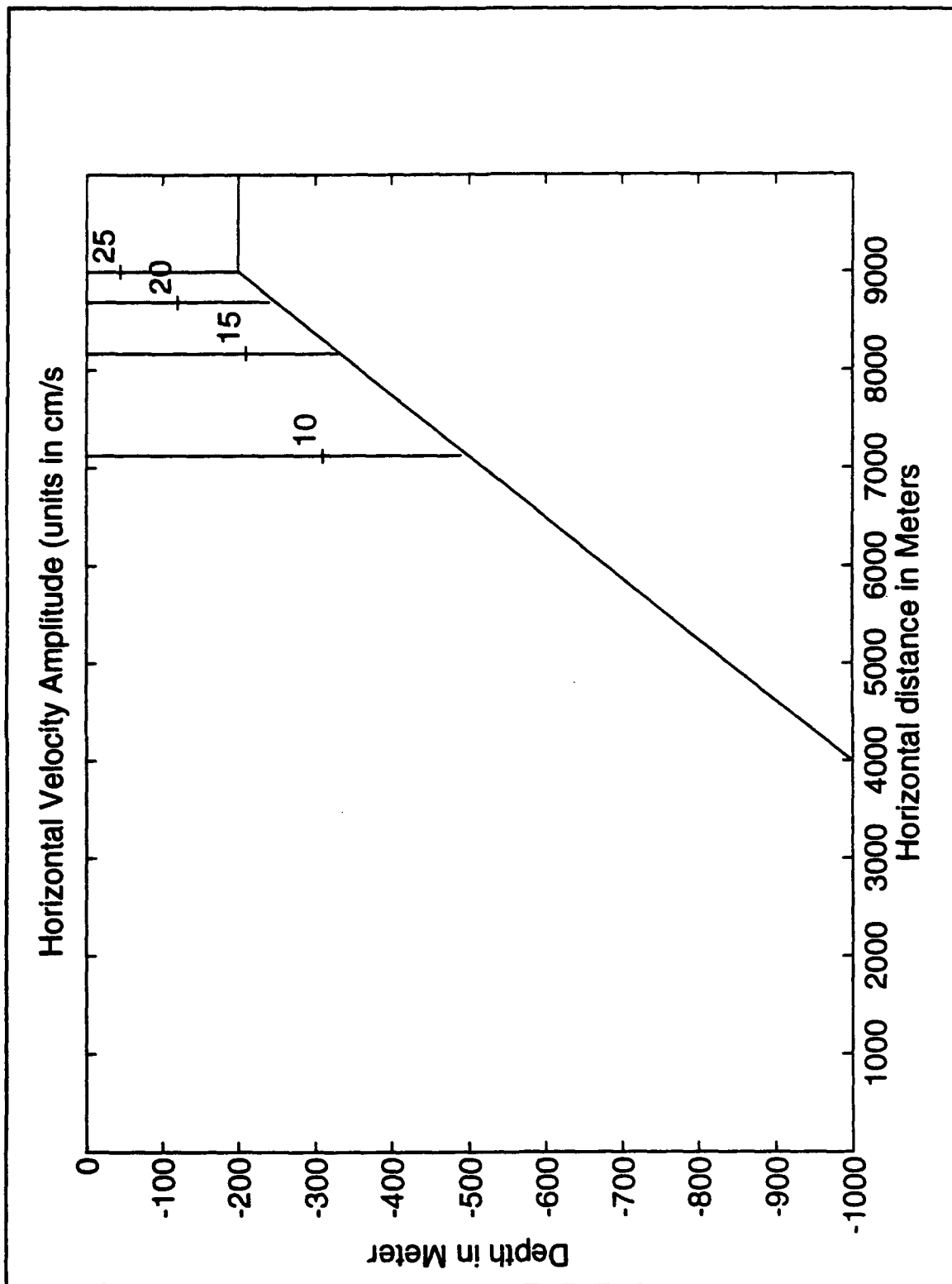
Figure IV-A.1 (a)
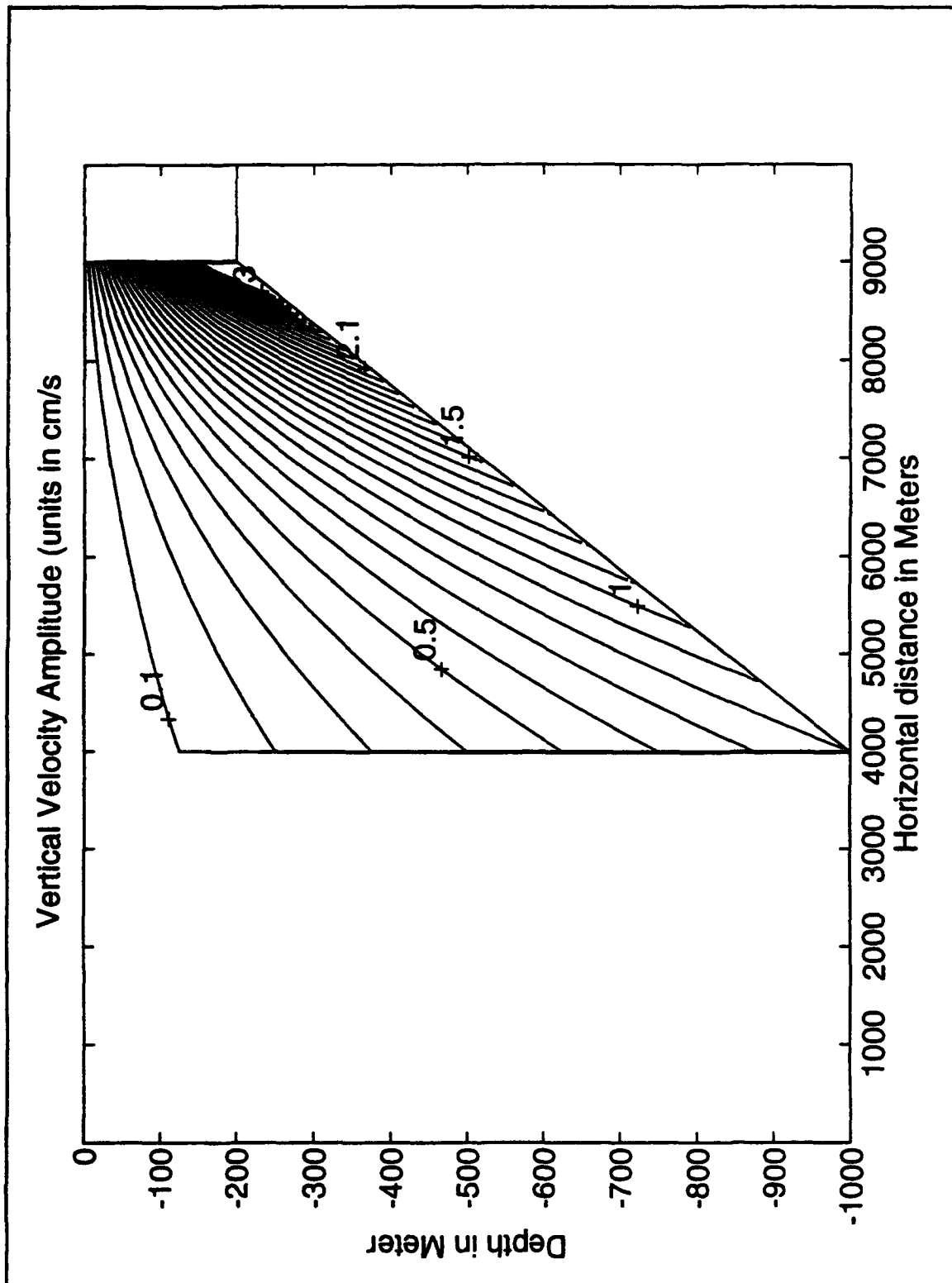
Figure IV-A.1 (b)

Figure IV-A.1 (c)

169
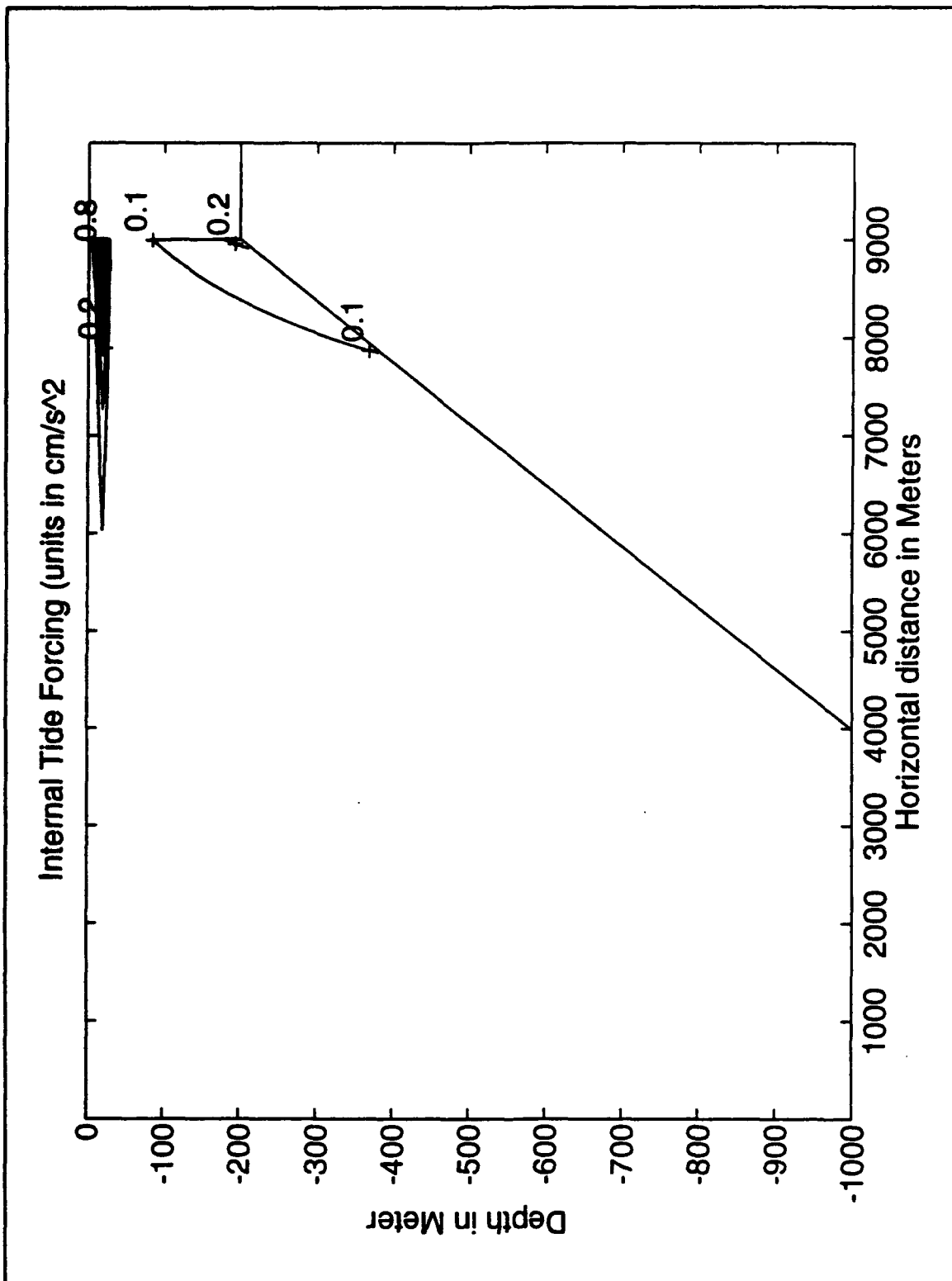
Figure IV-C.1

Ray paths for run #1 along the grid representing an attenuated continental slope relative to MBAY conditions, extending for 10 Km between the 18 Km and 8 Km distances with depth ranging from 200 to 1000m. Figure (a) shows vertical sections of the rays and Figure (b) the top view (horizontal paths). See text for interpretation of these results.

Figure IV-C.1 (a)

171

Figure IV-C.1 (b)

172
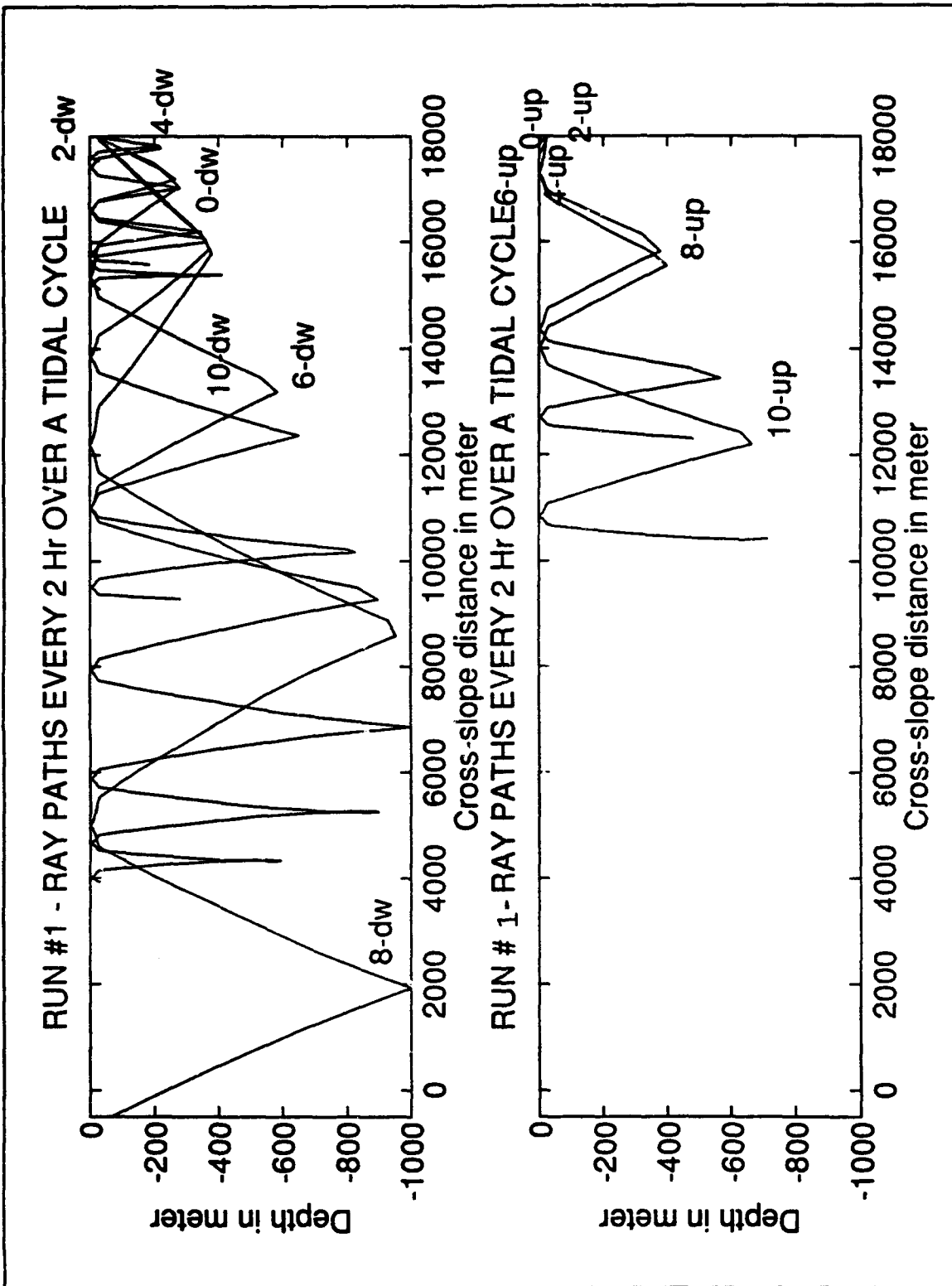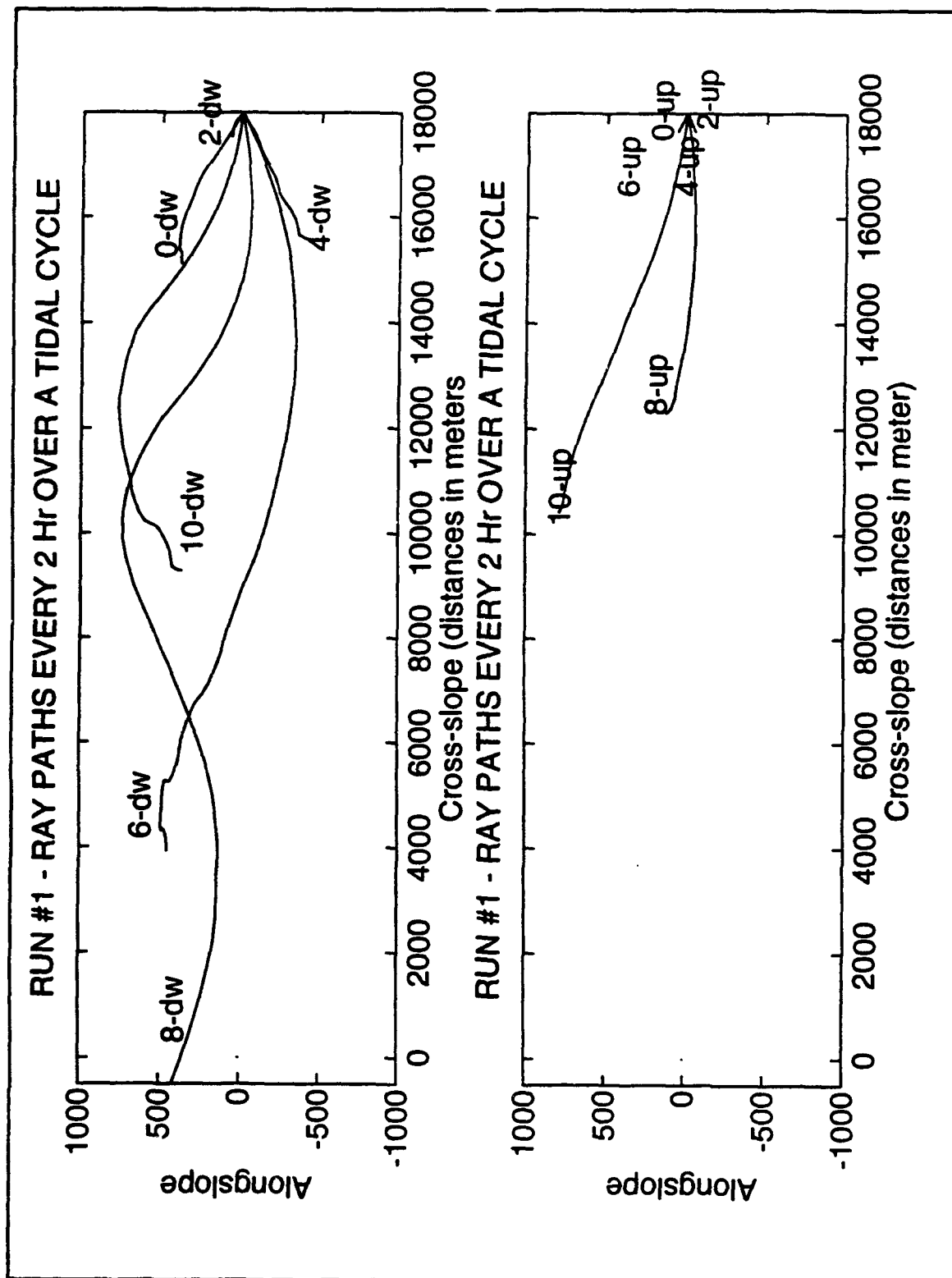
Figure IV-C.2

Ray initial velocity amplitudes for run #1 along the cross-shore axis. The shelf break is at 18 Km and the rays are propagating towards decreasing values. The horizontal axis identifies each ray path by the corresponding starting time. The letters 'up' and 'dw' identify initially upward and downward rays respectively. The velocity amplitudes were computed from the wave action and intrinsic frequency along the rays for an initial wave velocity amplitude of 0.15 m/s. This run was forced with waves having six times the tidal frequency and the typical length scales derived in IV-A. See text for interpretation of these results.
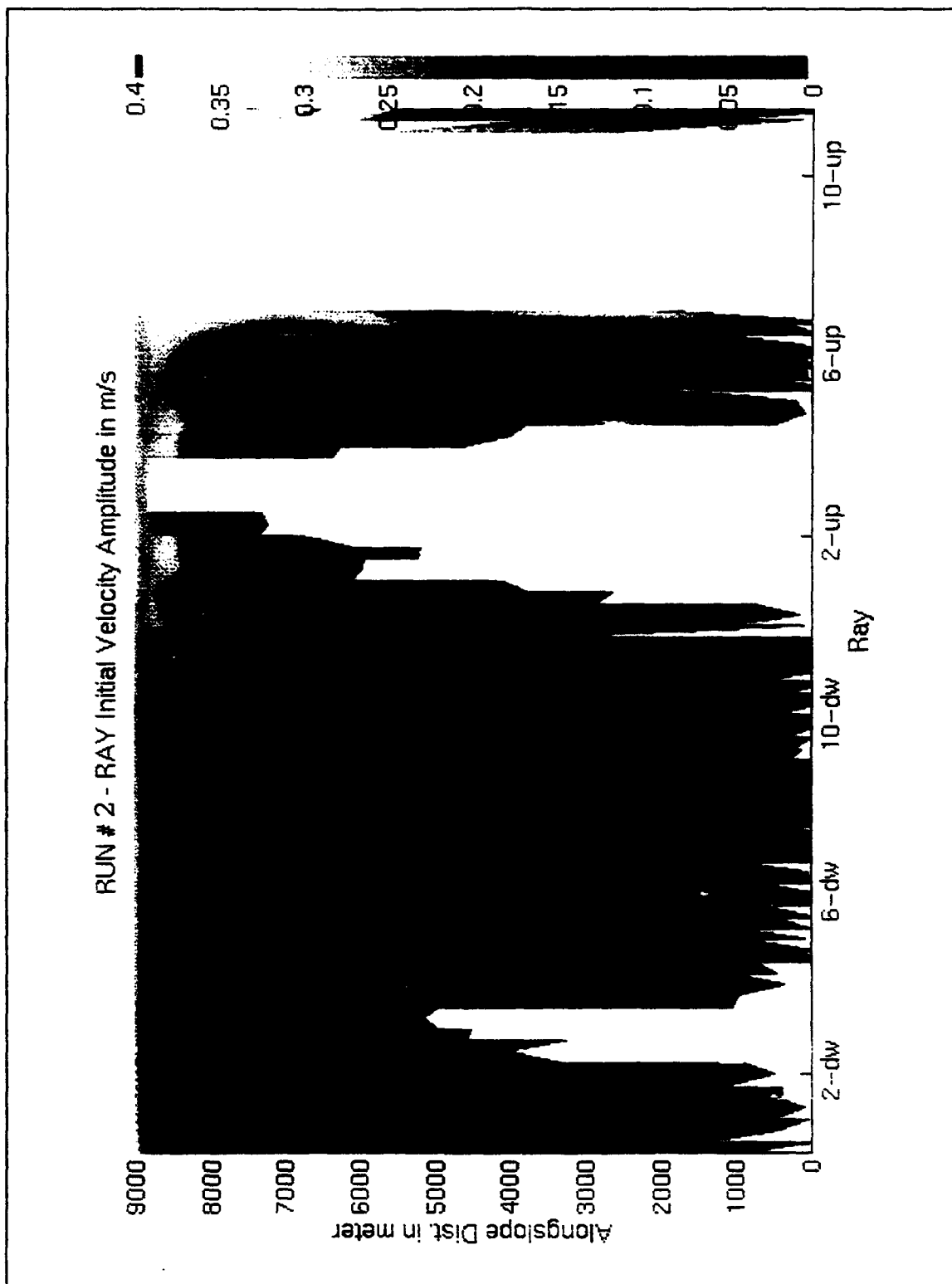
Figure IV-C.2

174
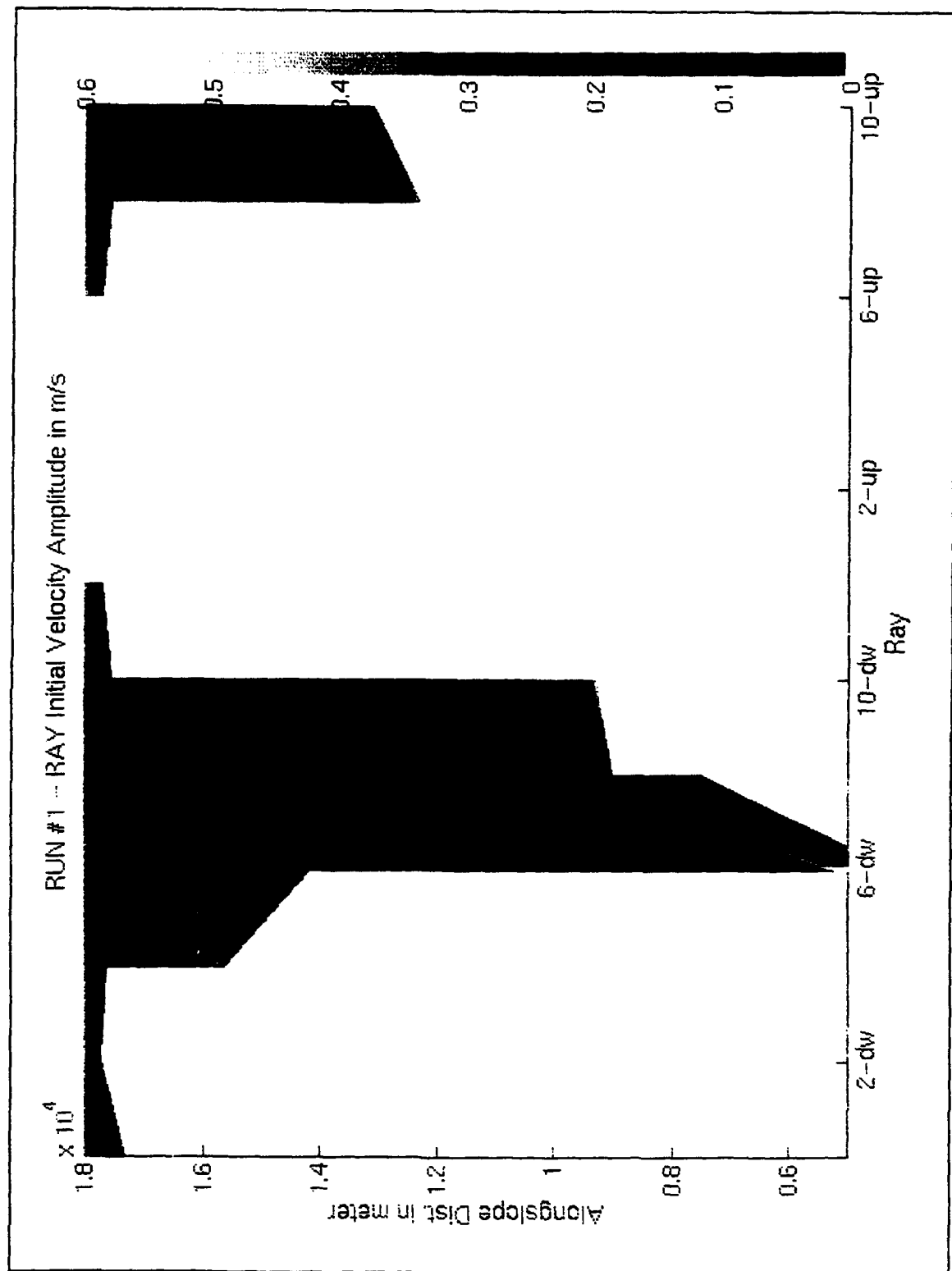
Figure IV-C.3

Ray paths for run #2 along the grid representing a continental slope similar to MBAY conditions, extending for 5 Km between 9 Km and 4 Km distances and with depth ranging from 200 to 1000m. Figure (a) shows vertical sections of the rays and Figure (b) the top view (horizontal paths). This run was forced with waves having twice the tidal frequency and a typical length scale of 7Km, as derived in IV-A. See text for interpretation of these results.
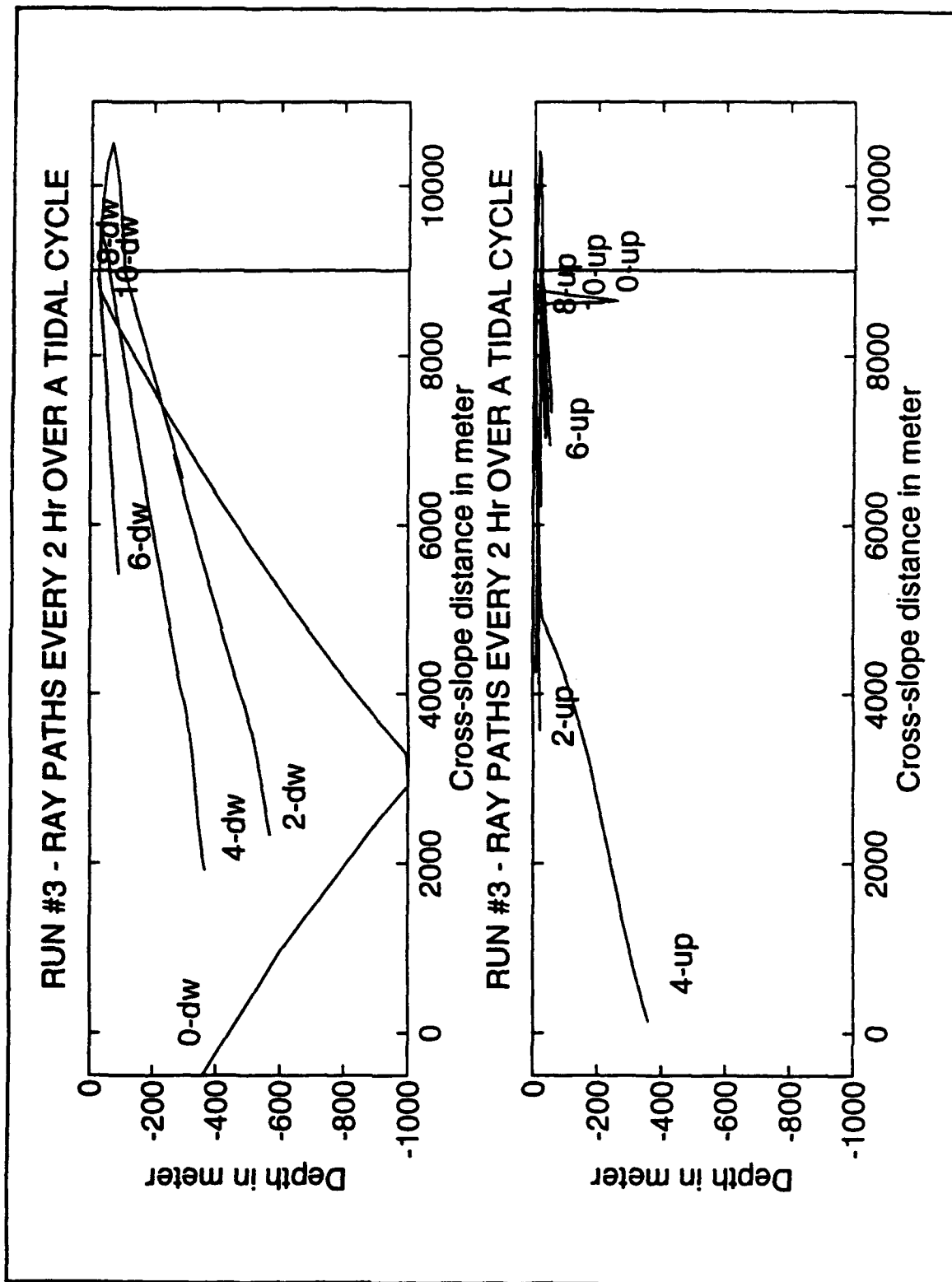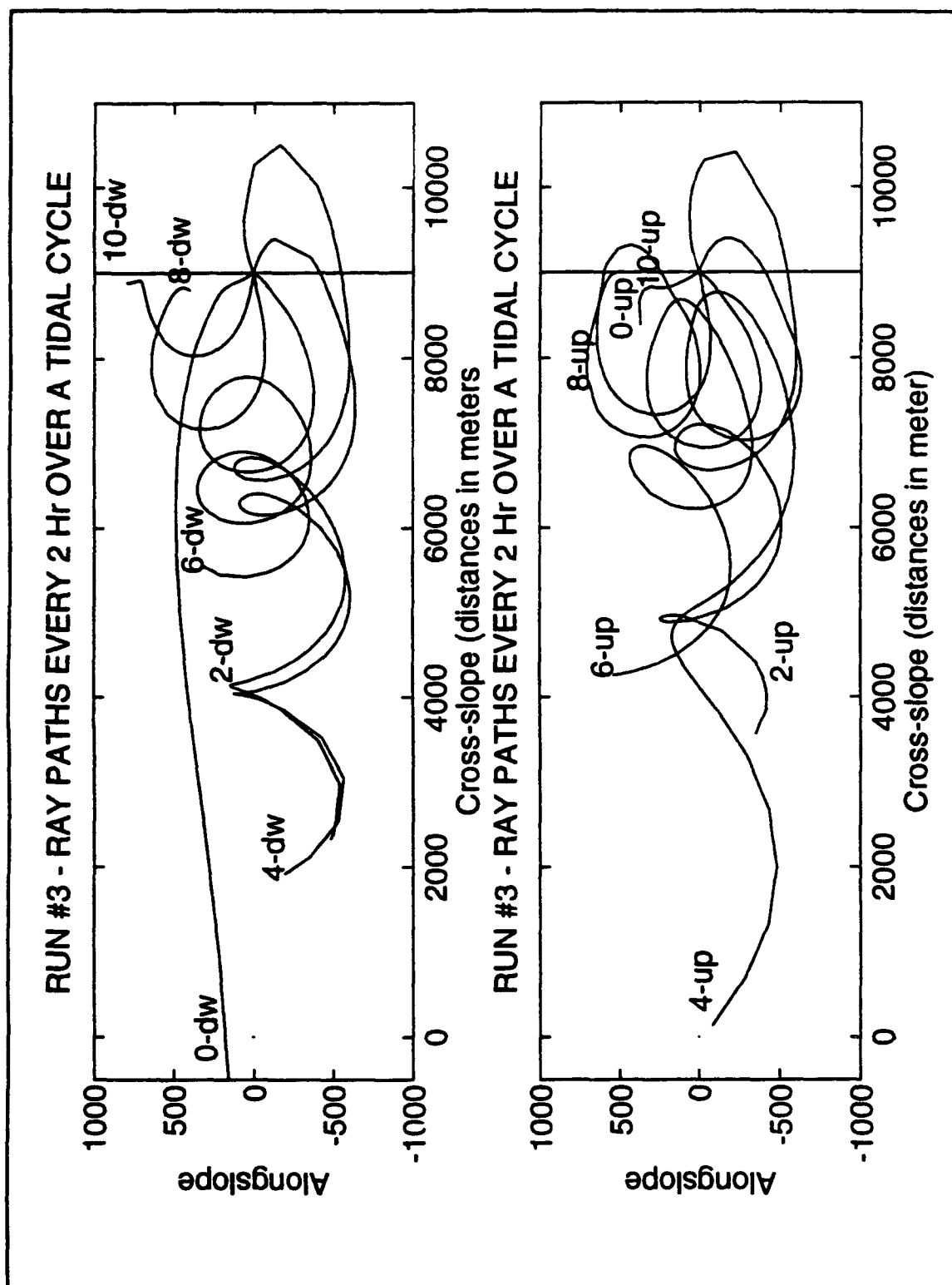
Figure IV-C.3 (a)

176

Figure IV-C.3 (b)

177
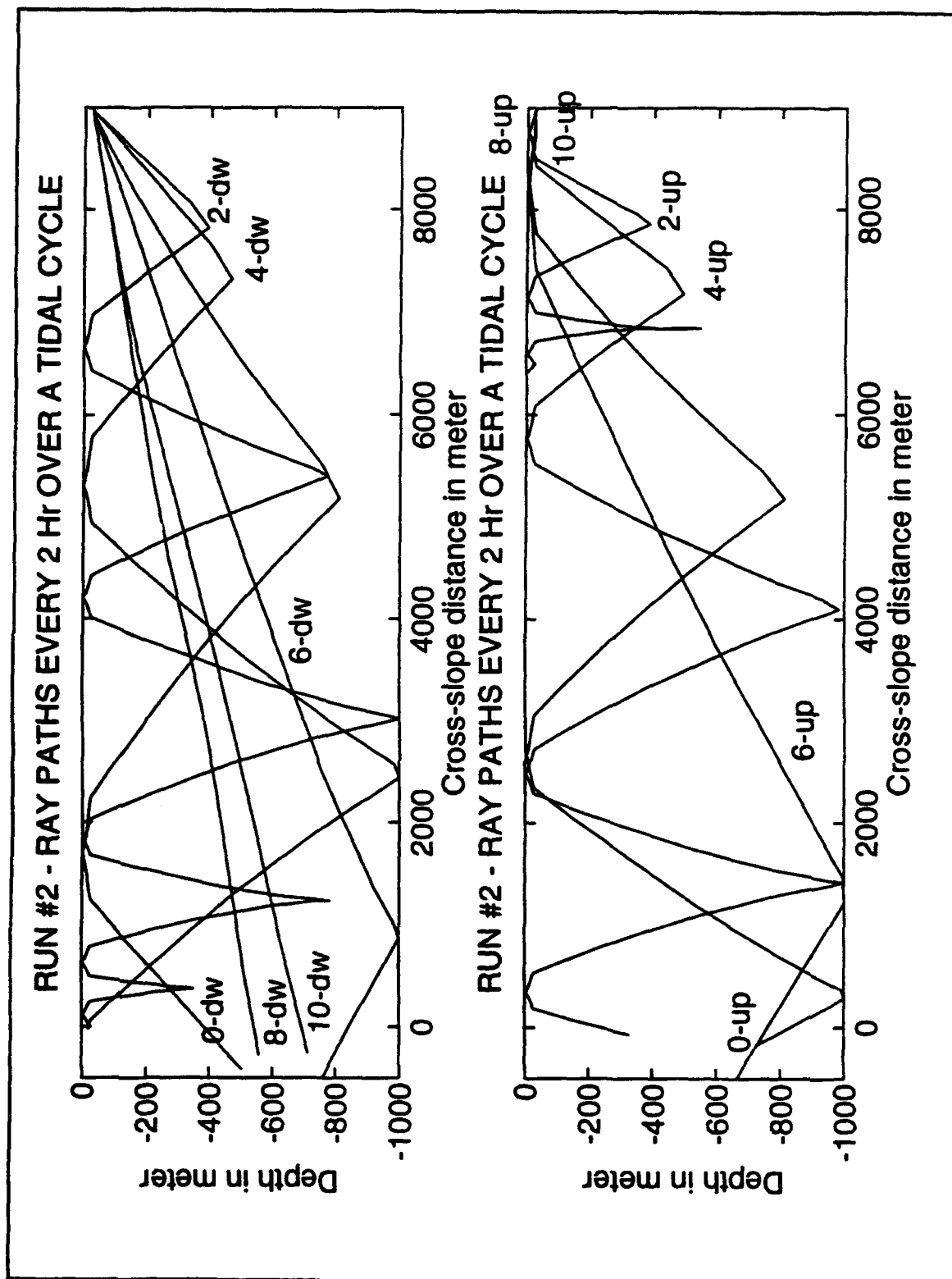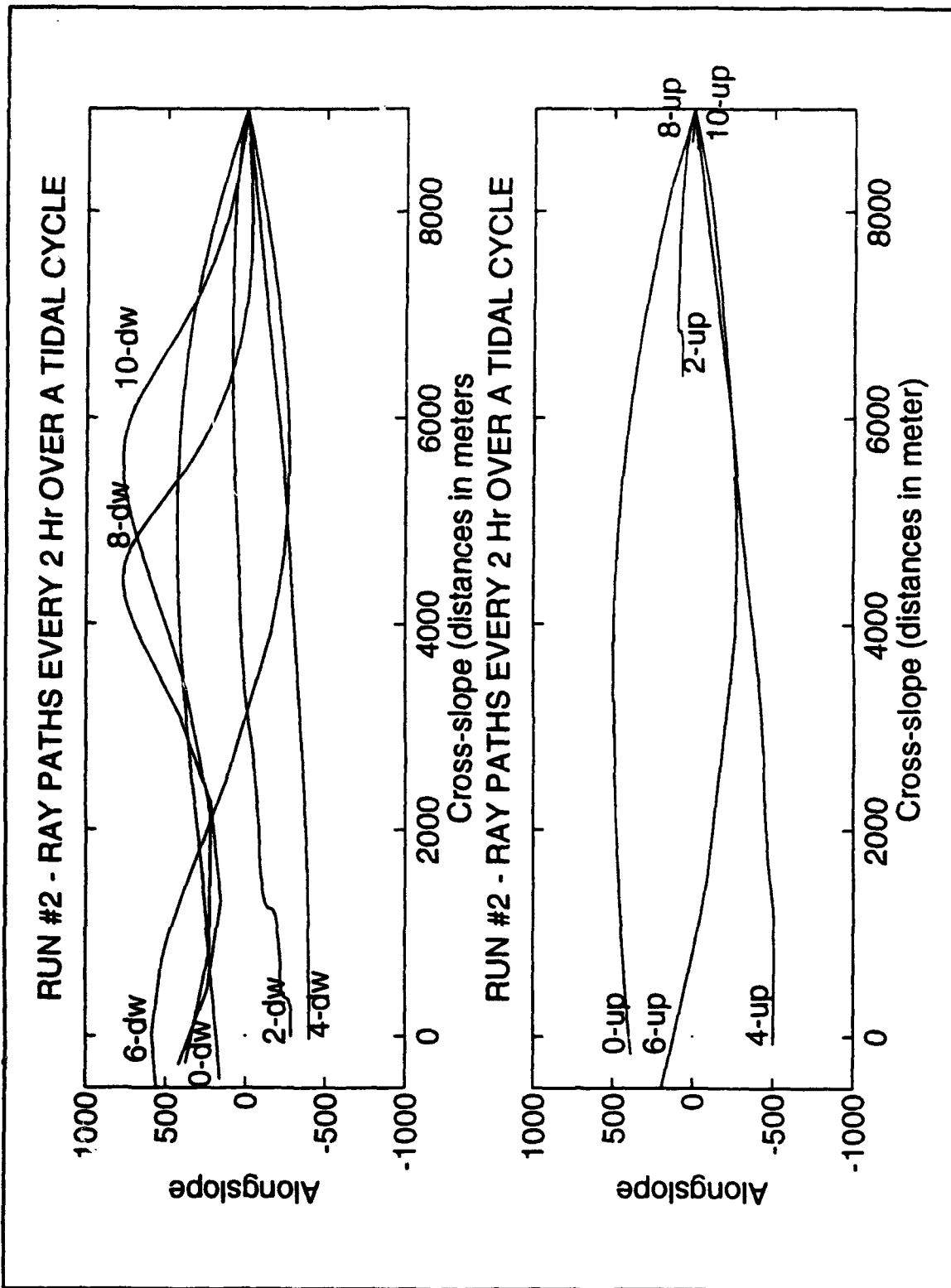
Figure IV-C.4

Ray initial velocity amplitudes for run #2 along the cross-shore axis. The shelf break is at 9 Km and the rays are propagating towards decreasing values. The x-axis identifies each ray path by the correspondent starting time. The letters 'dw' and 'up' identify initially upward and downward rays. The amplitudes were computed from the wave action and intrinsic frequency along the rays for an initial wave velocity amplitude of 0.15 m/s. See text for interpretation of these results.

RUN # 2 - RAY Initial Velocity Amplitude in m/s

Figure IV-C.4

179

Figure IV-C.5

Ray paths for run #3 along the grid representing a continental slope similar to MBAY conditions, extending for 5 Km between 9 Km and 4 Km distances and with depth ranging from 200 to 1000m. Figure (a) shows vertical sections of the rays and Figure (b) the top view (horizontal paths). This run was forced with waves having semidiurnal tidal frequency and a length scale of 7Km, as derived in IV-A. See text for interpretation of these results.

Figure IV-C.5 (a)

Figure IV-C.5 (b)

182

Figure IV-C.6

Time series of frequency at the source for run #3. Figure (i) corresponds to the Eulerian frequency and Figure (ii) to the intrinsic frequency. The horizontal axis represents the time during a typical tidal cycle. The effects of doppler shifting are evident in the Eulerian frequency producing a modulation with the tidal period; however, the straining effects are visible in the intrinsic frequency in the form of a modulation by a frequency twice the tidal, canceling the symmetry of the Eulerian frequency modulation.

Figure IV-C.6

184
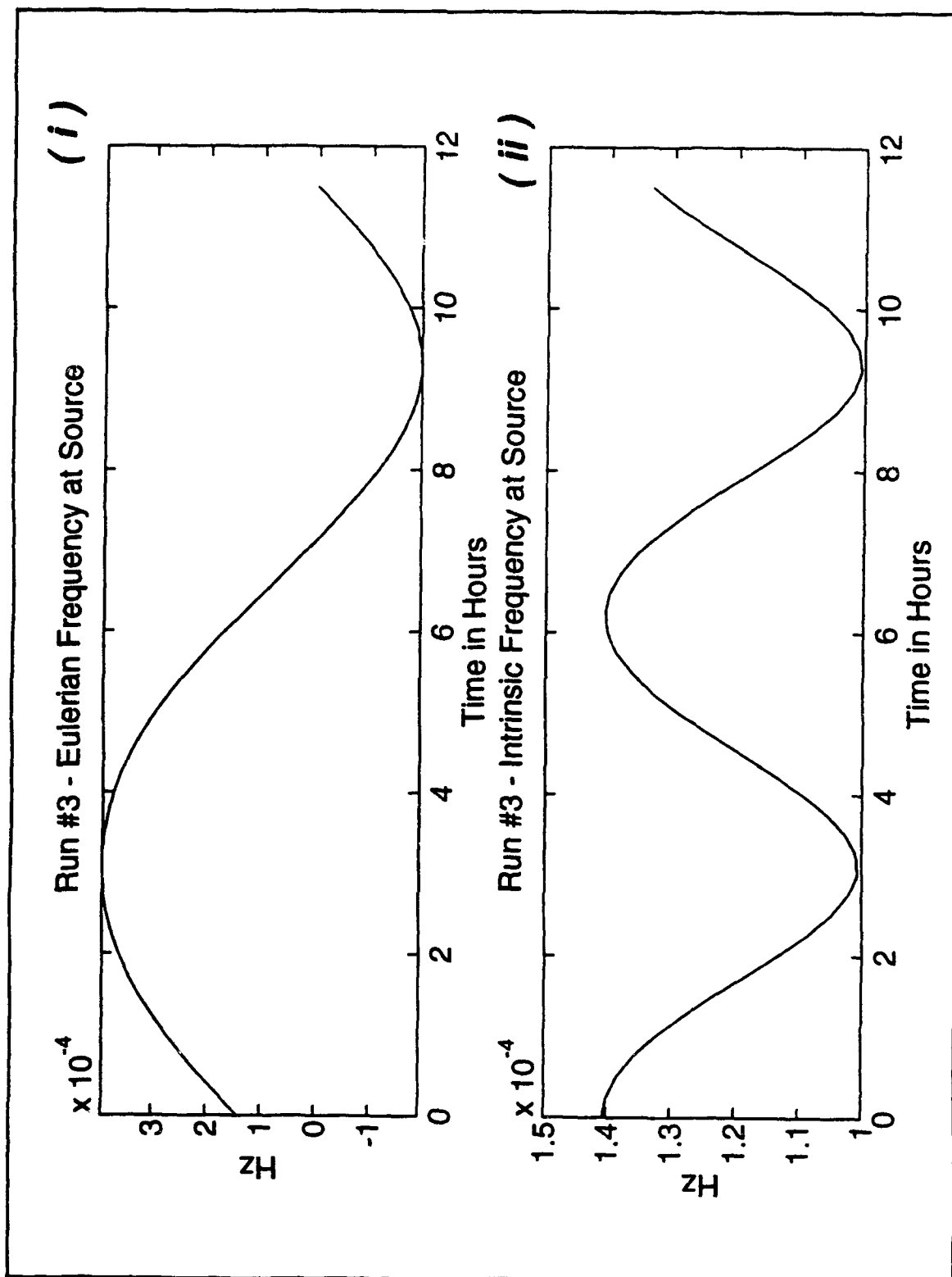
Figure IV-C.7

Evolution of frequency along each ray path for run #3. Figure (a) corresponds to the intrinsic frequency and Figure (b) to the Eulerian frequency. The horizontal axis represents the propagation time for each ray since it started from the source point at the shelf break. Rays are marked in accordance to the time on the tidal cycle at their beginning. One should note the range of the intrinsic frequency extends from approximately the inertial frequency ($0.8 \times 10^{-4} \text{s}^{-1}$) to 3 times the inertial frequency. The Eulerian frequency shows that some rays experience a strong advection, overcoming their group velocities during at least part of the tidal cycle, as can be seen by the negative values.
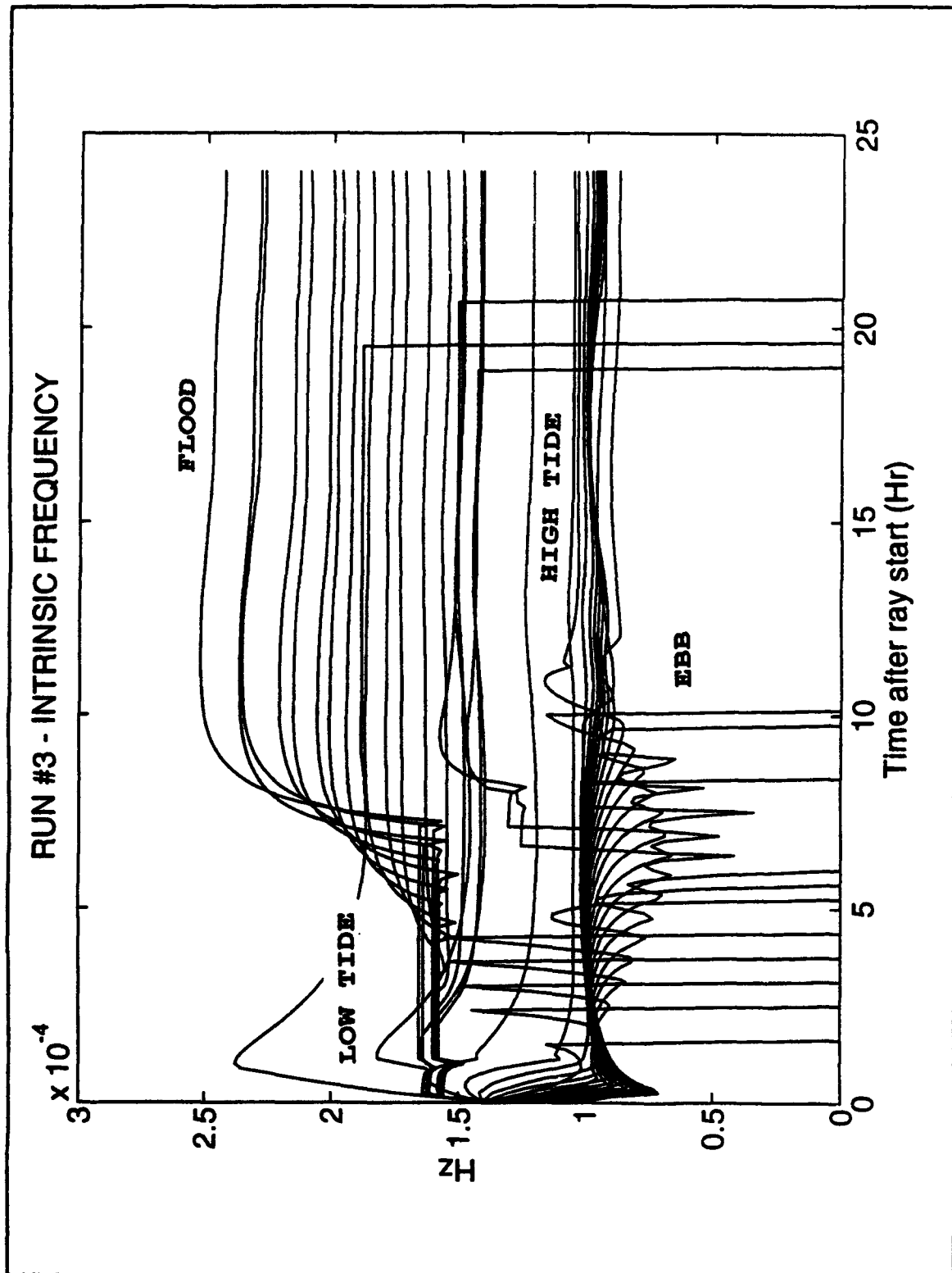
Figure IV-C.7 (a)
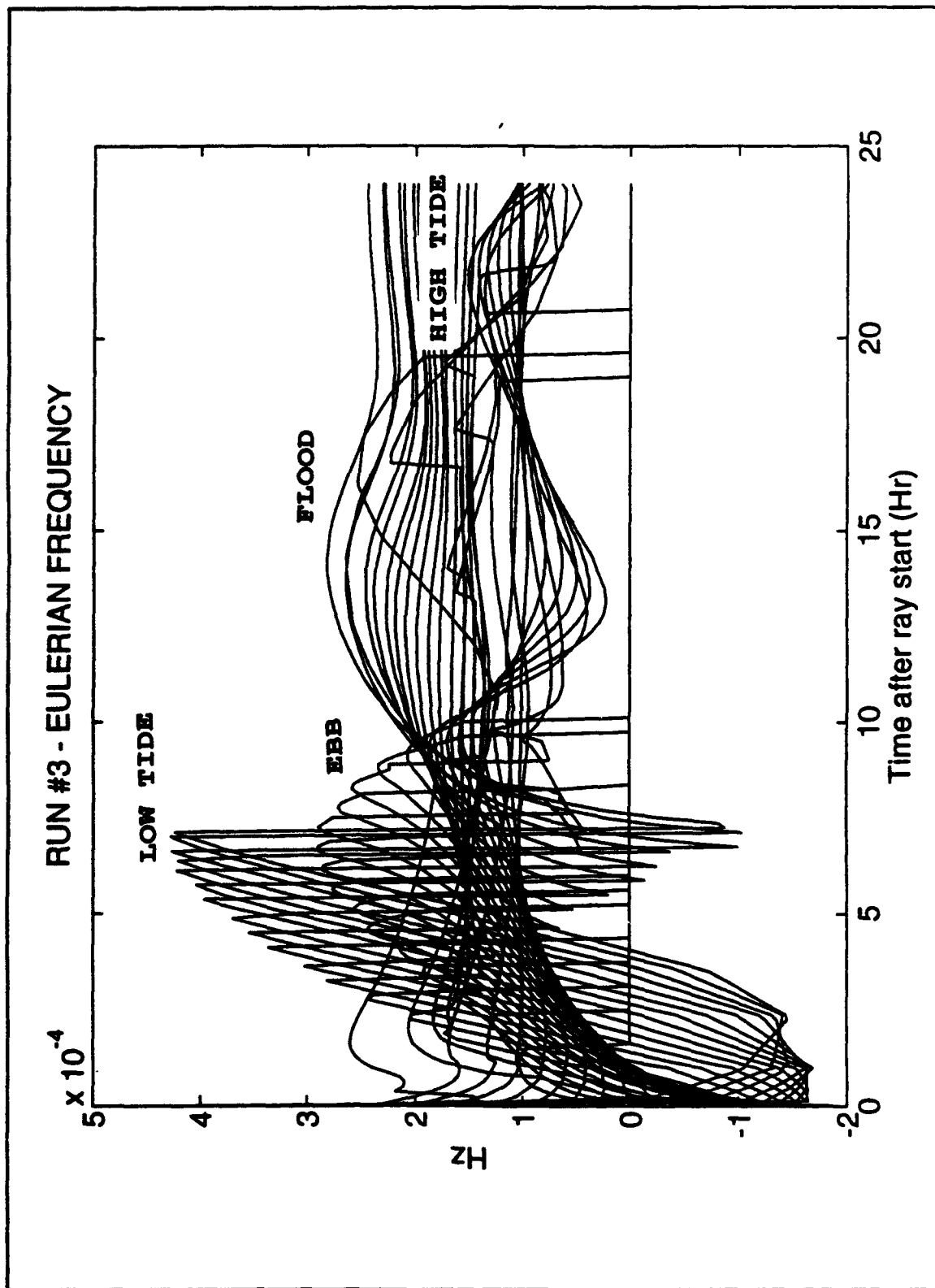
Figure IV-C.7 (b)

Figure IV-C.8

Evolution of wavenumber along each ray path for run #3. Figure
(a) corresponds to the horizontal, cross-slope wavenumber
component and Figure (b) to vertical wavenumber component. The
horizontal axis represents the propagation time for each ray
since it started from the source point at the shelf break.
Rays are marked in accordance to the time on the beginning of
the tidal cycle. One should note the modulation of the
wavenumber by the spatial derivatives of the mean flow. The
rays that start during the flood are advected onto the shelf
where no changes occur; however, when they propagate back to
the shelf break, though the vertical component has significant
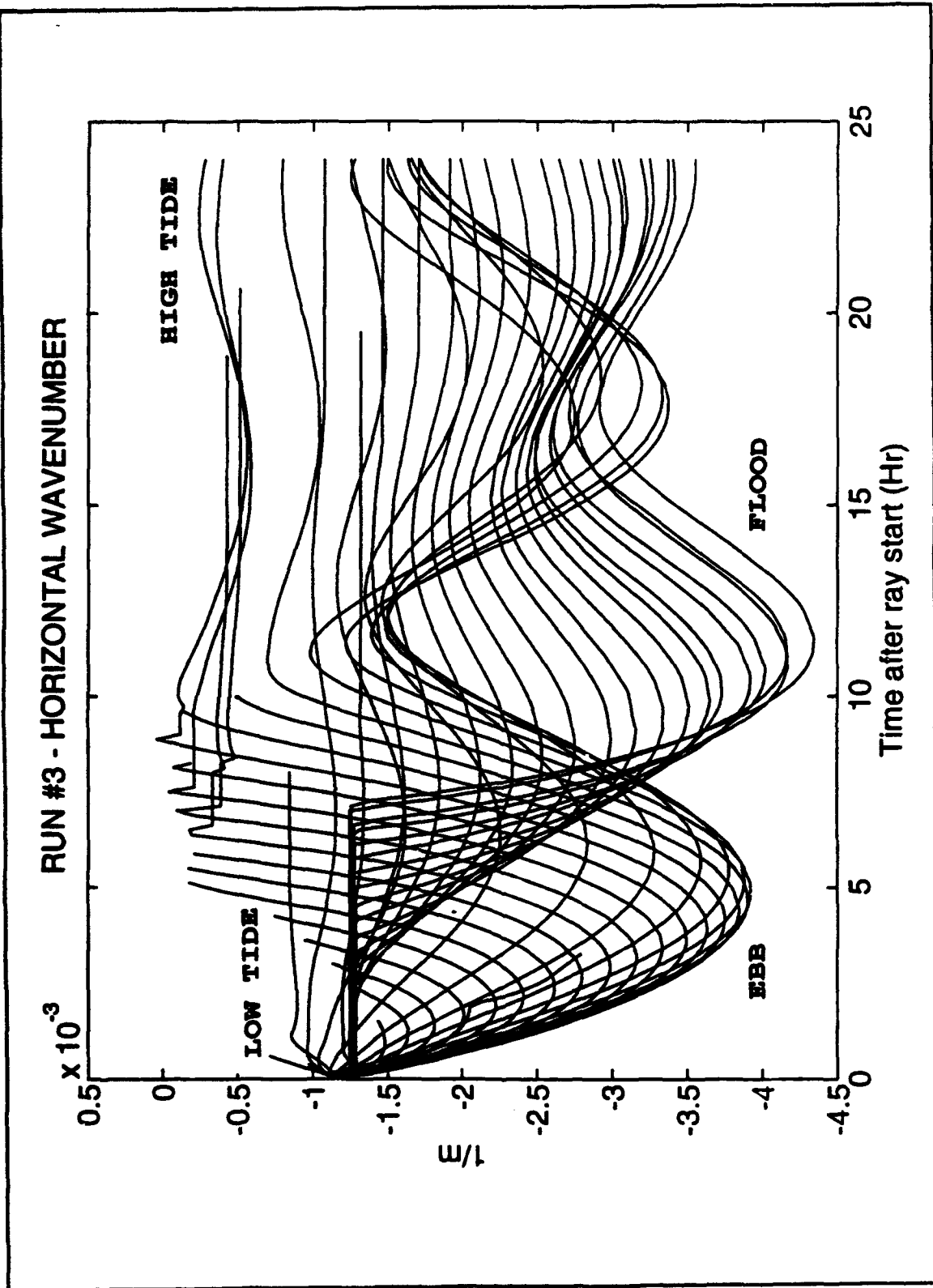variability, the horizontal components do not change like
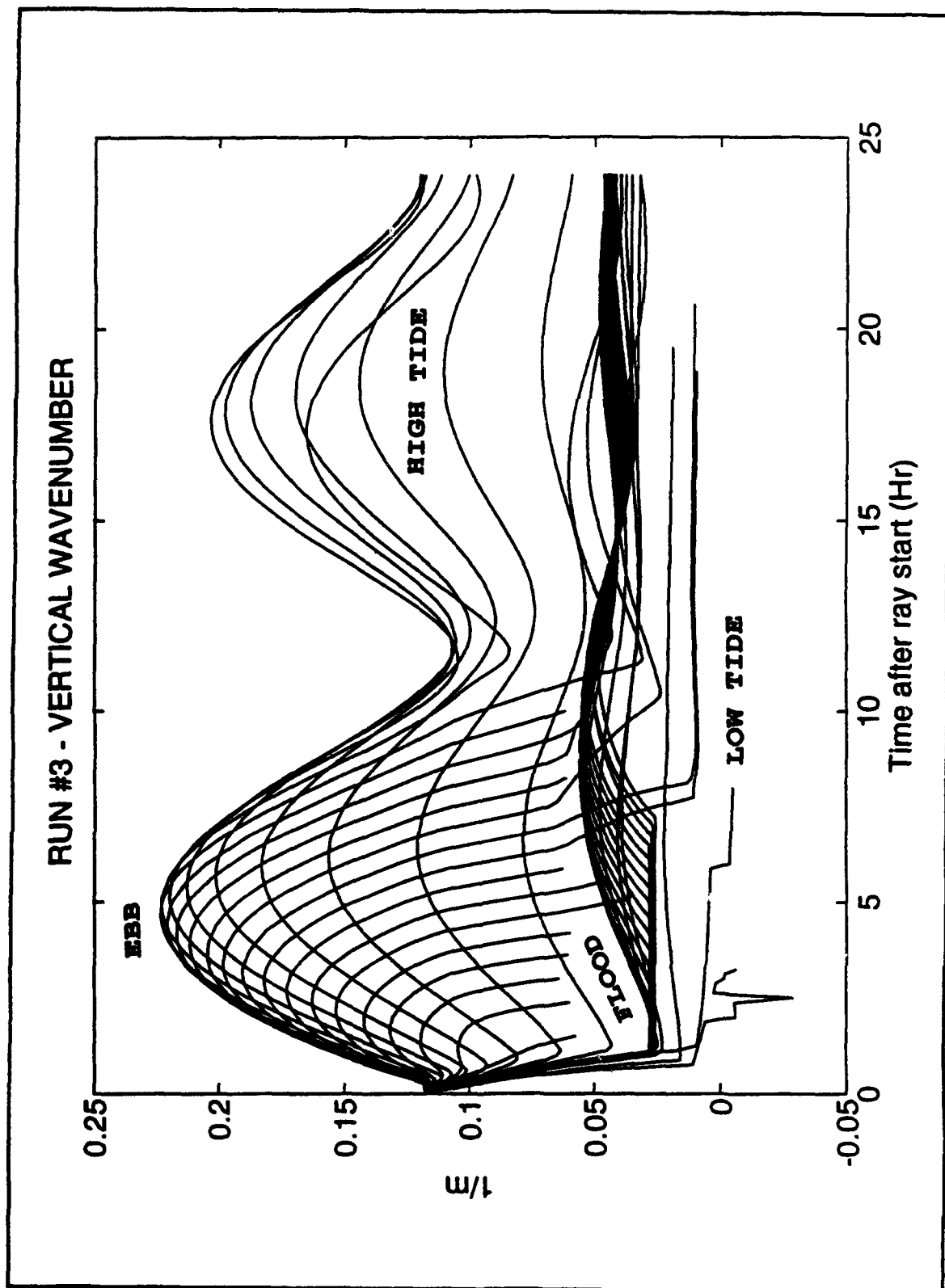those starting at the ebb.

Figure IV-C.8 (a)

189

Figure IV-C.8 (b)

190

Figure IV-C.9

Schematic of ray paths and velocity field estimation. A typical characteristic trajectory (j) starting at time 't0' and 'x=z=0' in the space time domain is displayed. The variables 't_i^j' correspond to the instants the ray arrives to each location in the x-z plane. The time variant velocity function 'V', starting at the origin, is propagated along the ray changing its parameters in accordance with changes in the mean flow and location in space. The instantaneous velocity estimates at time 'T' are then computed by projecting the characteristic path onto the plane x-z that intersects the time axis at the corresponding time. The velocity phase lags are obtained from the time lags '$T-t_i^j$' and the time the ray crossed the origin.
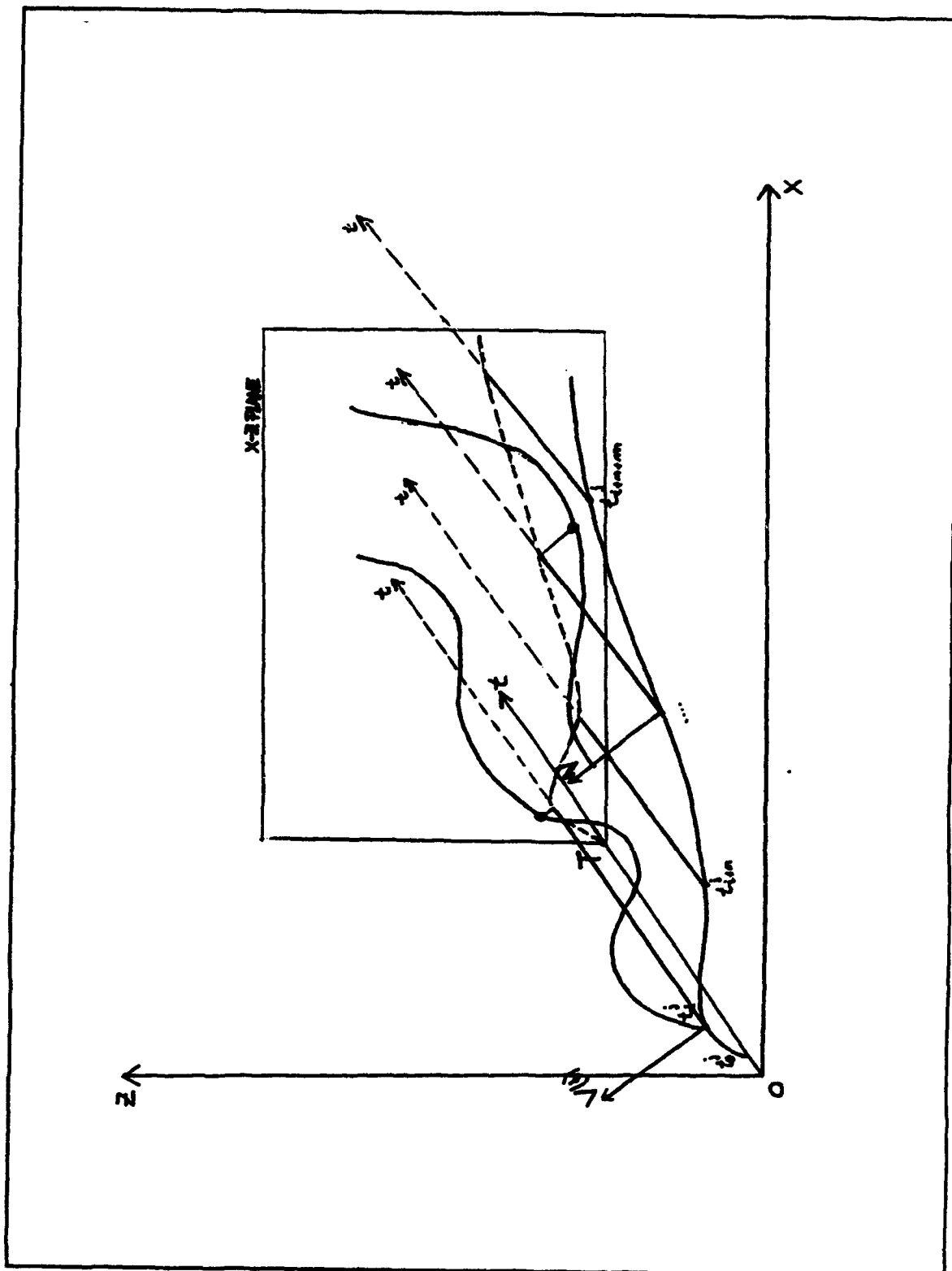
Figure IV-C.9

192

Figure IV-C.10

Position of the interface of a two layer model at the various
phases of the barotropic tide over the edge of a slope. Arrows
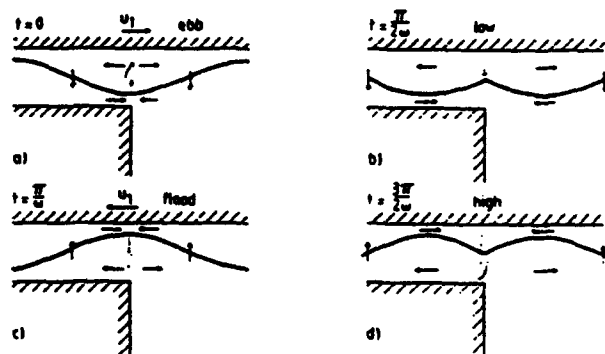denote current direction [from Baines, 1982 fig.6].

Figure IV-C.10

Figure IV-C.11

Contours showing the 24 hour velocity averages resulting from model run #3 over the simplified continental slope. Figure (a) shows the onshore velocity component (U), and Figure (b) shows the alongslope component (V), with the positive direction being into the page. The model was forced with semidiurnal internal waves at a point source at 25m depth in the shelf break. The parameters for this run are summarized in Table IV-C.1. Strong spatially inhomogeneous velocity residuals are observed in depth ranges from 30 to 70m, though smaller residuals can be observed in the profiles at 7500m distance between 150 and 200m depths.
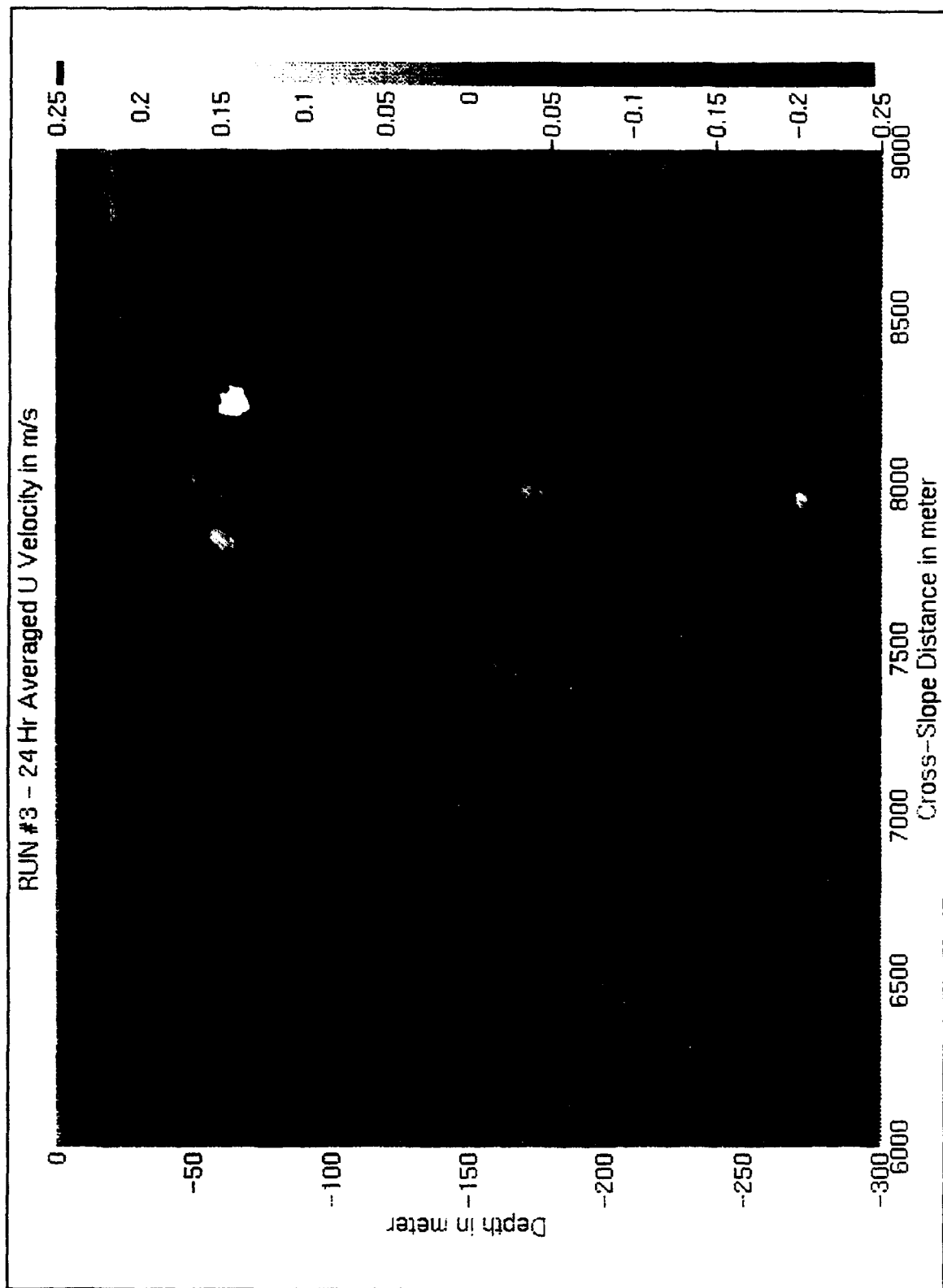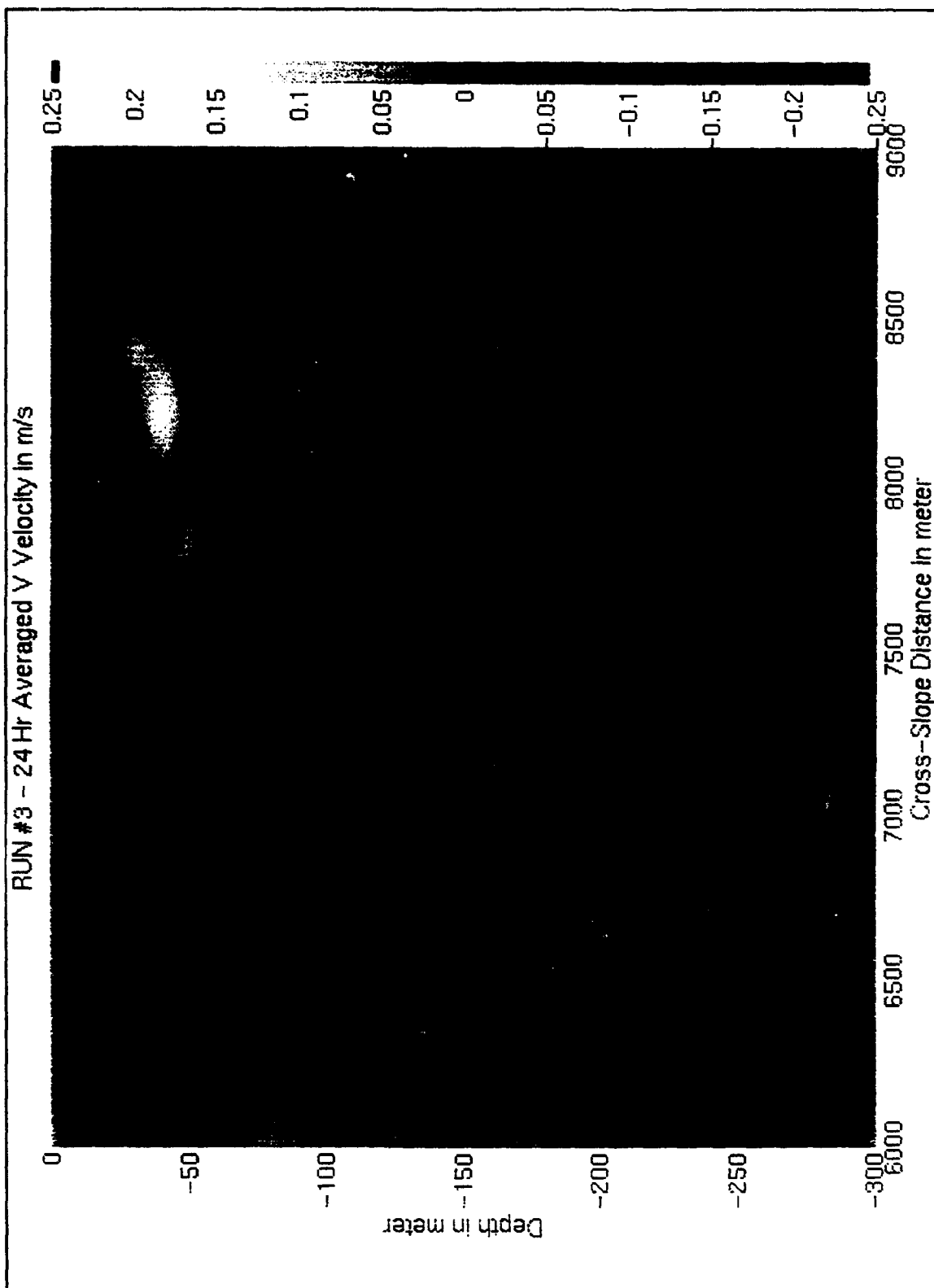
Figure IV-C.11 (a)

Figure IV-C.11 (b)

Figure IV-C.12

Contours showing the velocity profile time series of model run #3 at 6500m (a), 7500m (b), and 8250m (c). The onshore velocity component (U) is displayed in Figures (i) and the alongslope component (V), with the positive direction being into the page is displayed in Figures (ii). The model was forced with semidiurnal internal waves at a point source at 25m depth in the shelf break. The parameters for this run are summarized in Table IV-C.1. Wave-like patterns at several frequencies are seen in all figures, though the profiles at 8750m show higher frequencies compared to the others. One should note the 24 hour periodicity in the V component at 6500m, between 40m and 100m depths, that can also be seen at 50m depth in the profiles at 7500m. The 24 hour averages displayed in Figure IV-C.11 show strong residual currents at these locations and depths.
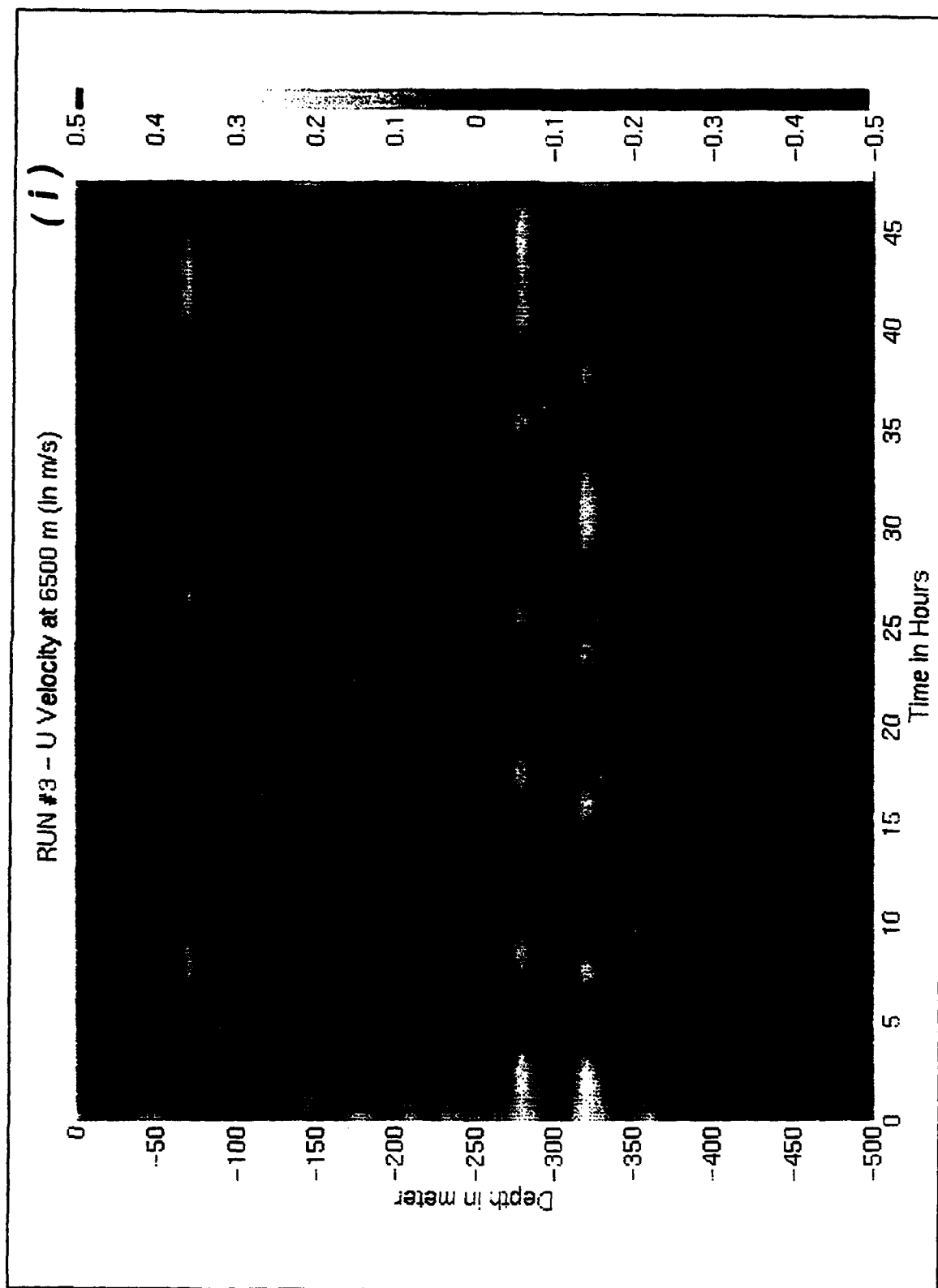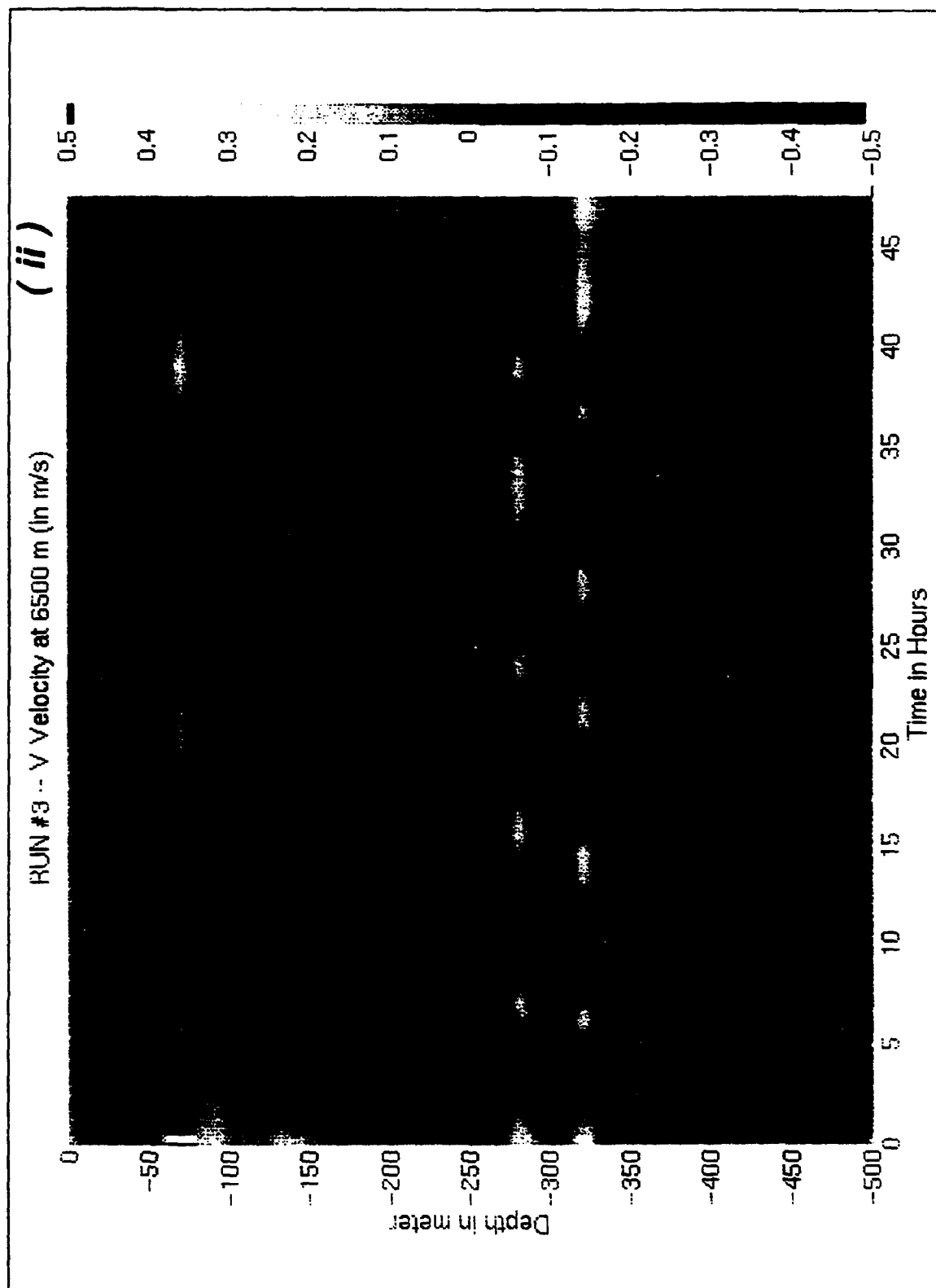
Figure IV-C.12 (a)

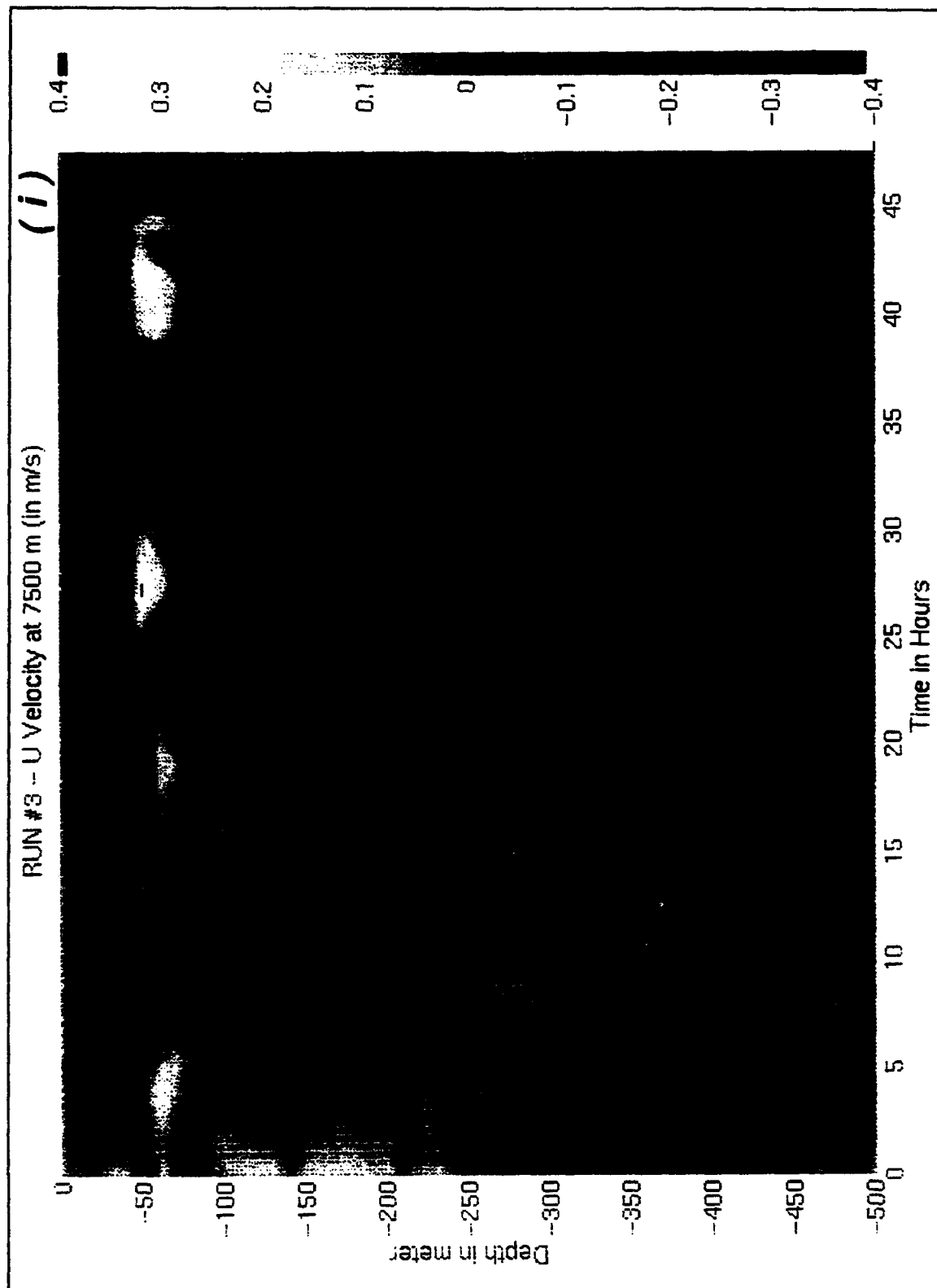199
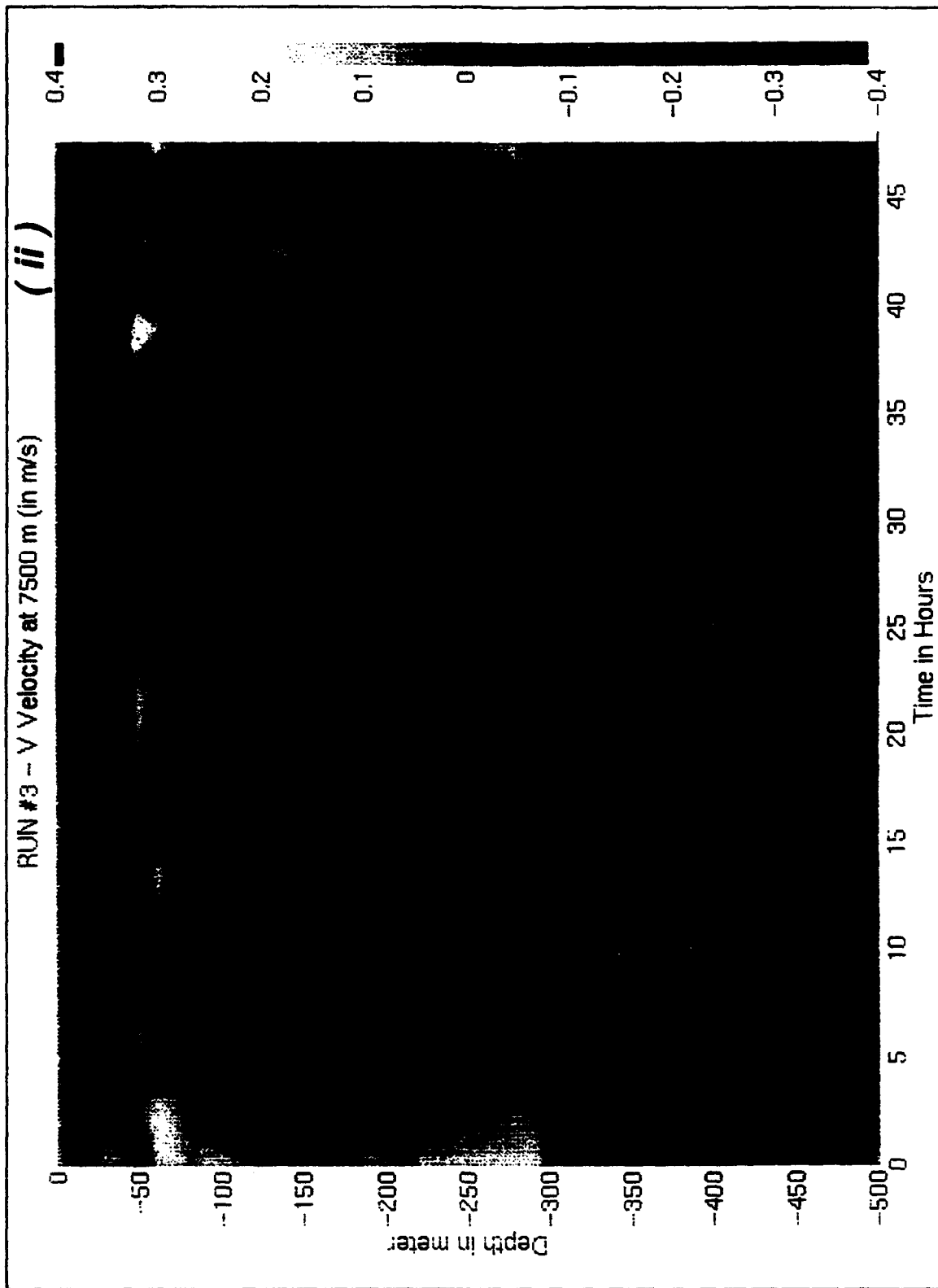
Figure IV-C.12 (a)

Figure IV-C.12 (b)

RUN #3 — V Velocity at 7500 m (in m/s)

(ii)

Figure IV-C.12 (b)

RUN #3 – U Velocity at 8250 m (in m/s)

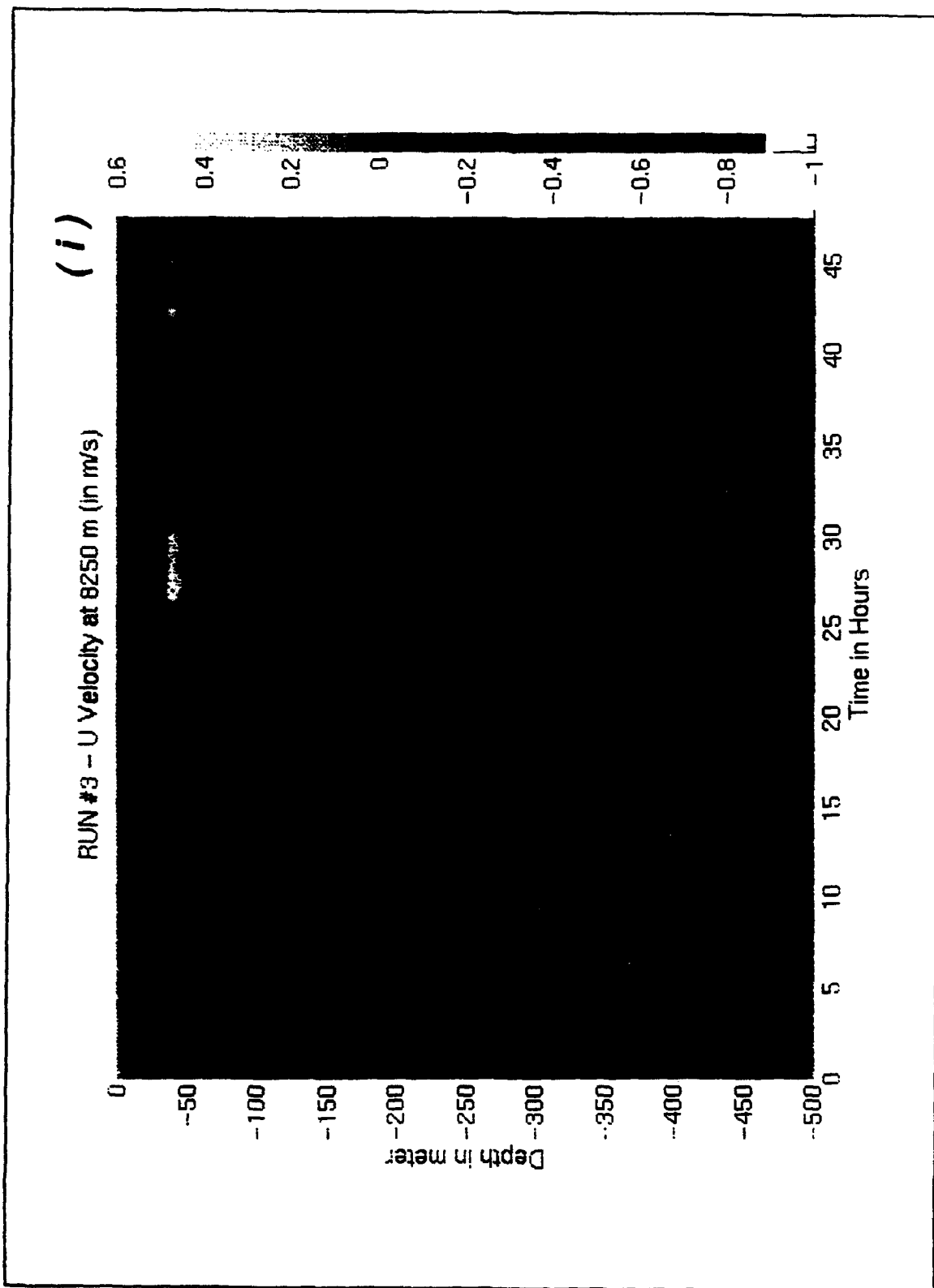**Figure IV-C.12 (c)**

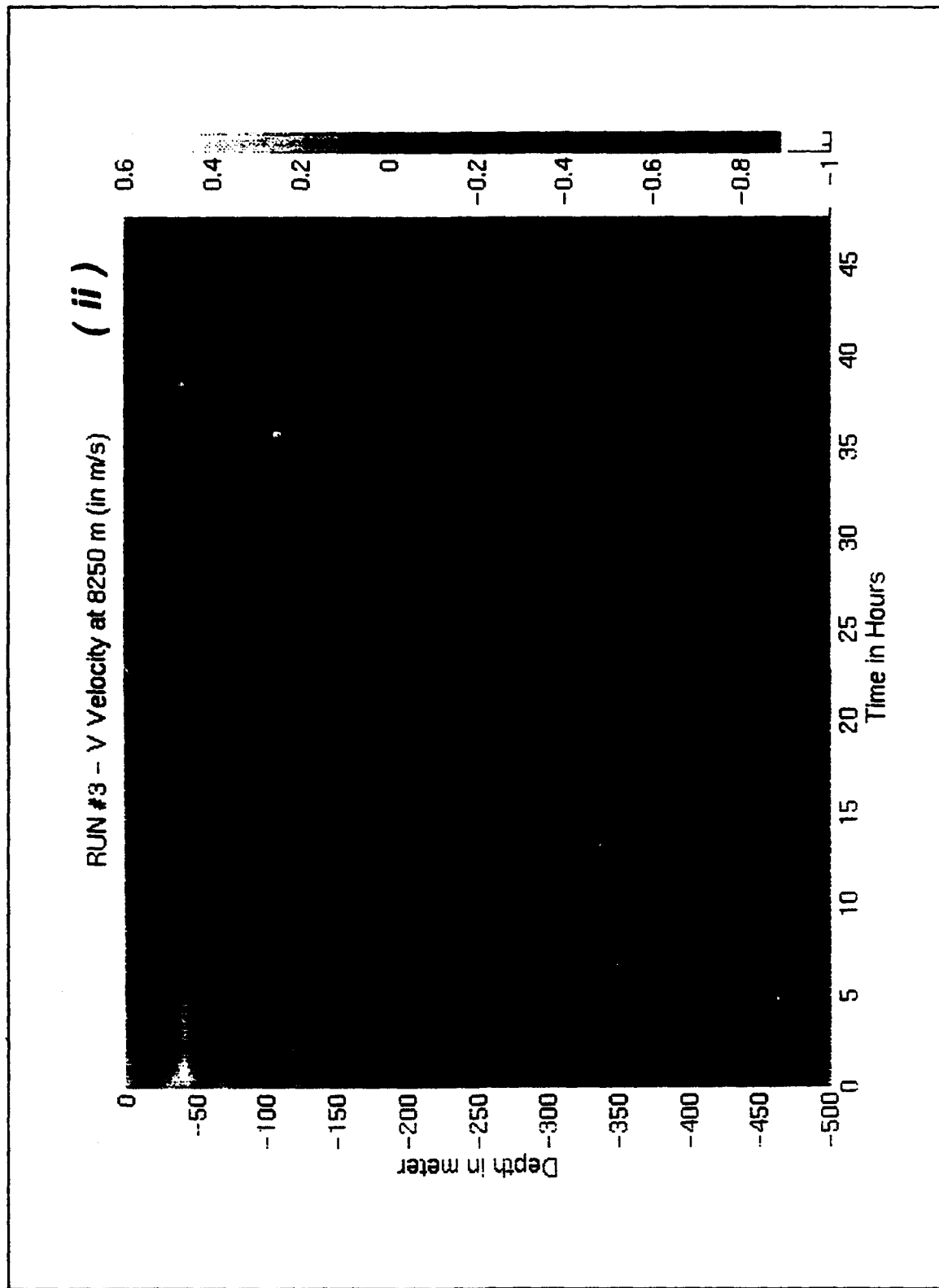RUN #3 – V Velocity at 8250 m (in m/s)

(ii)

Figure IV-C.12 (c)

Figure IV-C.13

Contours showing counts of hourly occurrences of Richardson number below the critical value of 0.25 over a 24 hour period. The assumed stratification is described in Table IV-C.1. The high number of occurrences of below critical conditions at depth ranges of 50 and 100m depth, and within 3000m from the shelf break, suggests that internal tide shear instabilities might exist forcing internal mixed layers as observed during the MBAY experiment. One should note the poor resolution of the estimates due to the broad resolution of the ray tracing numerical method that strongly enhance the edges of the internal wave beam. Nevertheless, the relative potential contribution of the three classes of rays (deeper rays starting during the flood, shallower starting during the ebb, and intermediate starting during slack waters) is evident in the figure, with the shallow rays displaying a larger capacity to generate shear instabilities.
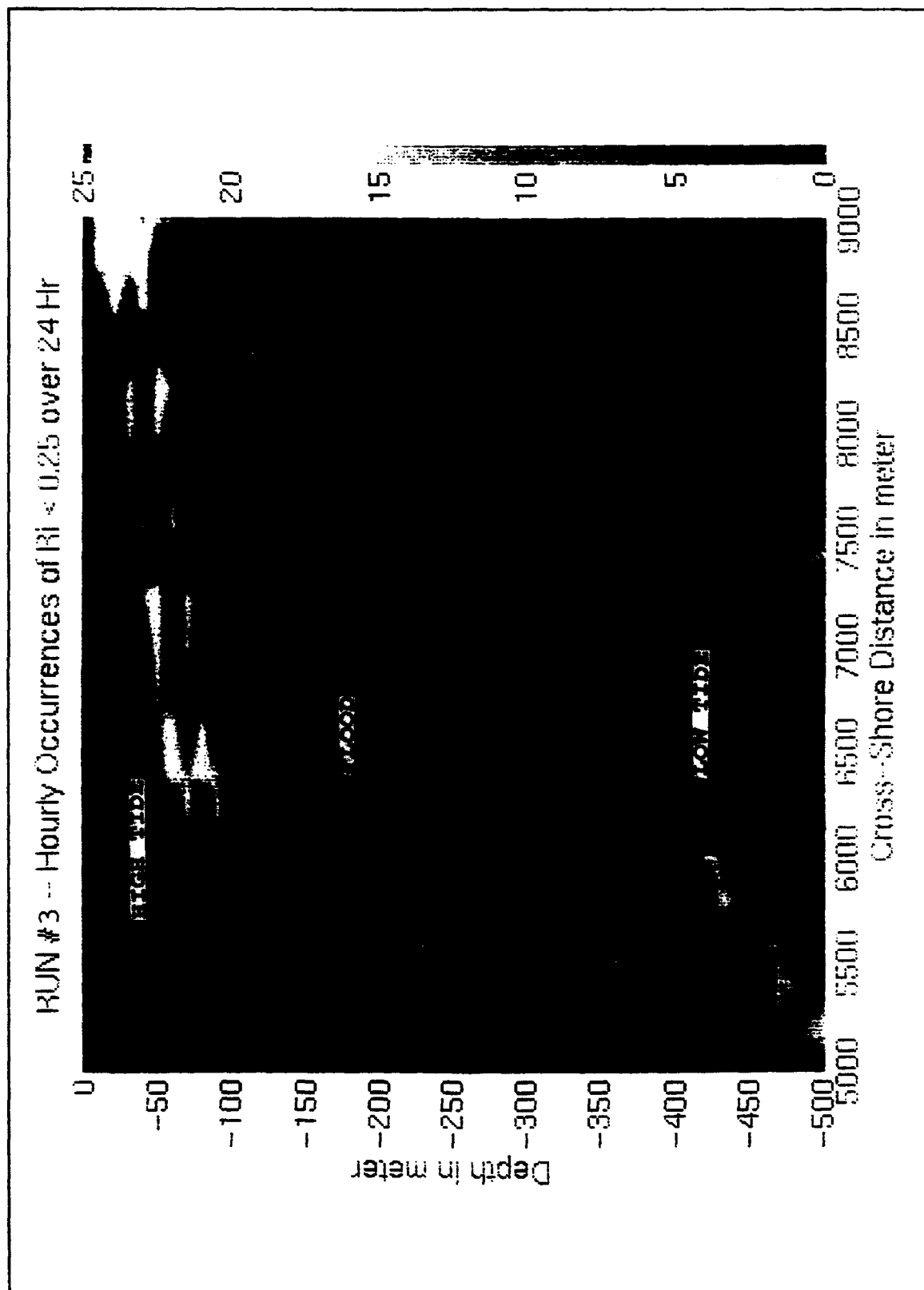
Figure IV-C.13

206

REFERENCES

Abramowitz, A.A., and Stegun, I.A., Handbook of Mathematical Functions, Dover, N.Y., 1968.

Baines, P.G., On Internal Tide Generation Models, Deep-Sea Res., Vol. 29, No. 3A, 307-338, 1982.

Baines, P.G., Tidal Motion in Submarine Canyons-A Laboratory Experiment, J.P.O., Vol.13, 310-328, 1983.

Baines, P.G., and Xin-Hua, F., Internal Tide Generation At Continental Shelf/Slope Junction: A Comparison Between Theory And A Laboratory Experiment, Dyn. Atm. Oc., 9, 297-314, 1985.

Bell, T.H., Topographically Generated Internal Waves in the Open Ocean, J. Geophys. Res., Vol.80, No. 3, 320-327, 1975.

Bender, C.M., and Orzag, S.A., Advanced Mathematical Methods for Scientists and Engineers, McGraw-Hill Int., 1984.

Bretherton, F.P., Propagation in Slowly Varying Waveguides, Proc. Roy. Soc., A.302, 555-576, 1968.

Bretherton, F.P., On the Mean Motion Induced by Internal Gravity Waves, J. Fluid Mech., Vol. 36, part 4, 758-803, 1969.

Bretherton, F.P., and Garrett, C.J.R., Wavetrains in Inhomogeneous Moving Media, Proc. Roy. Soc., A.302, 529-554, 1969.

Breaker, L.C., and Broenkow, W.W., The Circulation of Monterey Bay and Related Processes, Moss Landing Marine Lab., Tech. Pub. 89-1, 1989.

Broenkow, W.W., and McKain, S.J., Tidal Oscillations at the Head of Monterey Submarine Canyon and Their Relation to Oceanographic Sampling and Circulation of Water in Monterey Bay, Moss Landing Marine Lab., Tech. Pub. 72-5, 1972.

Carter, E.F., and Robinson, A.R., Analysis Models for Estimation of Oceanic Fields, J. Atmos. Oceanic Technol., Vol. 4, 49-74, 1987.

Chereskin, T.K., Firing, E., and Gast, J.A., Identifying and Screening Filter Skew and Noise Bias in Acoustic Doppler

<u>Current Profiler Measurements</u>, J. Atmos. Oceanic Technol., Vol. 6, 1040-1054, 1989.

Gan, J., and Ingram, R.G.,<u> Internal Hydraulics, Solitons and Associated Mixing in a Stratified Sound</u>, J. Geophy. Res., Vol. 97, No. C6, 1992.

Garrett, C.J.R., <u>On the Interaction Between Internal Gravity Waves and a Shear Flow</u>, J. Fluid Mech., Vol. 34, part 4, 711-720, 1968.

Garret, C., and Munk, W., <u>Space-Time Scales of Internal Waves: A Progress Report</u>, J.G.R., Vol. 80, No. 3, 291-297, 1975.

Garwood, R.W., <u>An Oceanic Mixed Layer Model Capable of Simulating Cyclic States</u>, J. Phys. Oceanogr., Vol.7, 455-468, May 1977.

Gill, A.E., <u>Atmosphere-Ocean Dynamics</u>, Academic Press, 1982.

Gordon, R.L., <u>Internal Modes in a Submarine Canyon</u>, J. Geophys. Res., Vol. 87, No. C1, 582-584, 1982.

Gregg, M.C., D'Asaro, E.A., Shay, T.J., and Larson, N., <u>Observations of Persistent Mixing and Near-Inertial Internal Waves</u>, J.P.O., Vol. 16, 856-885, 1986.

Habermann, R., <u>Elementary Applied Partial Differential Equations</u>, Prentice-Hall, Inc., 1987.

Holt, S.E., Koseff, J.R., Ferziger, J.H., <u>A Numerical Study of the Evolution and Structure of Homogeneous Stably Stratified Sheared Turbulence</u>, J. Fluid Mech., Vol. 237, 499-539, 1992.

Hughes, R.L., and Ofosu, K.N., <u>On the Behavior of Boundary Undercurrents Near Canyons</u>, J. Geophys. Res., Vol. 95, No. C11, 20259-20266, 1990.

Huthnance, J.M., <u>Internal Tide and Waves Near the Continental Shelf Edge</u>, Geophys. Astrophys. Fluid Dyn., Vol. 48, 81-106, 1989.

Jenkins, G.M., and Watts, D.G., <u>Spectral Analysis and Its Applications</u>, Holden-Day Inc., 1968.

Kay, S.M., <u>Modern Spectral Estimation</u>, Prentice Hall, 1988.

Klinck, J.M., <u>The Influence of a Narrow Transverse Canyon on Initially Geostrophic Flow</u>, J.Geophys. Res., Vol. 93, No. C1, 509-515, 1988.

Klinck, J.M., _Geostrophic Adjustment Over Submarine Canyons_, J.Geophys. Res., Vol. 94, No. C5, 6133-6144, 1989.

Kubota, T., Ko, D.R.S., and Dobbs, L.D., _Weakly-Nonlinear, Long Internal Gravity Waves in Stratified Fluids of Finite Depth_, J. Hydronautics, Vol.12, No.4, 157-165, 1978.

Kunze, E., _Near-Inertial Wave Propagation in Geostrophic Shear_, J.P.O., Vol.15, 544-565, 1985.

Kunze, E., Kennelly, M.A., and Sanford, T.B., _The Depth Dependence of Shear Finestructure off Point Arena and Near Pioneer Seamount_, J.P.O., Vol. 22, No. 1, 1992.

Lamb, K.G., and Shore, J.A., _The Influence of Horizontal Inhomogeneities on the Propagation of High-Frequency Linear Internal Gravity Waves Across a Baroclinic Flow_, J.P.O., Vol. 22, No. 9, 1992.

LeBlond,P.H., and Misak, L.A., _Waves in the Ocean_, Elsevier Oceanography Series, 1978.

Loder, J.W., _Topographic Rectification of Tidal Currents on the Sides of Georges Bank_, J.P.O., Vol. 10, 1399-1416, 1980.

Long, R.R., _Some Aspects of the Flow of Stratified Fluids_, Tellus V, 42-58, 1953.

Maas, L.R.M., and Zimmerman, J.T.F, _Tide-Topography Interactions in a Stratified Shelf Sea I. Basic Equations for Quasi-Nonlinear Internal Tides_, Geophys. Astrophys. Fluid Dynamics, Vol.45, 1-35, 1989a.

Maas, L.R.M., and Zimmerman, J.T.F, _Tide-Topography Interactions in a Stratified Shelf Sea II. Bottom Trapped Internal Tides and Baroclinic Residual Currents_, Geophys. Astrophys. Fluid Dynamics, Vol.45, 37-69, 1989b.

Marple, S.L., _Digital Spectral Analysis with Applications_, Prentice-Hall. Inc., 1987.

Maze, R., _Generation and Propagation of Non-Linear Internal Waves Induced By the Tide Over a Continental Slope_, Cont. Shelf Res., Vol.7, No. 9, 1079-1104, 1987.

McComas, C.H., _Resonant Interaction of Oceanic Internal Waves_, J. Geophy. Res., Vol.82, No. 9, 1397-1412, 1977.

Muller, P., and Olbers, D.J., _On the Dynamics of Internal Waves in the Deep Ocean_, J.Geophys. Res., Vol. 80, No. 27, 1975.

New, A.L., _Internal Tidal Mixing in the Bay of Biscay_, Deep-Sea Res., Vol.35, 691-709, 1988.

Noble, M., and Butman, B., _The Structure of Subtidal Currents Within and Around Lydonia Canyon: Evidence for Enhanced Cross-Shelf Fluctuations Over the Mouth of the Canyon_, J. Geophys. Res., Vol. 94, No. C6, 8091-8110, 1989.

Peregrine, D.H., _Interaction of Water Waves and Currents_, Adv. Applied Mech., Vol. 16, 1976.

Phillips, O.M., _The Interaction Trapping of Internal Gravity Waves_, J. Fluid Mech., Vol.34, part 2, 407-416, 1968.

Pichon, A., and Maze, R., _Internal Tides Over a Shelf Break: Analytical Model and Observations_, J.P.O., Vol. 20, 657-671, 1990.

Pillsbury, R.D., Pilskaln, C.H., Pittock, G., and Still, R.E., _Deep Water Flow Characteristics of Monterey Bay: A Two Year Current Meter Data Set_, Data Rep. 143, Ref. 92-2, College of Oceanography Oregon State Univ., 1992.

Pond, S. and Pickard, G.L., _Introductory Dynamical Oceanography_, 2nd Edition, Pergamon Press, 1989.

Pratt, L.J., and Armi, L., _Hydraulic Control of Flows with Nonuniform Potential Vorticity_, J.P.O., Vol. 17, 2016-2029, 1987.

Prinsenberg, S.J., and Rattray, M., _Effects of Continental Slope and Variable Brunt-Vaisala Frequency on the Coastal Generation of Internal Tides_, Deep-Sea Res., Vol.22, 251-263, 1975.

Robinson, I.S., _Tidally Induced Residual Flows_, in Physical Ocean. of Coastal and Shelf Seas, B. Johns (editor), 1983 .

Shea, R.E., and Broenkow, W.W., _The Role of Internal Tides in the Nutrient Enrichment of Monterey Bay, California_, Est. Coast. and Shelf Sc., 15, 57-66, 1982.

Shepard, F.P., Marshall, N.F., and McLoughlin, P.A., _"Internal Waves" Advancing Along Submarine Canyons_, Science, Vol. 183, 1974.

Stull, R.B., _Boundary Layer_, Kluwer Academic Publishers, 1988.

Thorpe, S.A., _The Excitation, Dissipation, and Interaction of Internal Waves in the Deep Ocean_, J. Geophy. Res., Vol. 80, No. 3, 328-338, 1975.

Wijesekera, H., Padman, L., Dillon, T., Levine, M., Paulson, C., and Pinkel, R., <u>The Application of Internal-Wave Dissipation Models to a Region of Strong Mixing</u>, J.P.O., Vol. 23, No. 2, 1993.

Willmott, A.J., and Edwards, P.D., <u>A Numerical Model for the Generation of Tidally Forced Nonlinear Waves Over Topography</u>, Cont. Shelf Res., Vol. 7, No. 5, 457-484, 1987.

Whitham, G.B., <u>Linear and Nonlinear Waves</u>, John Wiley & Sons, 1974.

INITIAL DISTRIBUTION LIST

1. Defense Technical Information Center   2
   Cameron Station
   Alexandria,VA 22304-6145

2. Library, Code 52   2
   Naval Postgraduate School
   Monterey, CA 93943-5000

3. C.A. Collins (Code OC/Co)   1
   Department of Oceanography
   Naval Postgraduate School
   Monterey, CA 93943-5000

4. Chairman (Code MR/Hy)   1
   Department of Meteorology
   Naval Postgraduate School
   Monterey, CA 93943-5000

5. E.B. Thornton (Code OC/Tm)   1
   Department of Oceanography
   Naval Postgraduate School
   Monterey, CA 93943-5000

6. R.W. Garwood (Code Oc/Gd)   1
   Department of Oceanography
   Naval Postgraduate School
   Monterey, CA 93943-5000

7. T.P.Stanton (Code OC/St)   4
   Department of Oceanography
   Naval Postgraduate School
   Monterey, CA 93943-5000

8. J.H.Miller (Code Ec/Mr)   1
   Department of Electrical
   and Computer Engineering
   Naval Postgraduate School
   Monterey, CA 93943-5000

9. Emanuel Ferreira Coelho   1
   Instituto Hidrografico
   Rua das Trinas 49
   1296 Lisboa Codex
   Portugal

10. Office of Naval Research (Code 420)   1
    Naval Ocean Research and Development
    Activity
    800 N. Quincy Street
    Arlington, VA 22217

11. Director Tecnico   1
    Instituto Hidrografico
    Rua das Trinas 49
    1296 Lisboa CODEX
    Portugal

12. Fundacao Calouste Gulbenkian   1
    Servico de Bolsas de Estudo
    1093 Lisboa CODEX
    Portugal